School of Industrial and Information Engineering
Master of Science in Automation and Control Engineering

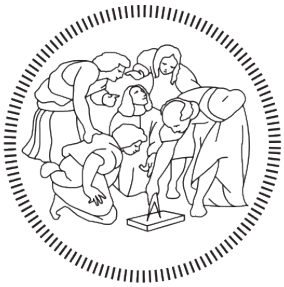

POLITECNICO
MILANO 1863

SIZING, OPTIMISATION AND THERMAL EVALUATION OF AN AXIAL FLUX PERMANENT MAGNET MOTOR IN COMPARISON WITH A RADIAL FLUX MOTOR

Advisor:
Prof. Francesco Castelli Dezza

MSc Thesis of:
Francesca Nava
Matr. 988018

Academic year 2022/23

This study was carried out within the MOST - Sustainable Mobility Center and received funding from the European Union NextGenerationEU (PIANO NAZIONALE DI RIPRESA E RESILIENZA (PNRR) - MISSIONE 4, COMPONENTE 2, INVESTIMENTO 1.4 - D.D. 1033 17/06/2022, CN00000023). This manuscript reflects only the authors' views and opinions, neither the European Union nor the European Commission can be considered responsible for them.

Contents

Abstract iii

Abstract in lingua italiana v

Introduction 1

1 Progress in Axial and Radial Flux Machine Technologies 5
1.1 A Journey Through History . . . 5
1.2 Axial vs Radial Flux Machines . . . 6
1.3 Exploring Axial Flux Machine Advancement . . . 9
1.3.1 Solutions Without Permanent Magnets . . . 9
1.3.2 Solutions With Permanent Magnets . . . 12
1.3.3 Hybrid Radial and Axial Flux Permanent Magnet Machine . . . 16
1.4 Cooling Systems for Electric Motors . . . 17
1.4.1 Housing Cooling . . . 18
1.4.2 Stator Core Cooling . . . 18
1.4.3 Winding Cooling . . . 20
1.4.4 Enhanced Rotor Cooling . . . 24

2 Axial Flux Electrical Machines 27
2.1 Winding Configuration . . . 29
2.2 Equations and Parameters of a Coreless Stator AFPM Machine . . . 31
2.2.1 Motor Model . . . 32
2.2.2 Losses . . . 35
2.2.3 Synchronous reactances computations and supplying conditions . . . 37
2.2.4 Rotor moment of inertia . . . 37
2.2.5 Mechanical and electromagnetic time constants . . . 38
2.2.6 Axial attractive force between backing steel discs of the twin rotor . . . 39
2.3 Commercial Examples of AFPM Machines . . . 39
2.3.1 YASA 750R . . . 39
2.3.2 Koenigsegg Quark e-Motor^{TM} . . . 40

3 Radial Flux PMSM and Control of PM Synchronous Machines 43
3.1 Comparative Analysis of Radial Flux Motors: . . . 43
3.2 Permanent Magnet Synchronous Machines (PMSM) . . . 44
3.2.1 The Historical Evolution . . . 45

3.2.2 Characteristics of the Machine . . . 45
3.2.3 Control and Operative Regions . . . 48
3.3 The case of Nissan LEAF's Motor . . . 52

4 Thermal Sizing Methods **55**
4.1 General rules . . . 55
4.1.1 Heat Exchange . . . 55
4.1.1.1 Conduction . . . 55
4.1.1.2 Radiation . . . 56
4.1.1.3 Convection . . . 57
4.1.2 Conservation of Energy . . . 57
4.1.3 Lumped Parameter Thermal Model . . . 58
4.2 Axial Flux Motor . . . 59
4.2.1 Cooling Methods . . . 59
4.2.1.1 Self-Ventilation Machines . . . 59
4.2.1.2 Externally-Ventilated Machines . . . 60
4.2.1.2.1 External Fans: . . . 60
4.2.1.2.2 Heat Pipes: . . . 60
4.2.1.2.3 Direct Water Cooling: . . . 62
4.2.2 Lumped Parameter Model: Thermal Equivalent Circuit . . . 62
4.3 Radial Flux Motor . . . 65

5 Motor Parameters Design **73**
5.1 General Rules . . . 73
5.2 Axial Flux Machine Model . . . 76
5.2.1 The Developed Design . . . 77
5.3 Radial Flux Machine Model . . . 80
5.3.1 The Developed Design . . . 82
5.4 Thermal Analysis and Cooling System . . . 86
5.4.1 Thermal Equivalent Model . . . 86
5.4.2 Cooling System Design . . . 89

6 Validation of Sizing Results **93**
6.1 Finite Element Analysis Method . . . 93
6.2 Validation of the Axial Flux Machine Model . . . 94
6.2.1 Ansys Maxwell . . . 95
6.2.2 MotorXP-AFM . . . 99
6.3 Validation of the Radial Flux Machine Model . . . 103
6.4 Validation of the Cooling System Design . . . 107
6.4.1 Axial Flux Machine Case . . . 107
6.4.2 Radial Flux Machine Case . . . 109

7 Conclusions and Future Developments **113**

Abstract

This work is based on an initiative of the National Recovery and Resilience Plan (PNRR). The three-year project, of which this thesis constitutes the first chapter, aims to develop prototypes of engines for automotive applications with the goal of promoting the transition to electric vehicles and improving their efficiency. The project focus was on optimising parameters and thermal evaluation of an axial flux motor with a direct comparison to a radial flux motor.

The first fundamental step for this project involved the development of an innovative electric motor, in which the magnetic field flow was directed parallel to the axis of rotation, resulting in a structure called axial flux motor.

For the efficient realisation of a prototype, an "objective function" minimisation algorithm with constraints was implemented using MATLAB. The parameters were subsequently validated through a series of phases using finite element analysis software.

For the radial flux motor model, the user-friendly software Ansys MotorCAD was used, while for the more complex axial flux model, Ansys Maxwell and MotorXP-AFM were employed. The performance results of both motors were compared to identify their respective advantages and disadvantages.

To complete the project, a comprehensive thermal analysis of the two motors was conducted.
For the radial flux motor, a finned enclosure was designed, as its larger dimensions allow for more efficient thermal dissipation without the need for liquid cooling.
For the axial flux motor, given its compactness and high performance, a liquid cooling solution was proposed due to the potential generation of elevated temperatures over the long term.
In both cases the results were validated: using Ansys MotorCAD for the radial flux motor and Ansys Fluent for the axial flux motor.

This research contributes to knowledge in the field of electric motor design for vehicles by providing a detailed and comparative analysis between radial and axial flux motors, with a focus on size, thermal efficiency, and performance. The added value of this work lies in the design and validation of innovative motors, as well as the optimisation of cooling solutions, providing valuable data for the future development of more efficient and sustainable electric vehicles.

Key words:
optimisation, automotive, axial flux permanent magnet machine, radial flux permanent magnet machine, thermal sizing of electrical machines, design of cooling systems for electrical machines.

Abstract in lingua italiana

Questo elaborato è basato su un'iniziativa del Piano Nazionale di Ripresa e Resilienza (PNRR). Il progetto triennale, di cui questa tesi costituisce il primo capitolo, è finalizzato a sviluppare prototipi di motori per applicazioni automobilistiche con l'obiettivo di promuovere la transizione verso i veicoli elettrici e migliorarne l'efficienza. Il focus del progetto è stato l'ottimizzazione dei parametri e la valutazione termica di un motore a flusso assiale con un confronto diretto con un motore a flusso radiale.

Il primo passo fondamentale per questo progetto ha coinvolto lo sviluppo di un motore elettrico innovativo, in cui il flusso del campo magnetico è stato direzionato parallelamente all'asse di rotazione, ottenendo così una struttura chiamata a flusso assiale.

Per la realizzazione efficiente di un prototipo, è stato implementato un algoritmo di minimizzazione delle "objective function" con vincoli, utilizzando MATLAB. I parametri sono stati successivamente validati attraverso una serie di fasi utilizzando software di analisi a elementi finiti.

Per il modello del motore a flusso radiale, è stato utilizzato il software user-friendly Ansys MotorCAD, mentre per il modello a flusso assiale, più complesso, sono stati impiegati Ansys Maxwell e MotorXP-AFM.
I risultati delle prestazioni di entrambi i motori sono stati comparati per identificare i rispettivi vantaggi e svantaggi.

Per completare il progetto, è stata condotta un'analisi termica approfondita dei due motori.
Per il motore a flusso radiale, è stato progettato un involucro alettato, poiché le sue dimensioni maggiori permettono una dissipazione termica più efficiente senza la necessità di raffreddamento a liquido.
Per il motore a flusso assiale, invece, data la sua compattezza e le elevate prestazioni, è stata proposta una soluzione di raffreddamento a liquido a fronte della potenziale generazione di temperature elevate a lungo termine.
In entrambi i casi i risultati sono stati validati: utilizzando Ansys MotorCAD per il motore a flusso radiale e Ansys Fluent per il motore a flusso assiale.

Questa ricerca contribuisce alla conoscenza nel campo della progettazione di motori elettrici per veicoli, offrendo un'analisi dettagliata e comparativa tra i motori a flusso radiale e assiale, con particolare attenzione alla dimensione, all'efficienza termica e alle prestazioni. Il valore aggiunto di questo lavoro risiede nella progettazione e validazione di motori innovativi, nonché nell'ottimizzazione delle soluzioni di raffreddamento, fornendo dati preziosi per il futuro sviluppo di veicoli elettrici più efficienti e sostenibili.

Parole chiave:
ottimizzazione, automotive, macchina a magneti permanenti a flusso assiale, macchina a magneti permanenti a flusso radiale, dimensionamento termico di macchine elettriche, progettazione di sistemi di raffreddamento per macchine elettriche.

Introduction

Moving towards vehicles that produce zero emissions is a crucial objective. In addition, it is imperative to adopt policies that foster innovation and efficiency in vehicles to improve the efficiency of the transportation system and shifting towards low-emission alternative energy sources.

In the year 2021, the average amount of carbon dioxide (CO_2) released by new passenger cars registered in the European Union was 116.3 grams of CO_2 per kilometre. In Italy this value rises to 124.6 grams (Fig.1), indicating a 7.5% increase compared to the figures recorded in 2020.

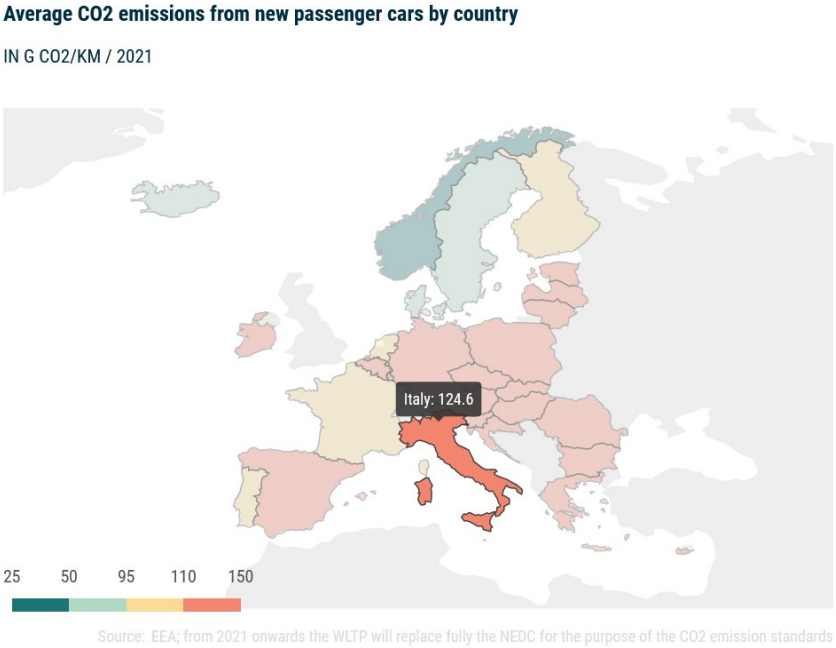

Figure 1: Average CO_2 emissions from new passenger cars, with focus on Italy situation

Transportation has long been recognised as one of the most challenging sectors to decarbonise, within the European Union, domestic transport is responsible for approximately one-quarter of greenhouse gas (GHG) emissions, and unfortunately, emissions in this sector have not shown significant declines. Furthermore, transportation contributes significantly to air pollution, with over half of nitrogen oxides (NO_x) emissions and substantial contributions to other air pollutants like particulate matter (PM). These factors raise concerns for climate, health, and the environment, in addition to issues such as road accidents, congestion, and biodiversity loss.

Italy has implemented measures to enhance its charging infrastructure, aiming to develop 7,500 fast public charging points on public roads by 2025, 13,755 fast charging points in urban areas, and establish 100 experimental charging stations connected to energy storage facilities. Additionally, Italy plans to construct 9 hydrogen facilities for trains and 40 hydrogen refuelling stations for trucks. The country also focuses on completing the TEN-T Core Network Corridors, particularly the Verona-Brenner connection in the Scandinavian-Mediterranean Corridor, while integrating them with the regional rail network and deploying ERTMS (European Rail Traffic Management System) across the national network.

Italy's National Recovery and Resilience Plan (**PNRR**), or "Piano Nazionale di Ripresa e Resilienza" in Italian, is Italy's response to the global COVID-19 emergency and the obstacles that have hindered the economic, social, and environmental growth of our country over the past decades.

The PNRR is a part of the European Next Generation EU recovery project, an unprecedented program in terms of scope and ambition, with a total funding of 750 billion euros allocated for boosting growth, investments, and reforms, of which over half, 390 billion euros, consists of grants.

The plan encompasses six missions:

1. **Digitalisation, Innovation, Competitiveness, Culture:** A total budget of over 49 billion euros (40.3 billion from the Recovery and Resilience Facility and 8.7 billion from the complementary fund) is allocated to promote the digital transformation of the country, support innovation in the production system, and invest in two key sectors for Italy, namely tourism and culture.

2. **Green Revolution and Ecological Transition:** A total of 68.6 billion euros (59.5 billion from the RRF and 9.1 billion from the fund) is dedicated to improving the sustainability and resilience of the economic system and ensuring a fair and inclusive environmental transition.

3. **Infrastructure for Sustainable Mobility:** With a total amount of 31.5 billion euros (25.4 billion from the RRF and 6.1 billion from the fund), its primary goal is the development of a modern, sustainable transportation infrastructure extending to all areas of the country.

4. **Education and Research:** A total of 31.9 billion euros (30.9 billion from the RRF and 1 billion from the fund) is allocated to strengthen the educational system, digital and technical-scientific skills, research, and technology transfer.

5. **Inclusion and Cohesion:** This mission has a total allocation of 22.6 billion euros (19.8 billion from the RRF and 2.8 billion from the fund) to facilitate labour market participation, including through training, strengthen active labour market policies, and promote social inclusion.

6. **Health:** A total of 18.5 billion euros (15.6 billion from the RRF and 2.9 billion from the fund) is dedicated to strengthening prevention and healthcare services at the local level, modernising and digitalising the healthcare system, and ensuring equitable access to healthcare.

Therefore, PNRR plan includes initiatives to promote sustainable local transport, such as extending cycle lanes, expanding metro and tramway networks, and introducing zero-emission buses. The regional public transport bus fleet will be replaced with at least 3,000 zero-emission buses.

Focusing more deeply on electrical vehicles, one of the main troubles is to develop high power and torque electrical motors able to work at high speed to be applied in the automotive industry. Another challenge in this field is the reduction of the use of rare Earth minerals; an innovative method for producing high-performance magnets has the potential to reduce Europe's reliance on rare earth elements as it shifts towards a carbon-neutral economy.

A possible solution to these obstacles could be to remove permanent magnets from electrical motors, discussed in **Chapter 1** with pros and cons and a special focus on axial flux motors that could be a possible solution for high torque density and space-constrained applications a sub-chapter is then dedicated to the state of the art of cooling solutions for this type of motor structure.

In **Chapter 2** the theory regarding accurate motor sizing for axial machines is examined.

To highlight the significance of this novel motor design, **Chapter 3** not only discusses the structure of radial motors but also provides extensive details on the control aspects, which bear a striking resemblance to the control methods adopted in purely axial motors.

Chapter 4 is dedicated to assess the thermal sizing methods theory.

Sizing algorithms, methods, and design outcomes are addressed in **Chapter 5**.

Chapter 6 is focused on the validation and to the results given by the analysis of the models built in chapter 5, with a special highlight on the axial/radial flux models comparison.

To finalise, **Chapter 7** is then devoted to conclusions and possible future development in this field.

Chapter 1

Progress in Axial and Radial Flux Machine Technologies

1.1 A Journey Through History

The history of the design of electrical machines is a captivating journey through time, spanning several centuries and marked by key developments that have fundamentally shaped the modern world. It all began with the early experiments in the 17^{th} and 18^{th} centuries when scientists like William Gilbert and Otto Von Guericke first delved into the mysteries of electricity. These early investigations lead the way for groundbreaking discoveries.

In the late 18th century, Alessandro Volta's invention of the voltaic pile, the precursor to modern batteries, provided a consistent source of electrical energy; his innovation was a critical step in harnessing electricity for practical use.

The 19^{th} century witnessed a wave of activity in the field of electromagnetism. Hans Christian Oersted's remarkable discovery of electromagnetism in 1820 was followed by André-Marie Ampère's formulation of Ampère's law, which deepened the following understanding of electrical phenomena.

In this fertile scientific environment, inventors and engineers began to experiment with electric motors. Michael Faraday's work in 1821 resulted in the creation of the first electromagnetic rotating device, known as the homopolar motor (Figure 1.1). Faraday's pioneering research laid the groundwork for the development of practical electric motors, which eventually emerged in the 1830s thanks to innovators like William Sturgeon and Thomas Davenport.

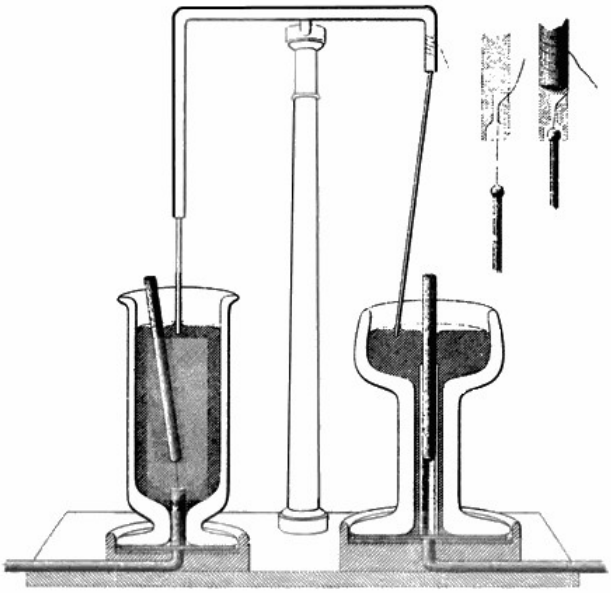

Figure 1.1: Michael Faraday's first homopolar motor.

The mid-to-late 19^{th} century marked the development of dynamos, or generators, which could convert mechanical energy into electrical energy. Michael Faraday and Hippolyte Pixii independently created early versions of these devices. The work of individuals like Ernst Werner von Siemens, Samuel Morse, Charles Francis Brush, and Thomas Edison further refined generator designs and improved their efficiency.

The late 19^{th} and early 20^{th} centuries brought significant advancements in electric motor technology, notably Nikola Tesla's groundbreaking invention of the alternating current (AC) induction motor in the late 1880s. Figures like Charles Steinmetz and Nikola Tesla continued to advance the field of electric motors through theoretical insights and practical applications.

In the 20^{th} century, electrical machines became integral to modern society, powering everything from household appliances to industrial machinery and electric vehicles. Ongoing research and development focused on enhancing efficiency and sustainability, with innovations in materials, power electronics, and the integration of renewable energy sources.

1.2 Axial vs Radial Flux Machines

Axial and radial flux electric machines represent two distinct design approaches in the field of electric motors, each with its own set of advantages and disadvantages, it is interesting to make an overview on both of them and try to visualise the best one in the case of automotive applications.

Axial flux machines have a thinner, pancake-like configuration, where the magnetic flux flows parallel to the rotational axis (shaft). In contrast, radial flux machines have a more traditional design, with the magnetic flux moving radially outward from the centre (Figure 1.2).

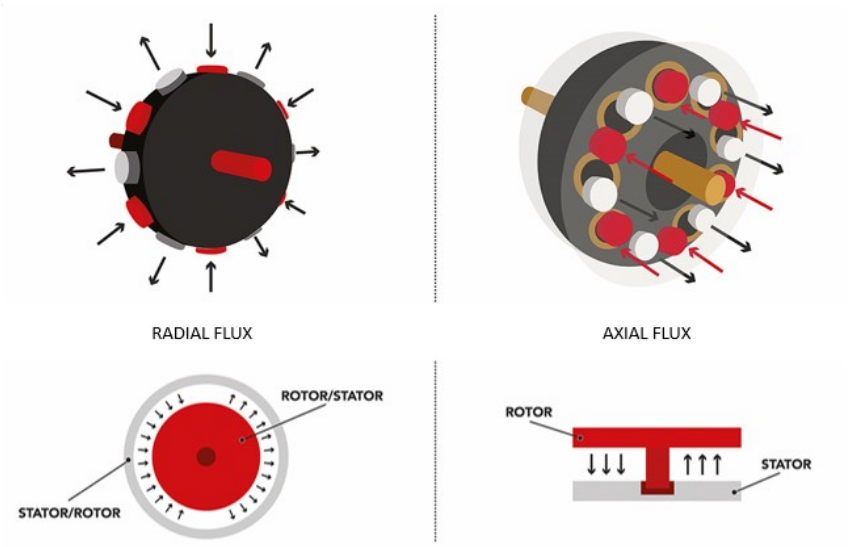

Figure 1.2: Focus on the magnetic flux direction in both Axial and Radial machines.

The primary difference lies in their geometry and magnetic flux path. Axial flux machines offer benefits such as compactness, potentially higher power density, and improved cooling due to their larger surface area. However, they may require more complex cooling systems and face challenges with winding arrangement, these problems will be analysed more in detail in the next dedicated paragraphs. Radial flux machines, on the other hand, have a well-established design with reliable winding layouts, making them easier to manufacture and service. However, they tend to be bulkier and may have limitations in power density.

In radial flux machines, the torque-diameter relationship varies with the square power and linearly with length, while in axial flux machines, this relationship follows a cubic power law. Consequently, electric motors with axial flux have a distinct external appearance with a larger diameter and reduced width, resulting in reduced axial space requirements compared to radial flux machines while maintaining the same torque output. This greater distance between the rotor magnets and the axis increases the maximum attainable torque. However, the higher rotor diameter generates a significant centrifugal force at high rotational speeds, which could potentially dislodge the magnets. Its reduced thickness in relation to the increased diameter makes it particularly suitable for installation at the gearbox output, especially in sports cars and motorcycles. The ability to generate the magnetic field using permanent magnets allows the construction of synchronous machines with a high number of pole pairs, effectively managing production costs and footprint. Consequently, this technology enables the development of lighter vehicles or, for the same weight, more high-performing ones.

Taking the example of an axial flux motor with two rotors and a single stator at its centre (which will be analysed in detail in the upcoming chapters), it's evident that the stator consists of a circular core created by spirally winding a thin strip of ferromagnetic material (Figure 1.3).

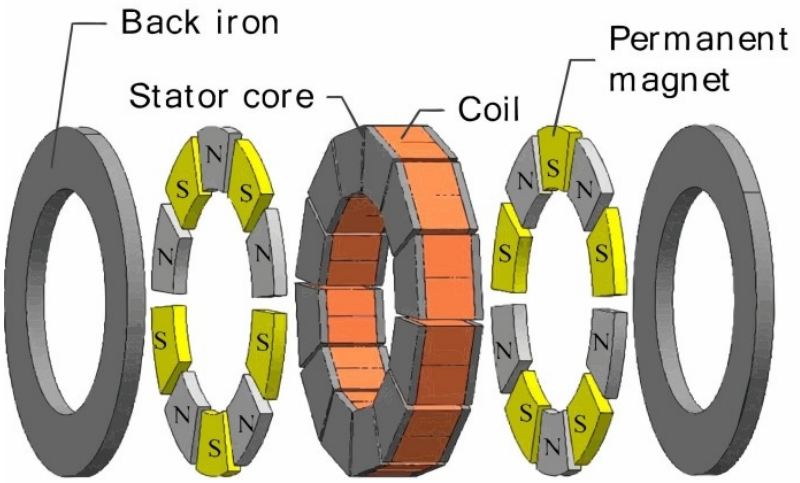

Figure 1.3: Double Rotor Single Stator Axial Flux Machine.

Conductors are wound around this core, and each coil is subjected to two magnetic fluxes generated by the rotors. The rotors, in turn, are positioned on the two outer sides of the stator, with magnets featuring similar magnetic poles facing each other. The flux enters the stator azimuthally and exits axially on the adjacent pole pitch. Furthermore, unlike radial flux machines, where a significant portion of the windings (up to 50%) remains inactive, electric motors with axial flux have 100% of the winding completely active, resulting in significant benefits in terms of electrical resistance (heat dissipation) and power-to-weight ratio.

The cooling system also differs: in radial flux machines, heat must be transported through the stator to the machine's exterior. However, steel is not an excellent conductor, and cooling the coil is challenging because it is not in direct contact with the motor casing. In the case of axial flux machines, the windings are in direct contact with the external aluminium casing, which is an excellent conductor. As a result, cooling is more straightforward and efficient. This technology finds a natural application in the automotive industry, where high torque density is a critical requirement. Multiple-stage structures, consisting of several stators and rotors, can be developed to meet specific performance needs.

The choice between axial and radial flux machines depends on the specific application and trade-offs between size, efficiency and cooling requirements. Axial flux machines are well-suited for applications with space constraints, like electric vehicles, while radial flux machines are often preferred for more traditional industrial and commercial applications where reliability and ease of maintenance are critical.

1.3 Exploring Axial Flux Machine Advancement

In an era marked by an urgent need to combat climate change, the automotive industry is swiftly moving towards a future where zero-emission vehicles play a pivotal role. One of the key solutions driving this transformation is the adoption of high-torque electric motors. These motors are at the forefront of sustainable transportation, offering remarkable performance while minimising environmental impact. In this discussion, we will focus on a critical aspect of these motors: the comparison between axial flux machines with and without permanent magnets, with a specific aim of reducing the use of rare earth materials. This exploration sheds light on the innovative strategies that are shaping the future of automotive engineering and sustainability.

1.3.1 Solutions Without Permanent Magnets

One potential avenue for enhancing the performance of axial flux machines without resorting to the use of permanent magnets involves the incorporation of Grain-Oriented Electrical Steel (GOES). GOES is a specialised variant of electrical steel utilised in the manufacturing of electrical devices like transformers, generators, and other systems demanding exceptional magnetic efficiency.

GOES is manufactured by rolling electrical steel into thin sheets and subsequently annealing them to create a specific crystal structure. This structure comprises grains oriented in a particular direction, facilitating high magnetic anisotropy. This characteristic means that the steel exhibits distinct magnetic properties in various directions, which, in turn, leads to the efficient manipulation of magnetic fields and the reduction of energy loss attributed to eddy currents.

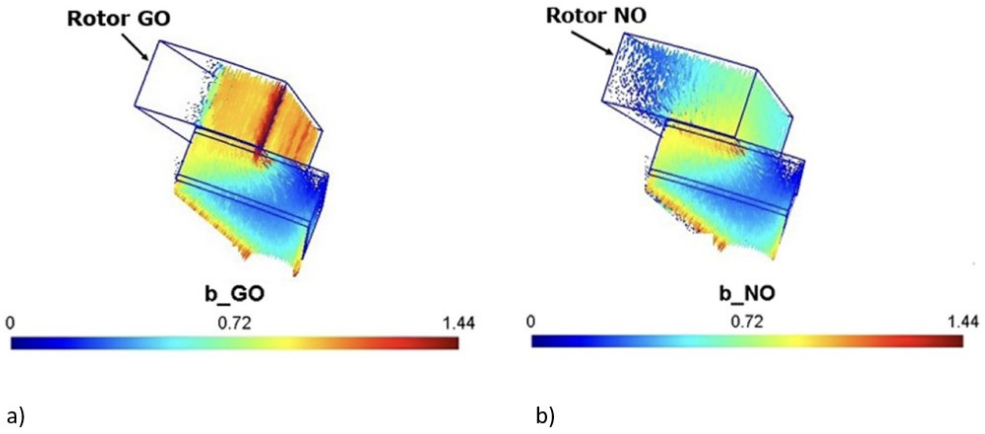

Figure 1.4: a) GOES influence on the flux path. b) NOES flux path. Source: [1]

The orientation of these grains is achieved by meticulously controlling the cooling process during annealing. The resultant material boasts a highly uniform structure, ensuring consistent magnetic performance across the entire sheet. Consequently, GOES finds application across a wide spectrum of electrical devices, including power transformers, motors, and generators, thanks to its remarkable ability to efficiently convert electrical energy into magnetic energy and vice versa.

This discussion pertains to Article [1], which investigates the performance of an axial-flux switched reluctance machine (AFSRM) with a rotor crafted from GOES, comparing it against a rotor composed of non-oriented electrical steel (NOES). The unique structure of the AFSRM lends itself well to GOES integration, particularly within the rotor. In order to assess the intrinsic capabilities of the AFSRM, numerical simulations were conducted to evaluate self-inductance versus rotor position and static torque at a specific operating point. These metrics serve as indicators for comparing the performance of NOES and GOES. The introduction of GOES to the rotating machine led to improvements in electromagnetic torque, with significant enhancements in mean and maximum values. The results (Figure 1.4) demonstrate the positive impact of GOES on machine performance, offering a more efficient torque-to-weight ratio.

Looking ahead, future research may involve an analysis of GOES integration throughout the entire magnetic circuit. However, it's essential to address potential convergence challenges when investigating the 3D model to strike a balance between convergence and result accuracy for specific rotor positions.

Article [2] also utilises Grain-Oriented Electrical Steel (GOES) in an axial-flux switched reluctance motor (AFSRM) to optimise its torque characteristics. This approach capitalises on GOES's excellent magnetic properties along its rolling direction. By dividing GOES into sections and arranging them in the rotor and stator teeth to align with the magnetic flux's rolling direction, the study achieves a substantial improvement in the AFSRM's performance. In particular, the maximum electromagnetic torque exhibits a remarkable 20.5% increase when compared to conventional non-oriented electrical steel motors under identical conditions. The rotor retaining ring comprises epoxy resin lamination to secure the rotor teeth modules, with thermal and stress analyses conducted under fault conditions to verify the retaining ring's reliability. Furthermore, the study involves the construction of an AFSRM prototype and subsequent experiments to validate the calculated data.

This research introduces a novel AFSRM topology suitable for GOES applications, enabling the magnetic field to predominantly align with the rolling direction of GOES within the stator and rotor teeth. The results demonstrate that through the use of GOES and this novel design, machine torque can be significantly improved by over 20% compared to conventional AFSRMs. A prototype validates the design's efficacy, potentially positioning this novel AFSRM topology, combined with GOES material, as a promising candidate for applications demanding high torque density, such as in-wheel motors.

In alignment with the discussion on enhancing the performance of electric motors for transportation applications, it is worth noting the relevance of axial-flux motors, particularly in the context of hybrid scooters. As presented in Article [3], switched reluctance motors (SRMs), characterised by their simplicity, ruggedness, reliability, and lower hysteresis loss, have generated considerable attention for such applications due to their unique advantages.

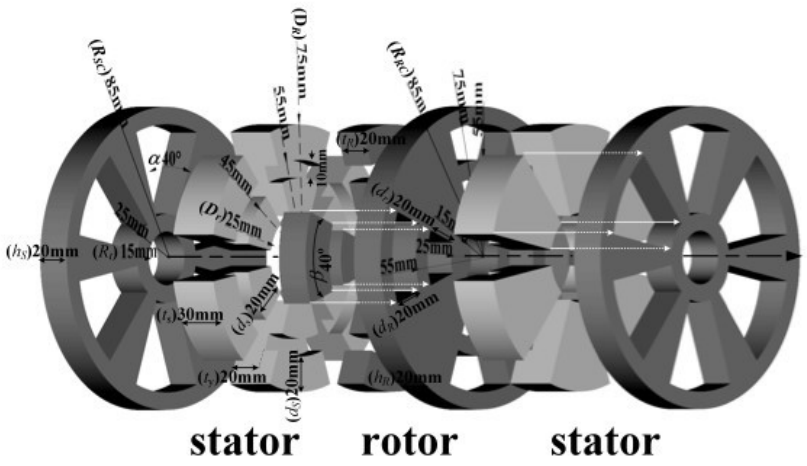

Figure 1.5: Structure and geometry of 6/4 DSRM. Source: [3]

This paper introduces an axial-flux disk-type switched reluctance motor (DSRM) tailored for hybrid scooters (Figure 1.5), offering dual functionality as a scooter drive motor and an engine starter. The choice of an axial flux motor in this context is driven by its superior torque density compared to radial flux motors. Instead of employing finite element analysis (FEM), the study utilises a permeance model to characterise the DSRM. Analytical expressions are employed to dynamically determine output torque and current, enabling further optimisation of the DSRM's geometries.

Crucially, the research establishes a hardware-in-the-loop (HIL) simulation environment to conduct full system simulations, demonstrating the DSRM's suitability as an auxiliary power source for hybrid scooters. Given the high emissions and low fuel economy associated with petrol scooters in urban areas, the hybrid scooter concept has gained prominence as a viable alternative, integrating both a petrol engine and an additional electric motor to address issues like low acceleration and limited cruising time.

In essence, this study highlights the growing interest in SRMs for transportation applications and underscores the advantages of axial-flux motors, such as the DSRM, in enabling more efficient and eco-friendly hybrid scooter designs. By harnessing the axial flux distribution, these motors offer higher torque-to-volume ratios and increased power density, contributing to improved fuel economy, reduced urban air pollution, and extended mileage limitations, ultimately promoting the transition toward sustainable transportation solutions.

Axial flux motors exhibit a unique adaptability to various structural configurations, a feature underscored in articles [4], [5], [6] and [7] with comprehensive elucidation provided in article [8], which outlines the three principal categories of Axial-Flux Switched Reluctance Motors (ASRMs):

- **ASRM with Single Stator and Single Rotor:** In this category, a sole stator and a solitary rotor are employed, resulting in a singular air-gap (see Fig. 1.6a). However, this configuration introduces an inherent challenge—unbalanced axial magnetic forces. Consequently, robust measures for guiding the rotor are imperative. An example is presented in Ref. [9], where a 6/4 configuration of 2.7 kW ASRM is described. Notably, this motor wasn't tested at its rated speed due to the occurrence of rotor teeth contacting stator teeth, a consequence of the unbalanced axial force.

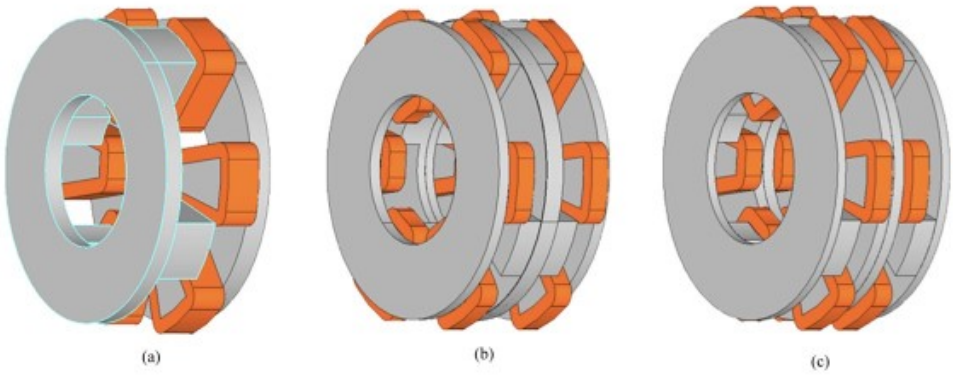

Figure 1.6: ASRM categories: (a) ASRM with single-stator and single-rotor, (b) ASRM with double-stator and single-rotor, (c) ASRM with single-stator and double-rotor. Source: [8]

- **ASRM with Double Stator and Single Rotor:** This design features a single rotor positioned between two stators (Fig. 1.6b), resulting in two air-gaps. An advantageous feature is the balancing of axial forces, as each stator's axial force on the rotor is counteracted by the other stator. To mitigate torque ripples, an angular shift of the stators can be employed [7]. While patent [10] introduces this configuration and employs a rolling method for motor lamination, the specific details are somewhat limited. Nevertheless, claimed benefits encompass reduced torque ripples, noise, vibrations, and iron losses. Notably, a solution for retaining rotor teeth without the rotor yoke is not provided. Acoustic advantages of this structure are emphasised in Ref. [11].
- **ASRM with Single Stator and Double Rotor:** This category features a single stator positioned between two external rotors (Fig. 1.6c), presenting challenges in terms of cooling due to the central stator placement. Patent [12] outlines the adaptation of the radial SRM concept into an axial configuration with a double rotor, albeit without comprehensive calculations. Notably, the use of global coils complicates winding insertion and increases manufacturing costs. Furthermore, the patent lacks a detailed study validating proclaimed benefits such as higher efficiency, reduced copper loss, improved thermal performance, lower torque ripple, increased torque density, and lower production costs. Authors in Ref. [13] have applied this motor in automotive traction, while Refs. [14] and [15] introduce ASRMs with segmental rotors for traction applications. In Ref. [14], a novel rotor shift is proposed to mitigate torque ripples without causing axial force imbalances. Meanwhile, in article [15], the machine incorporates more rotor teeth than stator teeth to enhance torque density.

1.3.2 Solutions With Permanent Magnets

Achieving higher peak performance levels in contemporary technologies necessitates the integration of permanent magnets. In the research presented in paper [16], the focus centres on dual-rotor axial-flux permanent magnet (DRAFPM) machines characterised by a modular stator (MS) and tooth-wound fractional slot non-overlapping winding (FSNW), designed explicitly for electric vehicles (EVs). This investigation encompasses four distinct machines, each distinguished by varying rotor topologies: Surface-Mounted Permanent Magnet (SPM), Concentrated Permanent Magnet (CPM), Hybrid Core Permanent Magnet (HCPM), and Interior Permanent Magnet (IPM):

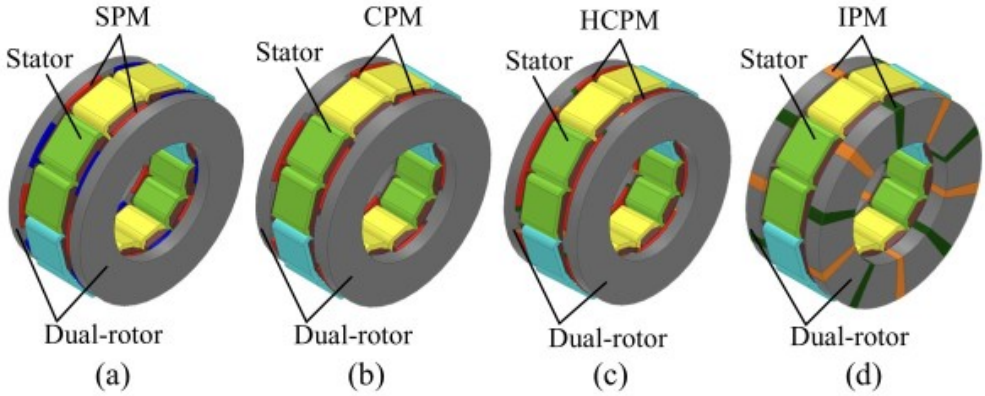

Figure 1.7: The proposed DRAFPM machines with different rotor topologies. (a) DRAFPM with SPM rotor. (b) DRAFPM with CPM rotor. (c) DRAFPM with HCPM rotor. (d) DRAFPM machine with IPM rotor. Source: [16]

A parameter sensitivity analysis reveals intriguing findings. Notably, the introduction of an air barrier within the CPM structure serves to mitigate magnetic flux leakage, thereby augmenting output torque. Additionally, the inclusion of tangential permanent magnets in the HCPM configuration effectively reduces back-EMF harmonics.

Furthermore, in the comparative study of electromagnetic performance, it is evident that the SPM motor attains the highest average output torque. Remarkably, the CPM machine consumes permanent magnets equivalent to 73.6% of the volume required by the SPM machine, while achieving an impressive 86.1% of the torque output. Consequently, the output torque per unit of permanent magnet volume in the CPM configuration surpasses that of the SPM by 17%.

Moreover, both the CPM and IPM machines exhibit reluctance torque, with IPM machines displaying a higher proportion of reluctance torque. Simultaneously, their d-axis inductances surpass that of the SPM due to reduced reluctance, resulting in a wider range of speed regulation.

Lastly, the IPM machine stands out in terms of its capacity to withstand permanent magnet demagnetisation and minimal rotor losses. These attributes contribute to high efficiency and enable the accommodation of overload armature currents, underlining its potential for robust and efficient operation.

In cases involving the incorporation of permanent magnets, as exemplified in articles [1] and [2], article [17] introduces a notable advancement by employing grain-oriented (GO) silicon steel in an axial-flux permanent magnet (AFPM) machine, strategically enhancing both its torque and efficiency.

The utilisation of GO silicon steel entails a meticulous examination of the rolling direction to ensure that the machine's primary magnetic flux aligns with the material's easy magnetisation direction. Based on a comprehensive investigation into the electromagnetic characteristics of the AFPM machine, GO silicon steel is employed to create a stator with a prescribed lamination direction. The outcome of this innovation is a notable increase in torque and efficiency compared to conventional non-oriented (NO) silicon steel machines operating under identical conditions.

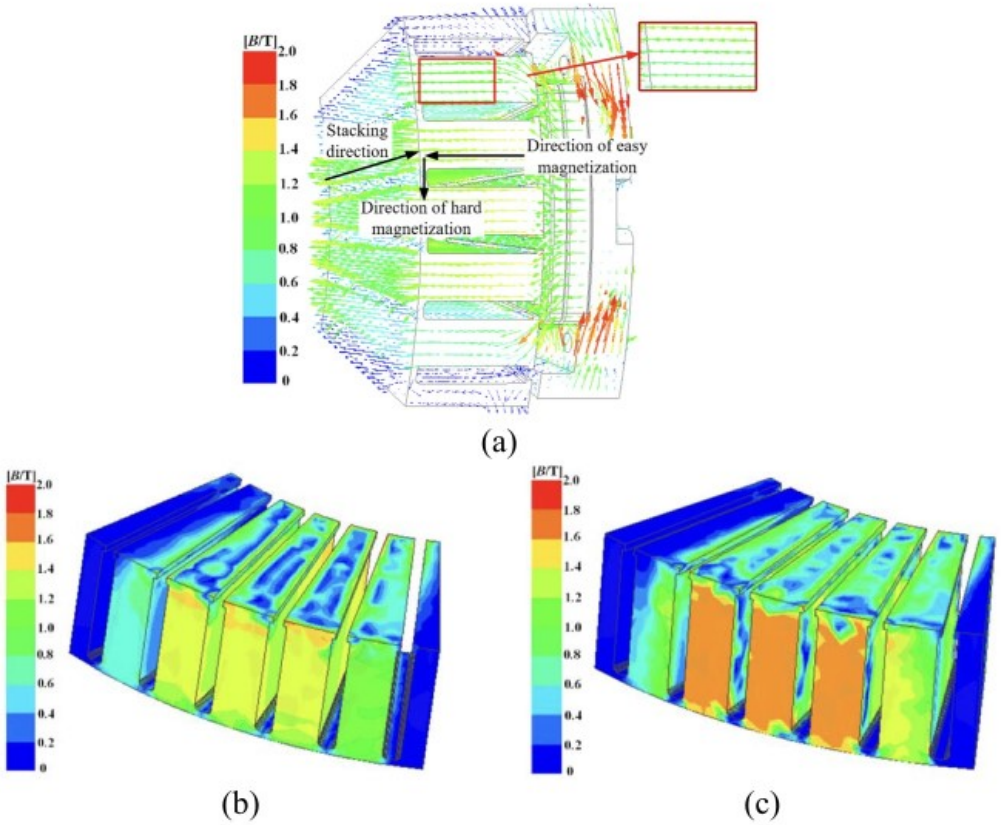

Figure 1.8: Field distributions and flux density under no load. (a) Field distributions. (b) Flux density of GO material. (c) Flux density of NO material. Source: [17]

Additionally, an equivalent magnetic circuit model is formulated to illustrate the minimal discrepancy in electromagnetic properties under no-load conditions when employing two types of silicon steel sheets in the yokeless stator AFPM machine. Furthermore, an AFPM machine with a stator yoke is established to underscore the advantages of GO material in the context of yokeless stator AFPM machines.

By introducing GO material into the yokeless stator AFPM machine, the objective of this article is to leverage its electromagnetic anisotropy to enhance torque performance, diminish core losses, and augment overall efficiency. Leveraging a 3-D Finite Element Analysis (FEA) model of a 48-slot / 8-pole AFPM motor, comprehensive comparisons have been made regarding field distributions, flux density, torque output capacity, and efficiency maps between GO and NO materials (Figure 1.8).

The introduction of GO material in conjunction with the yokeless stator structure results in a commendable 3% increase in the torque output capacity of the AFPM machine, accompanied by a noteworthy 10% reduction in core losses and a substantial improvement in overall efficiency. Furthermore, this article delves into the examination and verification of the inapplicability of GO material in AFPM machines with stator yokes through FEA analysis.

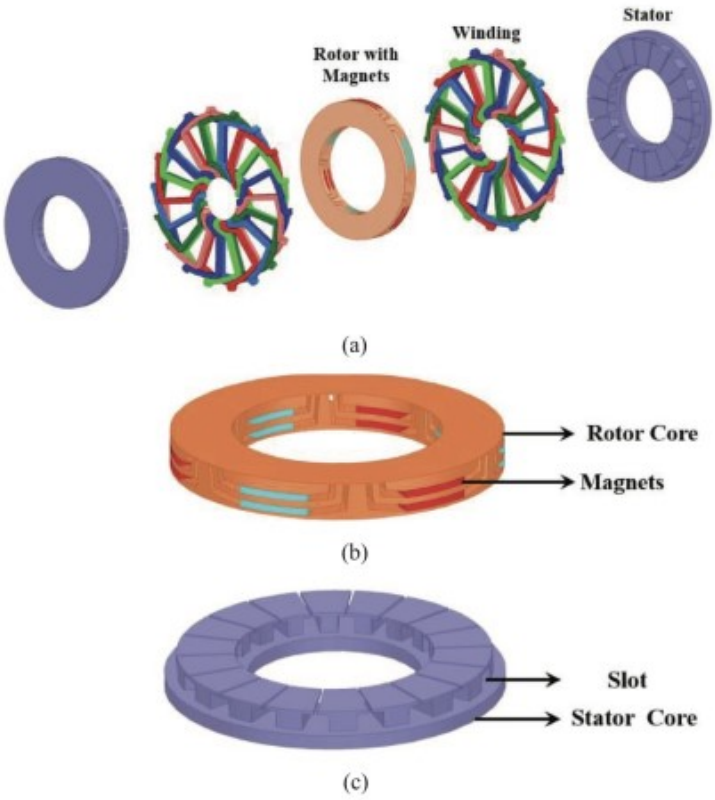

Figure 1.9: (a) Exploded view of AFPMa-SynRM, (b) Rotor of AFPMa-SynRM and (c) stator of AFPMa-SynRM. Source: [18]

Axial flux permanent magnet (AFPM) motors, renowned for their elevated power and torque densities as well as simplified construction, find application across various domains. The majority of AFPM motors conventionally employ surface-mounted permanent magnets to generate torque, resulting in reduced saliency and reluctance torque. Consequently, these motors typically exhibit a limited flux weakening range.

Paper [18] introduces an innovative solution: the axial flux permanent magnet assisted synchronous reluctance motor (AFPMa-SynRM) (Figure 1.9). This novel motor design offers not only the advantages of magnet torque but also a significantly higher reluctance torque, while requiring a reduced quantity of magnet material.

To optimise the AFPMa-SynRM's performance, a Taguchi method-based approach has been systematically employed to enhance torque per unit volume while concurrently minimising torque ripple. Comparative assessments have been conducted between the electromagnetic and flux weakening performances of the AFPMa-SynRM and a benchmark axial flux interior permanent magnet (AFIPM) motor.

The findings from this study indicate that the AFPMa-SynRM presents a compelling and potentially cost-effective solution, outperforming the benchmark AFIPM model. Notably, the AFPMa-SynRM demonstrates a capacity to provide increased saliency and a broader speed range, making it a promising choice for applications demanding an extended flux weakening range.

1.3.3 Hybrid Radial and Axial Flux Permanent Magnet Machine

Axial leakage magnetic flux arises in the spoke-type interior permanent magnet synchronous motor (IPMSM) due to the design of the flux-concentrating rotor structure. This phenomenon adversely affects the motor's performance. The study made in article [19] begin with the fabrication and test of a conventional spoke-type interior permanent magnet (IPM) motor. Subsequently, an innovative spoke-type IPM rotor (Figure 1.10), designed to combine both radial and axial flux-concentrating capabilities, is introduced with the objective of minimising interpolar flux leakage and enhancing torque performance.

Moreover, radially magnetised permanent magnets are strategically positioned along the inner circumference of the rotor to mitigate internal flux leakage. The effectiveness of these two proposed structural modifications is rigorously evaluated through comprehensive three-dimensional finite-element analysis (3-D FEA).

The core focus of this investigation lies in the development of a novel rotor that combines radial and axial flux concentration, reducing leakage flux within the spoke-type permanent magnet rotor. To analyse leakage flux and electromagnetic performance, 3-D models of concentrated winding permanent magnet motors has been established employing different rotor configurations.

To further validate the significance of the 3-D FEA in accounting for flux leakages, a 12-slot ten-pole concentrated winding motor equipped with a spoke-type IPM rotor is manufactured and subjected to experimentation. The 3-D FEA findings reveal substantial improvements, demonstrating a 58.1% reduction in axial leakage flux and a 61.7% decrease in rotor-interior leakage flux.

Consequently, the novel rotor designs contribute to an enhancement in electromagnetic torque, with improvements of 2.81% and 5.48% achievable when subjected to a 30 Arms phase current input in an 8 kW prototype motor. These advancements come without an increase in permanent magnet consumption.

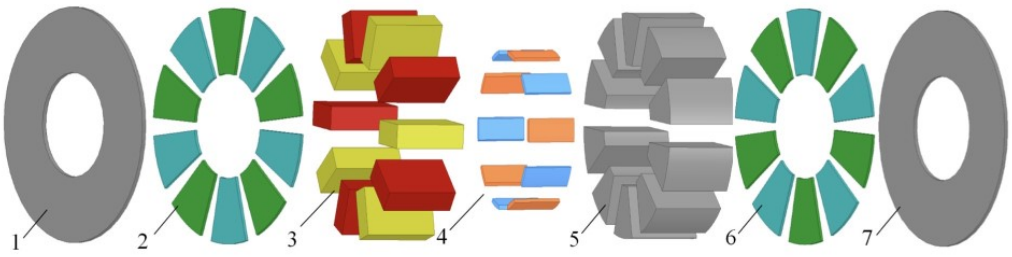

Figure 1.10: Exploded view of the second novel rotor (1 and 7 are the rotor yoke, 2 and 6 are axially magnetised PM, 3 is the tangentially magnetised PM, 4 is the radially magnetised PM, 5 is the rotor). Source: [19]

Paper [20] introduces a design and analysis approach for a high-power density hybrid flux permanent-magnet (PM) machine. This innovative machine combines the principles of radial and axial flux machines, incorporating integrated windings to boost air-gap flux density. Additionally, it implements an overhang structure for the PM and introduces supplementary magnetic cores to enhance power density.

Given the distinctive structural characteristics of the proposed motor, a thorough 3-D finite-element analysis (FEA) is essential for its analysis and design. To address the computational time constraints associated with such an approach, we present a novel and efficient analysis method, utilising a 2-D equivalent conversion technique.

Notably, this research highlights the significant contribution of the novel hybrid flux machine to the realm of high-power density machines. Equally important is the development of an accurate and expedient analysis method that accommodates the unique 3-D structure of the Hybrid Flux Permanent-Magnet Machine (HFPMM) (Figure 1.11). This analysis method has broad applicability, particularly for the design of motors with non-uniform stack lengths and material properties.

It is pertinent to mention that this study primarily focuses on the magnetic field distribution under no-load conditions. Future research endeavours will delve into extended analyses, including the calculation of iron losses, which will further demonstrate the utility of the proposed analysis method.

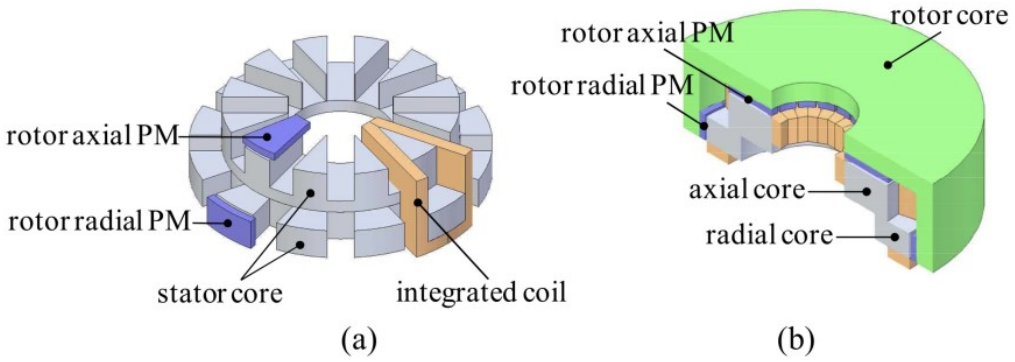

Figure 1.11: Basic structure of the HFPMM. (a) Assembled structure. (b) Cross-sectional view. Source: [20]

1.4 Cooling Systems for Electric Motors

This section of the report is dedicated to the examination of contemporary technologies available for enhancing the cooling systems of electric motors. The primary objective is to explore potential solutions that can increase power densities and, ideally, the efficiencies of propulsion systems. It is crucial to avoid any excessive enlargement of the core or copper components. Furthermore, implementing these measures can contribute to the improvement of the performances of switched reluctance, synchronous reluctance and assisted reluctance machines, thereby reducing reliance on rare earth materials. The main goal is to prevent any detrimental drops in performance, such as torque, power, and power density, in comparison to permanent magnet motors.

Moving to the review of cooling systems, the literature reports many studies and solutions aimed at increasing current and power densities in electrical machines for traction purposes. Among the most common cooling methods, liquid (water, water-glycol and oil) cooling strategies with their possible combination with air-cooled systems are capable of ensuring a significant increase in performances. Indeed, air cooling strategies alone cannot ensure the required performances for automotive applications due to the compact size of the machine. Additionally, certain approaches incorporating phase changes in the coolant are also worth mentioning. The solutions discussed in the following sections are primarily applicable to permanent magnet synchronous motors, with a focus on radial flux machines. Nevertheless, many of these approaches can be adapted for use in axial flux motors. Numerous cooling strategies outlined in these paragraphs have successfully pushed current density well beyond 10 A/mm^2.

The most common ideas for cooling electric machines in electric vehicle propulsion are detailed in [21], encompassing jacket cooling of the housing, end winding cooling and shaft cooling. Alternatively, [22] presents an extensive review of practical cooling system examples with an emphasis on aircraft applications, many of which can be adopted in electric cars. These solutions are categorised as follows:

- Housing cooling
- Enhanced stator core cooling
- Enhanced winding cooling
- Enhanced rotor cooling

This classification is retained throughout this paragraph and is supplemented with insights from other studies.

1.4.1 Housing Cooling

The classification in [22] comprises enclosed housing fan-cooled and indirect jacket-cooled machines, with references to [23], [24], [25], [26], [27], [28]. The primary advantage of housing cooling systems is that they have minimal impact on the internal electromagnetic structure of motors, as depicted in Figure 1.12. This makes them the preferred choice for engineering applications. The principle behind this strategy is that the heat generated in the windings, magnets, and iron core is transferred to the housing via the stator core in radial machines. Subsequently, air or liquid convection facilitates the removal of heat. In particular, [28] proposes the use of paraffin phase-change material as a coolant.

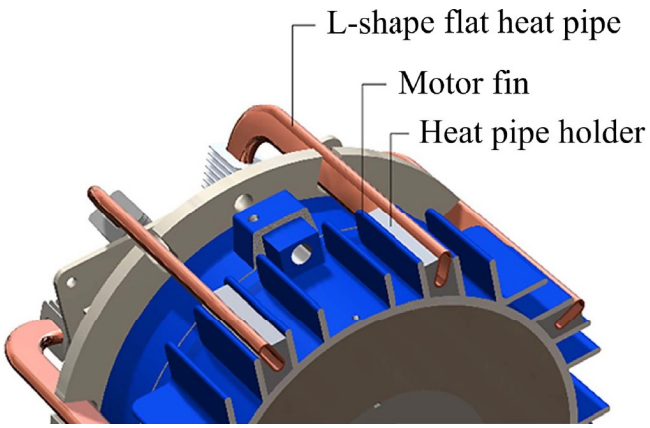

Figure 1.12: Installation of L-shaped pipes on motor fins. Source: [27]

1.4.2 Stator Core Cooling

As outlined in [22], it introduces various strategies for cooling the stator directly within the machine's housing. This improvement is necessary because iron losses contribute to a substantial portion of overall machine losses, particularly in high-speed motors. To address this issue, some researchers have introduced cooling channels in the stator back instead of relying on heat convection within the housing.

Direct contact between the coolant and the stator core is advantageous, as it places the coolant closer to the heat source, eliminating the thermal resistance associated with the housing. [29] suggests the use of oil-cooling grooves in the stator back, as shown in Figure 1.13.

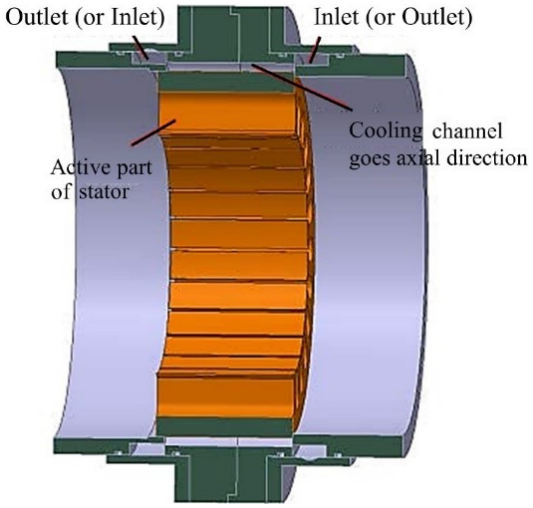

Figure 1.13: Direct-cooled motor. Source: [29]

[30], [31], [32] propose oil-flooded cooling to ensure contact between the entire stator and the coolant. This approach can also be adapted for use in axial flux permanent magnet motors. [32] suggests an enclosure made of glass fibre for the stator, enabling oil injection into the stator for direct contact with the core and windings, as depicted in Figure 1.14. It is noteworthy that oil-flooded stator cooling is significantly more efficient in terms of heat removal than stator back-channel cooling. However, it necessitates an external fluid circulation system (comprising coolant, pump, tube, tank, and heat dissipation unit), which may increase the system's weight and complexity.

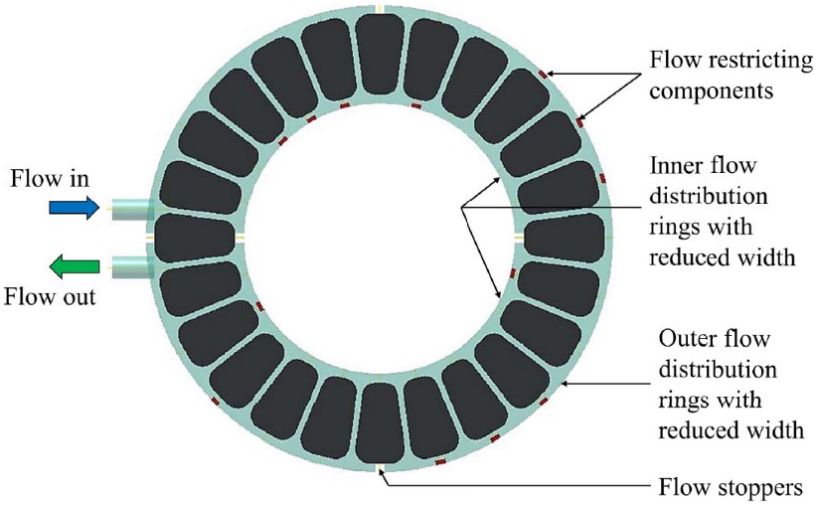

Figure 1.14: Oil-flooded stator of an axial-flux motor. Source: [32]

[33], on the other hand, proposes the insertion of water-cooled plates in a permanent magnet synchronous motor with concentrated windings. In this arrangement, three plates are inserted into the stator core laminations: one in the centre and two at the ends. This approach shortens the thermal path between heat sources and the coolant. The plates are made of aluminium alloy and enclose a water channel. Additionally, the end winding and the rotor can be indirectly cooled due to the reduced overall temperature of the stator.

1.4.3 Winding Cooling

As emphasised in [22], highlights that hot spots typically develop in the windings, leading to copper loss and potential damage to insulation coatings. Consequently, various advanced thermal designs have been proposed to facilitate heat extraction from the windings. One possible solution involves cooling the end winding, achieved by using potting materials to fill the gap between the end windings and the frame. This filler material establishes a conductive pathway to the housing. In particular, [34] and [35] combined a housing liquid-cooling system with potting material for radial-flux and axial-flux permanent magnet electrical machines, respectively, as illustrated in Figure 1.15.

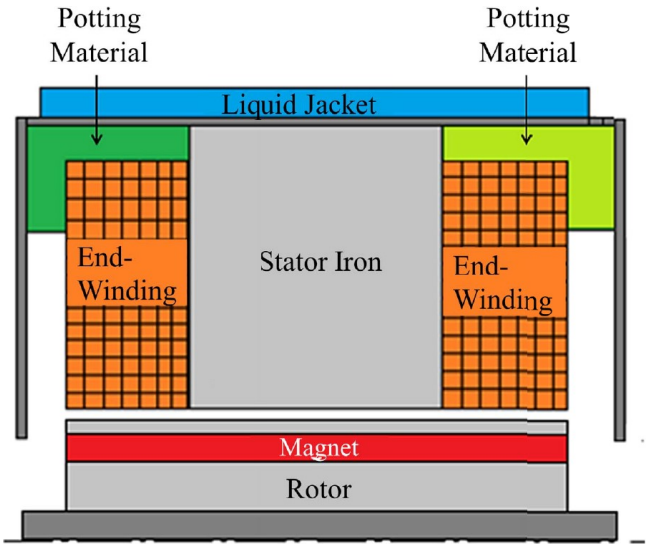

Figure 1.15: Radial flux synchronous motor with potted material and liquid housing cooling system. Source: [34]

[22] also presents an alternative filler material. The main drawback of this approach is the increased weight resulting from the replacement of air with the filler material. Additionally, potting materials must provide high electrical insulation and mechanical strength requirements at elevated temperatures. Another method for winding cooling involves oil spray cooling, as detailed in [36], [37] and [38]. In these systems, nozzles inject oil directly onto the end windings, taking advantage of the higher convective heat transfer coefficient of oil compared to air cooling. Notably, [38] incorporates water jackets, rotor blades, and oil injection onto the end winding, as shown in Figure 1.16.

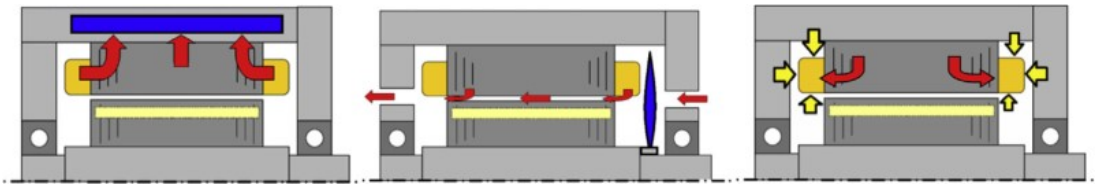

Figure 1.16: cooling strategy proposed in [38] which foresees water jackets, blades on rotor and oil injection on coil end-windings (heat flow in red).

It is worth highlighting the view expressed in [22] where oil spray cooling is inferior to oil-flooded cooling. While both systems require an external oil circulation system, the oil-flooded strategy ensures uniform heat removal. [39] proposes an annular cooling pipe positioned directly within the end windings, creating an additional cooling path and increasing the heat transfer area (Figure 1.17). This approach is well-suited for electrical machines with distributed windings. On the other hand, in-slot winding cooling proves more effective for motors with concentrated windings, ensuring direct contact between the coolant and the heat source throughout the machine's length. The concept involves placing the edges of the cooling duct in contact with the coils and/or the stator core.

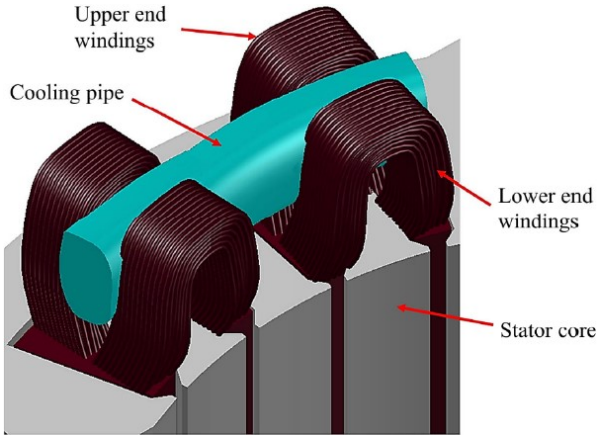

Figure 1.17: Annular cooling pipe on end windings. Source: [39]

Other potential solutions include the use of heat pipes [40], [41], [42], [43], which enclose a phase-changing coolant, facilitating heat transfer from a source to a heat sink with minimal thermal resistance. It should be noted that round heat pipes are suboptimal due to their limited heat transfer area. [44] introduces improvements involving microchannel heat exchangers positioned in contact with in-slot windings, and [45] suggests the placement of axial cooling channels and flat wires, as illustrated in Figure 1.18.

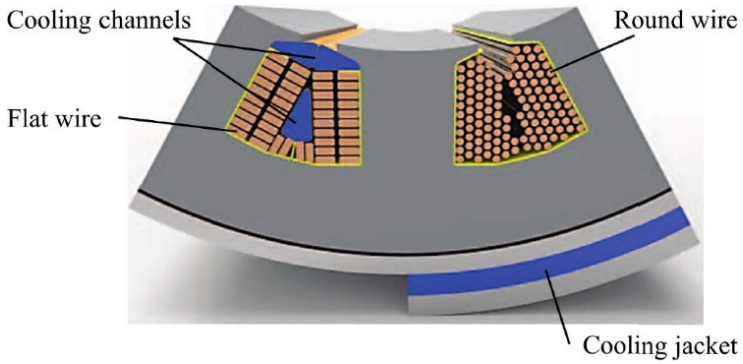

Figure 1.18: Flat wires combined with slot channels. Source: [45]

Various arrangements are possible, such as locating the cooling channels on the innermost side of the slot [46]. Additionally, hydrogen can be used as a coolant owing to its high thermal conductivity, low viscosity, density, and friction compared to water. It is also suitable for ventilation cooling at the air gap, as designed in [47]. It is important to recognise the trade-off between the filling factor of the slots and cooling area in these liquid-cooling methods. Cooling ducts reduce space available for windings, but improved cooling enables higher allowable current densities. An advancement in direct cooling involves the use of hollow conductors [48], entailing coaxial wires on cooling channels that provide a direct heat path to the coolant for each conductor. However, this strategy also faces trade-offs: the wall thickness must strike a balance between withstanding coolant pressure and minimising the reduction in the filling factor or number of turns. Additionally, the overall cooling system becomes more complex and less flexible than previous methods. Direct slot cooling is explored in [49], where all cooling channels are arranged hydraulically in parallel to reduce pressure drop, with each slot housing two or more thin-walled plastic tubes, as shown in Figure 1.19. To prevent freezing, chemical inert fluids with low viscosity and high temperature tolerance are necessary, with polysiloxane fluids emerging as suitable coolants.

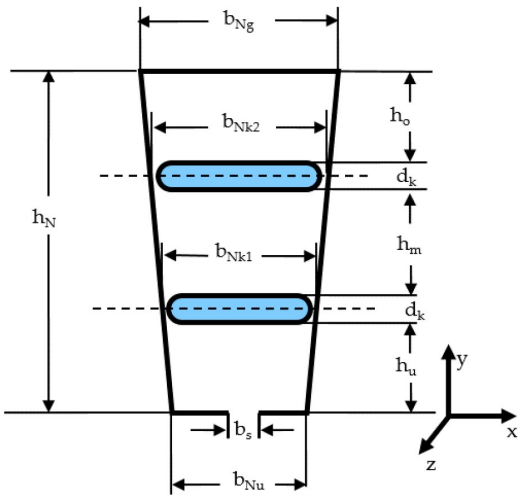

Figure 1.19: Stator slot with two distributed cooling channels for direct slot cooling. Source: [49]

[50] proposes the use of 3D-printed direct winding heat exchangers in a permanent magnet synchronous motor with concentrated windings. These T-shaped exchangers are hollow, allowing coolant to flow within them, and are positioned in the gaps between windings, as seen in Figure 1.20. Water was chosen as the coolant in this prototype.

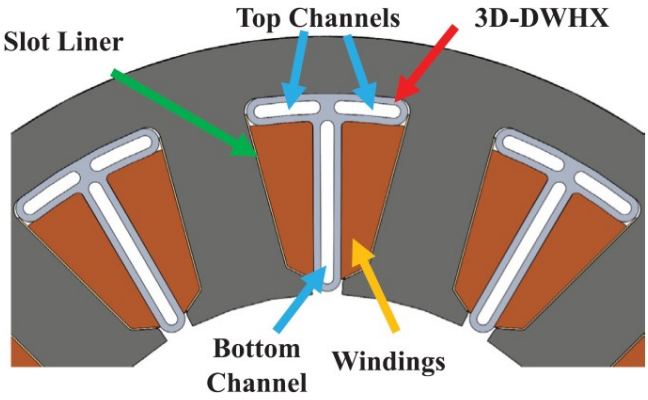

Figure 1.20: 3D printed heat exchangers and their arrangement on the stator of a concentrated winding machine. Source: [50]

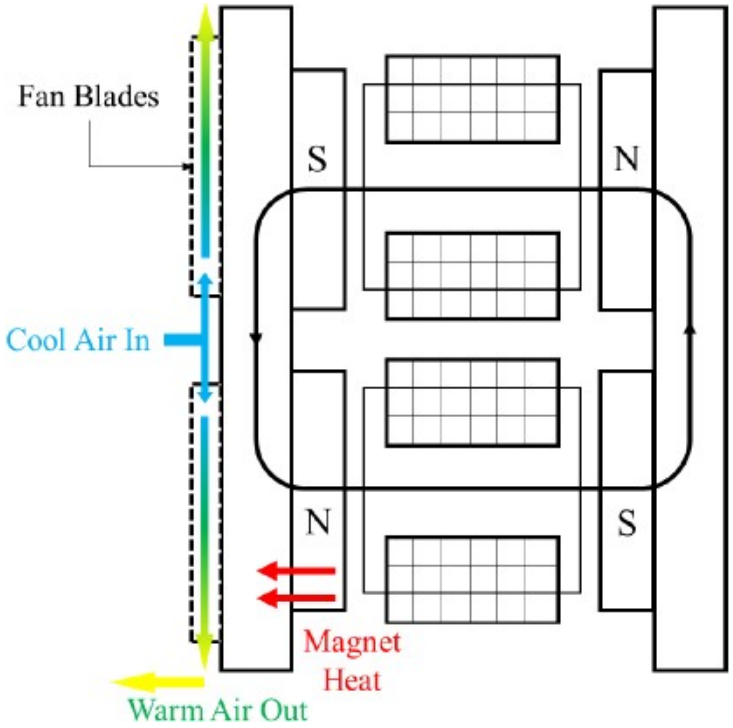

Figure 1.21: Fan attached to the rotor of an axial-flux machine. Source: [51]

1.4.4 Enhanced Rotor Cooling

As mentioned in [22], is particularly relevant for permanent magnet electrical machines, which can achieve relatively high power densities. However, elevated rotor temperatures can impact the performance of permanent magnets. Consequently, rotor cooling must be carefully considered. Forced air cooling remains the predominant solution [52], [53], [54], [51]. [51] introduces a design for a dual-rotor axial-flux permanent magnet machine featuring a fan mounted coaxially with a rotor disk, as illustrated in Figure 1.21. One drawback of this approach is the increased friction and windage losses associated with high-speed operations. A potential countermeasure involves incorporating hollow shafts [55], [56], allowing coolant to flow within the shaft. While effective, this solution introduces design complexities related to system reliability, watertightness, and mechanical strength under high torque conditions. Figure 1.22 combines hollow shaft cooling with air-cooled housing.

Similar solutions to those presented in [22] are also discussed in [57], [58] and [59]. [57] provides a fundamental overview of forced air and liquid cooling, delving into potential housing cooling methods (using air or water jackets). Stator cooling solutions involve cooling slots in the yoke or slots, as well as wet stator designs where the stator is flooded with coolant contained within a sleeve. For rotor cooling, [57] mentions direct liquid cooling, although it is acknowledged as a more complex and costly solution.

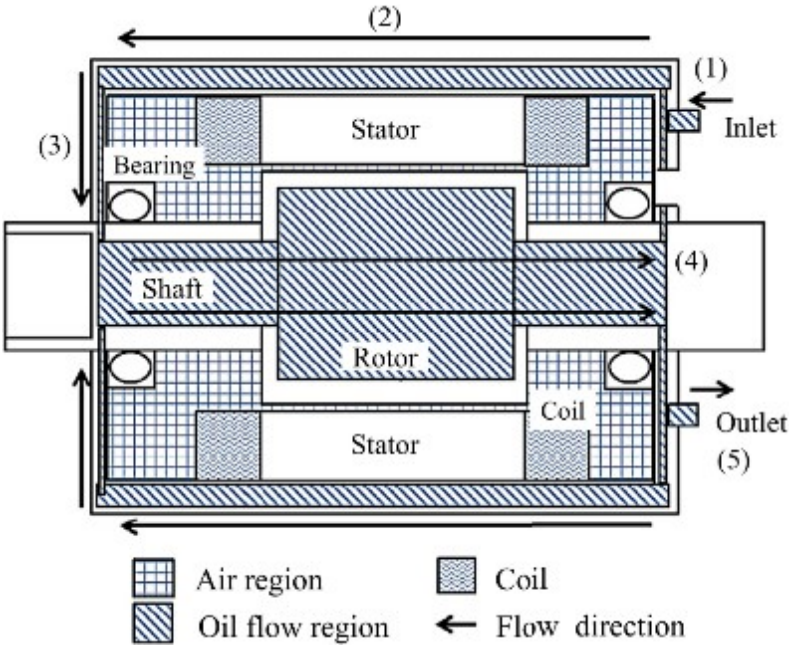

Figure 1.22: hollow shaft for rotor cooling combined with housing cooling. Source: [56]

As an alternative, [57] suggests annular cooling or hollow shaft cooling. The report in [57] also outlines phase change cooling, emphasising its application in heat pipes. It further suggests that high-power-density machines may require hybrid cooling methods, combining multiple approaches to cool the motor. Furthermore, practical examples, including an analysis of the cooling method adopted in the Nissan Leaf motor, are presented. [58], on the other hand, examines cooling methods for different components of a typical automotive electric powertrain.

For electric motors, it categorises direct and indirect stator core cooling, stator winding cooling, and end winding cooling, offering further sub-classifications based on the type of coolant or cooling method. [59] revisits avionics and highlights a few examples of oil bath cooling, water jacket cooling of the housing using circular, serpentine, or helical ducts. The report also mentions heat pipe cooling, which can utilise single or double-phase change coolants. Lastly, it is important to mention the book [60], which provides case studies in thermal management for electrical machines. These case studies encompass:

- Totally enclosed non-ventilated motors
- Totally enclosed fan-cooled motors
- Open ventilated cooled motors
- Closed circuit cooling with a heat exchanger
- Water jacket cooling of the housing
- Flooded stator cooling
- Hybrid solutions combining multiple methods

The aim of this section is to provide an objective and impersonal overview of the various cooling technologies and strategies available for electric motors, as well as their potential applications and advantages.

Chapter 2

Axial Flux Electrical Machines

In this section, the key characteristics of stator core-less axial flux permanent machines are discussed in detail. Axial flux permanent machines (AFPMs) are electric machines that utilise a axial magnetic flux path, unlike traditional machines with a radial flux path.
From a construction perspective, brushless AFPM (Axial Flux Permanent Magnet) machines offer various design options. These machines can be categorised based on whether they are single-sided or double-sided, their inclusion or exclusion of armature slots and cores, their use of internal or external PM rotors, their choice of surface-mounted or interior PMs, and whether they operate as single-stage or multi-stage machines. In the case of double-sided configurations, the choice is between adopting either an external stator or external rotor arrangement. Opting for the first choice means using fewer permanent magnets, but it may result in less efficient winding utilisation. On the other hand, the second choice, with an external rotor, is considered a highly advantageous machine topology. In summary, the design possibilities for brushless AFPM machines are diverse and can be classified as follows:

- single-sided AFPM machines
  - with slotted stator
  - with slotless stator
  - with salient-pole stator
- double-sided AFPM machines
  - with internal stator
    - with slotted stator
    - with slotless stator
      - with iron core stator
      - with coreless stator
      - without both rotor and stator cores
    - with salient-pole stator
  - with internal rotor
    - with slotted stator
    - with slotless stator
    - with salient-pole stator

It is also possible to have multi-stage (multidisc) AFPM machines.

The choice for the application in exam has landed on a double sided axial flux permanent magnet machine with internal stator without stator core. The absence of stator cores is a distinctive feature of some AFPM designs, which can have various advantages in terms of efficiency, weight, and compactness:

- **Stator Core Elimination:** In traditional electric machines, the stator core is a significant component that contributes to magnetic losses, weight, and manufacturing complexity. In axial flux machines without stator cores, this component is eliminated, simplifying the overall design.
- **Compactness and Weight Reduction:** The removal of the stator core allows for a more compact and lightweight machine design. This can be particularly advantageous in applications where space and weight are critical factors, such as electric vehicles, drones, and other mobile systems.
- **Higher Power Density:** With the elimination of the stator core, the AFPM can achieve higher power densities compared to traditional machines. This means they can deliver more power within a smaller and lighter package.
- **Reduced Eddy Current Losses:** Eddy current losses occur in the stator core of traditional machines due to the variable magnetic field. In AFPMs without stator cores, these losses are significantly reduced, leading to higher efficiency.
- **Improved Cooling:** The absence of a stator core enhances the cooling capabilities of the machine. Heat dissipation becomes more efficient, allowing the machine to operate at higher power levels without overheating.
- **Enhanced Customisation:** The simplified design can make customisation and adaptation to specific applications easier. Engineers can modify the characteristics of the machine to match the requirements of different applications.
- **Challenges in Manufacturing:** While the elimination of the stator core simplifies the design, manufacturing challenges may arise in terms of winding the coils and assembling the machine. Special manufacturing techniques may be required to ensure precise coil placement and alignment.
- **Magnetic Saturation Considerations:** Without a stator core to guide the magnetic flux, there can be challenges related to magnetic saturation and field distribution. Careful design and analysis are necessary to ensure optimal magnetic performance. More in detail, due to the larger gap without any magnetic material, a machine of this type requires a greater amount of permanent magnet material compared to an equivalent machine that incorporates a ferromagnetic stator core.
- **Control and Efficiency optimisation:** The unique design of AFPMs without stator cores may require specialised control algorithms to achieve the desired performance and efficiency. These algorithms would need to account for the unconventional magnetic field distribution.

Overall, axial flux permanent magnets machines without stator cores present a novel solution in electric machine design, offering benefits in terms of compactness, weight reduction, efficiency, and power density. However, their successful implementation requires careful consideration of design, manufacturing techniques, and control strategies to fully leverage their advantages.

As it can be seen in fig.2.1, the considered AFPM machine structure is composed by a coreless internal stator and twin external PM rotor where PMs are glued to the rotors backing steel discs.

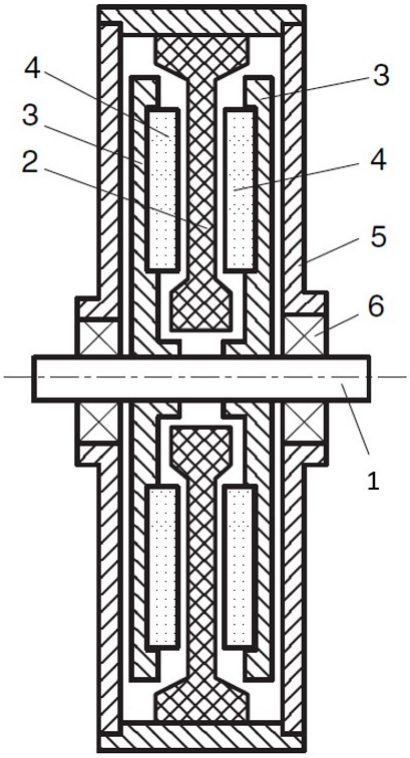

Figure 2.1: Double-sided coreless motor with internal stator. 1 — shaft, 2 — stator winding, 3 — rotor, 4 — PM, 5 — frame, 6 — bearing. Source: [61]

2.1 Winding Configuration

The windings of stator coreless axial flux permanent magnets (AFPM) machines are produced as coils uniformly distributed on a disk-shaped cylindrical support structure, or hub, constructed from non-magnetic and non-conductive materials. Two distinct winding types are employed:

a Windings composed of multi-turn coils, wound with insulated conductors of either round or rectangular cross-section.

b Printed windings, alternatively known as film coil windings.

These coils are organised into groups to create phase windings, commonly interconnected in a star or delta configuration. Within the same phase, coils or groups of coils can be paralleled to form parallel paths. Achieving high-density packing and assembly of identical coils is accomplished by fashioning coils with offsetting bends, as illustrated in Figure 2.2.

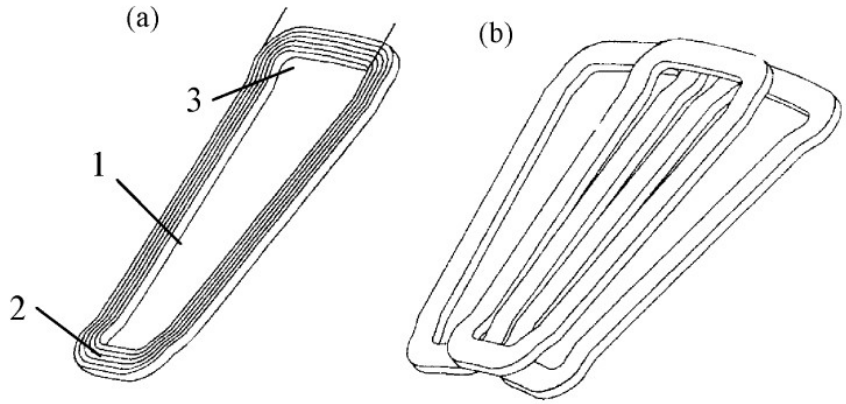

Figure 2.2: A type of coreless winding in the form of a disc is constructed using coils arranged uniformly, following the design from U.S. Patent No. US5744896 (Kessinger R.L., Jr, et al 1998. Interlocking segmented coil array). This winding configuration is shown in two variations: (a) A single coil setup. In this setup: 1) coil side. 2) inner bend that offsets the coil. 3) outer bend that offsets the coil. (b) Three neighbouring coils positioned side by side. Source: [61]

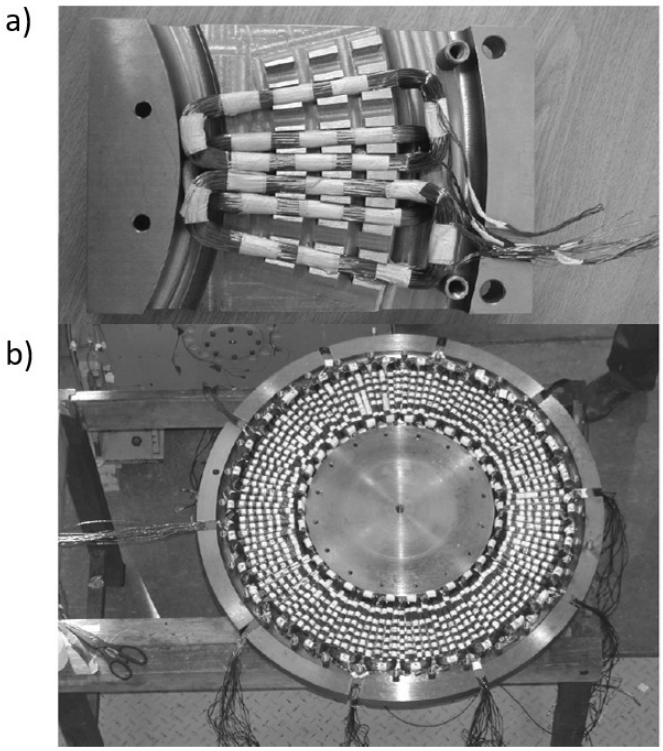

Figure 2.3: Devices for correctly placing the coils into position within the moulds are available in two forms: (a) A mould equipped with guide slots. (b) A mould designed with guide pins. Source: [61]

Coils can be placed into slots in a mould's structure (like in Figure 2.3). Once all the coils are in place, they are enclosed in a mix of epoxy resin and hardener. This mixture hardens when heated in an oven. However, removing the solidified stator from the mould's slot structure (as seen in Figure 2.3a) can be tricky. To make this easier, the guide slots are made with removable pins of various sizes (as shown in Figure 2.3b).

For very small AFPM machines and micromachines, a method called printed circuit coreless winding can be used to automate production. Though, efforts to create printed circuit windings for AFPM brushless machines, similar to printed circuit boards, haven't succeeded in the market due to poor performance.

The following paragraph will be focused on the rules and equations needed to develop an accurate model, but first it is necessary to put some rules for poles and slot combinations for **non-overlapping windings**:

- the number of poles must be even,
- the number of slots must be a multiple of the number of phases,
- the number of coils in a group must be an integer,
- the number of slots cannot be equal to the number of poles,
- the number of coils and slots are equal in double layer windings, while in single layer windings the number of coils is equal to half the number of slots.

2.2 Equations and Parameters of a Coreless Stator AFPM Machine

The model under development is a three-phase, Y-connected axial flux motor with nominal velocity measured in revolutions per minute rpm. This motor features a coreless stator and a twin external rotor equipped with permanent magnets (PMs) on the surface and a backing steel disc. The values of residual induction B_r and recoil permeability μ_{rrec} are provided by the manufacturer of the PMs. In addition to these crucial parameters, other factors to take into account are the non-magnetic distance between opposite PMs t, the winding thickness t_w, and the height of the PMs in axial direction, h_M. Outer and inner diameters of PMs, for simplicity, are considered equal to the values of the outer and inner diameters of stator conductors, D_{out} and D_{in}; the relationship between them is given by the constant: $k_d = D_{in}/D_{out}$.

Additional relevant variables selected by the motor designer are: the pole pair number p, the number of slots s_1, the number of turns in series per phase N_1, the number of parallel conductors a_w, the diameter of the wire d_w and the coil pitch per coil side w_c. These variables play a crucial role in determining the motor's performance and characteristics. Furthermore, certain values depend on the chosen materials for construction. These material-dependent parameters include the saturation factor of the magnetic circuit k_{sat}, the conductivity of the copper conductors σ_{cu}, the specific density of copper ρ_{cu}, the density of the PMs ρ_{PM}, the air density ρ_{air}, the dynamic viscosity of air μ_{air}, the coefficient of bearing friction k_{fb}, and the coefficient of distortion of the magnetic flux density η_d. Losses in PMs, in steel rotor disc and the tangential component of magnetic flux density in the air gap will be neglected for the sake of simplicity. This simplification allows to focus on the core aspects of motor design without delving into more complex loss calculations.

2.2.1 Motor Model

The primary objective of this analysis is to assess the steady-state performance characteristics of the motor, including output power, torque, efficiency and power factor. These evaluations are essential to meet the specific requirements set forth by the client, given the input armature current I_a (considering its projection on d axes, I_{ad}, equal to zero (Figure 2.4)).

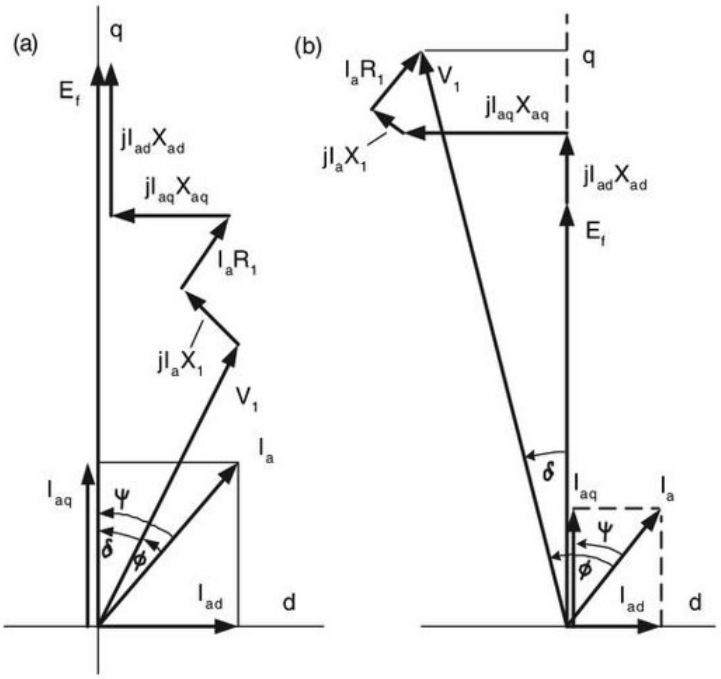

Figure 2.4: Phasor diagrams of: (a) overexcited generator, (b) under excited motor. Source: [61]

The number of coils per phase for a double layer winding is determined by the formula:

$$n_c = s_1/(m_1) \tag{2.1}$$

The number of turns per coil is calculated as:

$$N_{ct} = N_1/n_c \tag{2.2}$$

The number of coil side per pole per phase is given by:

$$q_1 = s_1/(2pm_1) \tag{2.3}$$

The air gap is half the difference between the total air gap thickness and the winding thickness: $(t - t_w)/2$. And the pole pitch measured in coil sides is determined by:

$$\tau_c = s_1/(2p) \tag{2.4}$$

The input frequency is the product of the motor velocity in revolutions per minute and the number of pole pairs:

$$f = n_s p \tag{2.5}$$

Delving into the magnetic aspects of the motor: the air gap magnetic induction produced by permanent magnets is computed as:

$$B_{mg} = \frac{B_r}{1 + [\mu_{rrec}(g + t_w/2)/h_M]k_s at} \tag{2.6}$$

The magnetic flux is given by:

$$\phi_f = \alpha_i B_{mg} \frac{\pi}{2p}[(D_{out}/2)^2 - (D_{in}/2)^2] \tag{2.7}$$

Other key factors impacting the motor's performance are:

1. The winding factor, that is the product of distribution factor and pitch factor:

$$k_{w1} = k_{d1} \cdot k_{p1} \tag{2.8}$$

   Where

$$k_{d1} = sin\frac{(\pi/2m_1)}{q_1 sin[\pi/2m_1 q_1]} \tag{2.9}$$

2. The distribution factor, defined as a polyphase winding for the first fundamental space harmonic, it is the ratio of the phasor sum-to-arithmetic sum EMFs induced in each coil. And k_{p1} is the pitch factor of the first fundamental space harmonic, evaluated as the ratio of the phasor sum-to-arithmetic sum of the EMFs per coil side:

$$k_{p1} = sin(\beta\frac{\pi}{2}) \tag{2.10}$$

   Where β is the coil pitch-to-pole pitch ratio, not dependent on the diameter:

$$\beta = \frac{w_c(r)}{\tau(r)}; \tag{2.11}$$

   $\tau(r)$ the pole pitch in function of the radius r:

$$\tau(r) = \frac{r\pi}{p} \tag{2.12}$$

   and $w_c(r)$ is the coil pitch measured in units of length at a given radius r.

3. EMF constant:

$$k_E = \pi\sqrt{2}pN_1 k_{w1}\phi_f \tag{2.13}$$

4. Torque constant:

$$k_T = k_E\frac{m_1}{2\pi} \tag{2.14}$$

5. EMF at the given speed:

$$E_f = k_E n \tag{2.15}$$

Knowing these constants and the given parameters that will be optimised later, it is possible to calculate the values of the electromagnetic torque and power:

$$T_d = k_T I_a \tag{2.16}$$

$$P_{elm} = 2\pi n T_d \tag{2.17}$$

Additional factors that need to be adjusted are the average dimensions:

- Average diameter:
$$D = (D_{out} + Din)/2 \tag{2.18}$$
- Average pole pitch:
$$\tau = \frac{\pi D}{2p} \tag{2.19}$$
- Length of conductors, that is equal to the radial length of the permanent magnets l_M
$$L_i = l_M = (D_{out} - Din)/2 \tag{2.20}$$

and the end Connection Lengths:

- Length of shorter end connection without inner bends:
$$l_{1emin} = \frac{w_c}{\tau_c}\pi\frac{D_{in}}{2p} \tag{2.21}$$
- Length of the longer end connection without outer bends:
$$l_{1emax} = l_{1emin}D_out/Din \tag{2.22}$$

The average length of the stator turn with $x \cdot m$ bends is approximately:

$$l_{1av} \approx 2L_i + l_{1emin} + l_{1emax} + 4x \tag{2.23}$$

The stator winding resistance at 75°:

$$R_1 = \frac{N_1}{a_w \sigma s_a}(2L_i k_{1R} + l_{1in} + l_{1out}) \approx k_{1R}R_{1dc} \tag{2.24}$$

Where k_{1R} is the skin-effect coefficient for the armature resistance:

$$k_{1R} = \phi(\xi_1) + [\frac{{m^2}_{sl} - 1}{3} - (\frac{m_{sl}}{2}sin(\frac{\gamma}{2}))^2]\Psi_1(\xi_1) \tag{2.25}$$

$$\phi(\xi_1) = \xi_1\frac{sinh(2\xi_1) + sin(2\xi_1)}{cosh(2\xi_1) - cos(2\xi_1)} \tag{2.26}$$

$$\Psi(\xi_1) = 2\xi_1\frac{sinh(\xi_1) - sin(\xi_1)}{cosh(\xi_1) + cos(\xi_1)} \tag{2.27}$$

$$\xi_1 = h_c\sqrt{\pi f \mu_o \sigma_1 \frac{b_{1con}}{b_{11}}} \tag{2.28}$$

where: m_{sl} is the number of conductors per slot arranged above each other in two layers; γ is the phase angle between the current of the two layers; f is the input frequency; b_1con is the width of all the conductors in a slot; b_{11} is the slot width; h_c is the height of a conductor in the slot. The maximum width of coil at the diameter D_{in} is $w_w = D_{in}\pi/s_1$; the thickness of the coil is t_w; the number of conductors per coil is $N_c = a_w N_{ct}$.

The maximum value of the coil packing factor is reached at the diameter D_{in}:

$$k_{fmax} = \frac{d_w^2 N_c}{t_w w_w} \tag{2.29}$$

The stator current density can be calculated as:

$$j_a = \frac{I_a}{2\pi d_w^2/4} \tag{2.30}$$

2.2.2 Losses

Proceeding with the investigation into motor losses and efficiency, the analysis is now conducted more in detail. The stator winding losses can be calculated as:

$$\Delta P_{1w} = m_1 I_a^2 R_1 \approx m_1 I_a^2 R1 dck_{1R} \tag{2.31}$$

Here, R_1 represents the stator winding resistance. The eddy current losses in stator round conductors, denoted as ΔP_e, are determined by various factors, including the material properties and frequency. They can be expressed as:

$$\Delta P_e = \frac{\pi^2}{4}\frac{\sigma}{\rho} f^2 d^2 m_{con}[B_{mx1}^2 + B_{mz1}^2]\eta_d^2 \tag{2.32}$$

Where m_{con} is the overall mass of the copper conductors:

$$m_{con} = \rho_{cu} m_1 a_w N_1 (\frac{\pi d_w^2}{4} 2L_i) \tag{2.33}$$

The friction losses in bearings can be estimated as:

$$\Delta P_{fr} = 0.06 k_{fb}(m_r + m_{sh})n \tag{2.34}$$

This accounts for the frictional resistance within the motor's bearings. Windage losses, expressed as ΔP_{wind}, are associated with air resistance within the motor:

$$\Delta P_{wind} = c_f \rho (2\pi n)^3 (R_{out}^5 - R_{sh}^5) \tag{2.35}$$

The coefficient of drag ($c_f = 3.87/\sqrt{(Re)}$) is determined thanks to the Reynolds number (Re), that is related with the turbulent flow. The Reynolds number is defined as:

$$Re = \rho R_{out} v/\mu = 2\pi n \rho R_{out}^2/\mu \tag{2.36}$$

Where v represents the linear velocity at the outer radius R_{out}. It's important to note that ΔP_{vent} has been assumed equal to 0, indicating negligible ventilation losses.

The total rotational losses (ΔP_{rot}) encompass friction losses in bearings, windage losses, and ventilation losses (if present). It can be expressed as:

$$\Delta P_{rot} = \Delta P_{fr} + \Delta P_{wind} + \Delta P_{vent} \tag{2.37}$$

The motor's output power (P_{out}) is determined as the electromagnetic power (P_{elm}) minus the rotational losses (ΔP_{rot}):

$$P_{out} = P_{elm} - \Delta P_{rot} \tag{2.38}$$

The shaft torque (T_{sh}) can be calculated by dividing the output power by the motor's synchronous speed:

$$T_{sh} = \frac{P_{out}}{2\pi n_s/60} \tag{2.39}$$

The input power (P_{in}) is the sum of electromagnetic power (P_{elm}), stator winding losses (ΔP_{1w}), and eddy current losses (ΔP_e):

$$P_{in} = P_{elm} + \Delta P_{1w} + \Delta P_e \tag{2.40}$$

The motor's efficiency (η) is defined as the ratio of output power to input power:

$$\eta = \frac{P_{out}}{P_{in}} \tag{2.41}$$

The leakage reactance can be approximately calculated taking into account the radial part of the conductors, end connection and differential leakage fluxes, that can be represented as follows:

$$\lambda_{1e} \approx 0.3 q_1 \tag{2.42}$$

$$\lambda_{1s} \approx \lambda_{1e} \tag{2.43}$$

$$\lambda_{1d} = \frac{m_1 q_1 \tau k_{w1}^2}{\pi^2 g' k_{sat}} \tau_{d1} \tag{2.44}$$

Here, k_{sat} represents the saturation factor of the magnetic circuit, and τ_{d1} is the differential leakage factor, calculated as:

$$\tau_{d1} = \frac{1}{k_{w1}^2} \sum_{\nu>1} (\frac{k_{w1\nu}}{\nu})^2 \tag{2.45}$$

Remembering that, in these equations, t_w represents the stator winding axial thickness, h_M is the axial height of the PM and μ_{rrec} is the relative recoil permeability of the PM, g' is the equivalent air gap in the d axis:

$$g' = 2[(g + 0.5 t_w) + \frac{h_M}{\mu_{rrec}}] \tag{2.46}$$

While the equivalent air-gap in the q axis is:

$$g'_q = 2[(g + 0.5 t_w) + h_M] \tag{2.47}$$

The armature leakage reactance is the sum of the slot leakage reactance X_{1s}, the end connection leakage reactance X_{1e} and the differential leakage reactance X_{1d} and it can be calculated as:

$$X_1 = X_{1s} + X_{1e} + X_{1d} =$$

$$= 4\pi f \mu_o \frac{L_i N_1^2}{p q_1} (\lambda_{1s} k_{1X} + \frac{l_{1in}}{L_i} \lambda_{1ein} + \frac{l_{1out}}{L_i} \lambda_{1out} + \lambda_{1d}) \tag{2.48}$$

More in detail, λ_{1s} represents the coefficient of the slot leakage performance (slot-specific permeance), while $\lambda 1 ein$ is the coefficient of the leakage permeance of the inner end connection and $\lambda 1 eout$ is the coefficient of the leakage permeance of the outer end connection; λ_{1d} is the coefficient of the differential leakage; l_{1in} represents the length of the stator winding inner end connection, and l_{1out} is the length of the stator winding outer end connection.

$$l_{1e} = 0.5(l_{1emin} + l_{1emax}) \tag{2.49}$$

To summarise, these calculations provide a comprehensive understanding of the motor's losses, efficiency, and important parameters that impact its performance.

2.2.3 Synchronous reactances computations and supplying conditions

The armature reaction reactances can be determined as follows:

- On the d-axis:

$$X_{ad} = 2m_1\mu_0 f(\frac{N_1 k_{w1}}{p})^2 \frac{(R_{out}^2 - R_{in}^2)}{g'} k_{fd} \tag{2.50}$$

- On the q-axis:

$$X_{aq} = 2m_1\mu_0 f(\frac{N_1 k_{w1}}{p})^2 \frac{(R_{out}^2 - R_{in}^2)}{g'_q} k_{fq} \tag{2.51}$$

Here, $k_{fd} = k_{fq} = 1$ are both equal to 1 for a surface configuration of permanent magnets.

The synchronous reactance of a synchronous machine, also known as a sine-wave machine, is defined as the sum of the armature reaction (mutual) reactances X_{ad} and X_{aq}, combined with the stator (armature) leakage reactance X_1:

$$X_{sd} = X_{ad} + X_1 \tag{2.52}$$

$$X_{sq} = X_{aq} + X_1 \tag{2.53}$$

Therefore, the input phase voltage is given by:

$$V_1 = \sqrt{(E_f + I_a R_1)^2 + (I_a X_{sq})^2} \tag{2.54}$$

The line-to-line voltage is calculated as:

$$V_{1L-L} = \sqrt{3} V_1 \tag{2.55}$$

Finally, the power factor $cos\phi$ is defined as:

$$cos\phi = \frac{E_f + I_a R_1}{V_1} \tag{2.56}$$

2.2.4 Rotor moment of inertia

To determine the rotor's moment of inertia, it is first needed to calculate the active surface area of permanent magnets (PMs) on one side:

$$S_{PM} = \alpha_i \frac{\pi}{4}(D_{out}^2 - D_{in}^2) \tag{2.57}$$

The mass of all PMs is required as well:

$$m_{PM} = 2S_{PM}\rho_{PM}h_{PM} \tag{2.58}$$

Mass of backing steel discs is obtained as:

$$m_{Fe} = m_r - m_{PM} \tag{2.59}$$

The PMs moment of inertia is calculated as:

$$J_{PM} = m_{PM}\frac{D_{out}^2 + D_{in}^2}{8} \tag{2.60}$$

Similarly, the moment of inertia of the backing steel disc is computed as:

$$J_{Fe} = m_{Fe}\frac{D_{out}^2 + D_{in}^2}{8} \tag{2.61}$$

Therefore, the resultant moment of inertia of the rotor is given by:

$$J_r = J_{PM} + J_{Fe} \tag{2.62}$$

2.2.5 Mechanical and electromagnetic time constants

Assuming the d-axis current, I_{ad}, equal to 0, the angle between the q axis and the stator current, ψ is equal to 0 too; knowing the value of the power factor from equation (2.56), the load angle is:

$$\delta = \phi - \psi \tag{2.63}$$

Assuming that the load angle at the starting point is equal to the nominal operating load angle, the stator current equations can be derived as follows:
On the d-axis:

$$I_{ashd} = \frac{V_1(X_{sq}cos\delta - R_1 sin\delta) - E_f X_{sq}}{X_{sd}X_{sq} + R_1^2} \tag{2.64}$$

On the q-axis:

$$I_{ashq} = \frac{V_1(R_1 cos\delta + X_{sd} sin\delta) - E_f R_1}{X_{sd}X_{sq} + R_1^2} \tag{2.65}$$

The resulting stator current magnitude is calculated as:

$$I_{ash} = \sqrt{I_{ashd}^2 + I_{ashq}^2} \tag{2.66}$$

The electromagnetic starting torque can be determined as:

$$T_{dst} = K_T I_{ashq} \tag{2.67}$$

The no load speed, following the assumption of linear torque-speed curve:

$$n_0 = \frac{rpm}{1 - T_d/T_{dst}} \tag{2.68}$$

To evaluate the mechanical time constant in seconds, the result of the following equation in revolutions per minute (rpm) must be converted to revolutions per second (rev/s):

$$T_{mech} = J_r \frac{2\pi n_0}{T_{dst}} \tag{2.69}$$

Additionally, the synchronous inductances on the d and q axes are given by:

$$L_{sd} = \frac{X_{sd}}{2\pi f} \tag{2.70}$$

$$L_{sq} = \frac{X_{sq}}{2\pi f} \tag{2.71}$$

Finally, the electromagnetic time constant of the stator winding is determined as:

$$T_{elm} = \frac{L_{sd}}{R_1} \tag{2.72}$$

2.2.6 Axial attractive force between backing steel discs of the twin rotor

To determine the axial magnetic attractive force between the two backing steel discs, the virtual box method has been employed, which is expressed as:

$$F_z = -\frac{dW}{dz} \tag{2.73}$$

Where, W represents the total magnetic energy stored in the machine, and dz is the infinitesimal variation of the air gap length. Analytically, it is possible to simplify this further using the following formula:

$$F_z \approx \frac{1}{2}\frac{B_{mg}^2}{\mu_0} S_{PM} \tag{2.74}$$

This allows us to calculate the magnetic pressure as:

$$p_z = \frac{F_z}{S_{PM}} \tag{2.75}$$

Furthermore, the backing steel disc thickness, needed to build the prototype, is determined as:

$$d_{Fe} = \frac{m_{Fe}}{2\rho_{Fe}\pi(D_{out}^2 - D_{in}^2)/4} \tag{2.76}$$

2.3 Commercial Examples of AFPM Machines

To highlight the importance of this new type of motor configuration, particularly in automotive applications, it is possible to focus on a couple of commercial examples of axial flux permanent magnets machines and an example of the big potential of the integration of axial and radial fluxes.

2.3.1 YASA 750R

Mercedes-Benz's recent acquisition of the British axial flux motor designer, YASA, has brought to the forefront a breakthrough in high-performance motor technology, exemplified in their newly futuristic Vision One-Eleven electric vehicle concept. YASA's innovative motor technology, previously seen in low-volume hybrid vehicles such as McLarens and Ferraris, is poised to make a significant impact, driven by its remarkable attributes.

As has been explained before, in terms of energy conversion from electricity into rotational torque, axial flux motors exhibit efficiency levels comparable to standard radial flux machines. However, the distinguishing factor lies in the compactness and reduced weight of axial flux motors relative to their power output. Dr. Tim Woolmer, the visionary behind YASA, elaborates on the transformative effects of this weight and size advantage in electric vehicle (EV) efficiency. Lightweight EVs inherently achieve higher efficiency, and when weight reduction is achieved across the vehicle, it translates into extended driving ranges. YASA's motors are notably one-sixth the size and half the weight of many equivalent radial flux machines. Consequently, the demand for extensive structural support for motor installation diminishes, enabling the use of smaller batteries for a given range. This, in turn, reduces the overall structural requirements for battery housing, and even auxiliary systems like cooling can be downsized, decreasing mass and size.

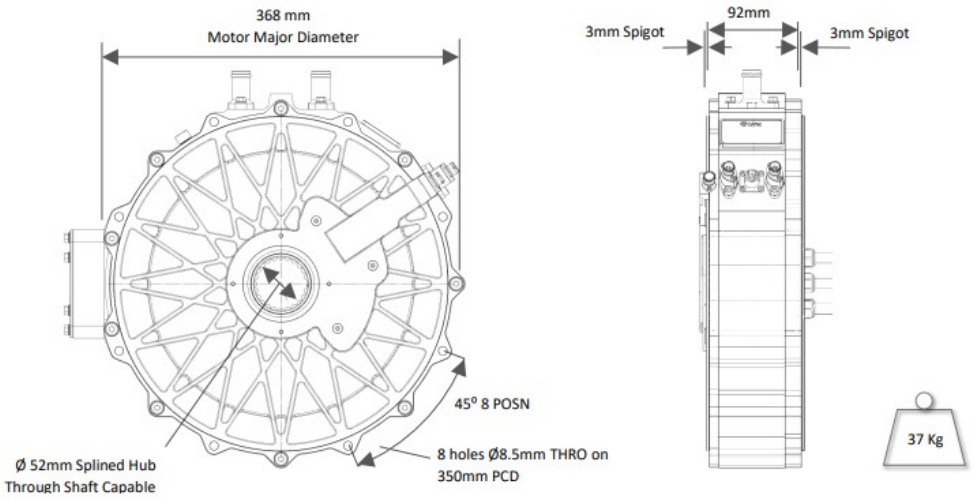

Figure 2.5: YASA 750R. Source: [62]

It is worth noting that while axial flux motors offer remarkable advantages, they have faced considerable technical challenges in achieving manufacturability and efficiency at a large scale. Dr. Woolmer and his team at YASA have devoted substantial efforts to address these challenges since 2005. Notably, radial flux rotors, found in conventional motors, are fabricated from simple laminations that lend themselves to straightforward manufacturing. This ease of production is not applicable to axial flux machines, demanding substantial engineering prowess to attain cost parity between the two technologies.

Focusing more on one of the latest YASA's product: YASA 750R; it utilises YASA's distinctive Yokeless and Segmented Armature configuration, optimising material usage and achieving superior torque and power densities compared to similar motors or generators. The YASA 750R has been designed for lower speeds but it delivers exceptional torque, standing out with its remarkable torque and power capabilities. It boasts a peak torque of 790Nm, peak power of 200kW, and a speed range spanning from 0 to 3250rpm, all while maintaining a compact axial length of just 98mm. The YASA 750 R represents a high-torque motor evolved from the reliable YASA 750, featuring a redesigned mechanical structure that facilitates installation and integration. This redesign includes enhanced mechanical durability and stiffness.

2.3.2 Koenigsegg Quark e-Motor™

Koenigsegg has recently introduced the innovative Quark e-motor, a groundbreaking development that rethinks fundamental aspects of motor design, including magnetism, materials, cooling, and packaging.

The name "Quark" is inspired by the elementary particle of the same name, which interacts with all four fundamental forces. This unique e-motor design, called "Raxial Flux," combines the advantages of both axial and radial flux solutions, resulting in the industry's best torque-to-power-to-weight ratio. The Quark finds its application in the high-performance Koenigsegg cars, enhancing low-speed performance for brutal acceleration while the internal combustion engine (ICE) focuses on high-speed operation. Constructed from high-strength 300M steel and featuring direct cooling and Koenigsegg's Aircore™ hollow carbon fibre rotor technology, the Quark sets new benchmarks for compact and torque-rich engineering.

With its exceptional efficiency and versatility, this motor is poised to revolutionise various industries, from marine and aviation to vertical takeoff and landing (VTOL) applications. Moreover, it is an integral component of Koenigsegg's comprehensive in-house high-voltage architecture, encompassing e-motors, batteries, and controllers.

Figure 2.6: Koenigsegg Quark e-Motor™. Source: [63]

This design triumphantly overcomes the challenges posed by the requirements of the famous Koenigsegg Gemera supercar, while simultaneously surpassing weight and size goals. The Quark, in its first production version, weighs a mere 30 kg while delivering up to 600 Nm of torque and 250 kW of power. Without the additional driveline functions for the Gemera, the Quark's weight can drop below 28.5 kg.

Chapter 3

Radial Flux PMSM and Control of PM Synchronous Machines

The rapid evolution of electric vehicles (EVs) has led to an increased demand for high-performance electric motors. Radial Flux Motors, such as Permanent Magnet Synchronous Motors (PMSMs), Induction Motors, and Switched Reluctance Motors (SRMs), have emerged as key contenders in this domain. Each of these motor types exhibits unique advantages and disadvantages, making them suitable for specific applications within the electric vehicle sector. In this section, a comparative analysis of these motor types will be done, highlighting their respective strengths and weaknesses, especially with a focus on the practical example of the Nissan LEAF motor.

3.1 Comparative Analysis of Radial Flux Motors:

- **Permanent Magnet Synchronous Motor (PMSM):**
  Advantages:
  High Power Density: PMSMs are renowned for their exceptional power density, making them ideal for applications where compactness and high power output are crucial.
  High Efficiency: PMSMs deliver impressive efficiency levels, ensuring minimal energy losses during operation.

  Disadvantages:
  Limited Speed Range: PMSMs are characterised by a limited speed range, which can be a drawback in certain high-speed applications.
  High Cost: The inclusion of permanent magnets in PMSMs contributes to their relatively high production costs.
  High Stator Core Losses at High Speed: At high speeds, PMSMs may experience increased stator core losses, impacting overall efficiency. (In the event of malfunctions, there would always be an induced electromotive force (EMF) applied to the stator in the presence of shaft rotation, which could potentially support them.)

- **Induction Motor:**
  Advantages:
  High Speed Range: Induction motors offer a broad speed range, making them versatile for various applications.

High Reliability: They are known for their robustness and reliability, ensuring consistent performance.
Low Cost: Induction motors are cost-effective and widely available in the market. Additionally, they are rugged in Hostile Environments: Their ability to withstand adverse conditions makes them suitable for operations in harsh environments.

Disadvantages:
Low Efficiency: Induction motors tend to have lower efficiency compared to PMSMs, leading to higher energy consumption.
Thermal Problems at High Speed: Operating at high speeds can lead to thermal issues that affect performance and longevity.

- **Switched Reluctance Motor (SRM):**
  Advantages:
  Desirable Torque-Speed Characteristic: SRMs exhibit a favourable torque-speed profile, which can be advantageous for certain applications.
  High Reliability: They are reliable and durable in demanding conditions.
  Low Cost: SRMs are generally cost-effective to manufacture.
  Rigidity in Hostile Environments: Similar to induction motors, SRMs are suitable to work in harsh environments.

  Disadvantages:
  High Torque Ripple and Noise: SRMs may suffer from torque ripple and noise issues during operation.
  Lower Power Density: They typically have a lower power density compared to PMSMs.
  Low Efficiency: SRMs may not achieve the same level of efficiency as PMSMs.

To summarise, how to choose the ideal motor for electric vehicle?
When assessing the suitability of these motors for electric vehicle propulsion, the ideal characteristics include high efficiency, high power density, a broad speed range, reliability, and cost-effectiveness. Among the radial flux motors, PMSMs stand out as the most favourable choice due to their exceptional efficiency and power density. This makes them ideal candidates for driving modern electric vehicles, where maximising energy efficiency and power output is of greatest importance.

A decisive role is played by the analytical modelling and its optimisation; to design electric machines customised for traction applications, designers require two essential tools: accurate analytical models and efficient optimisation algorithms. These tools empower designers to calculate the intricate relationships between the electromagnetic aspects of the machine while exploring various input combinations to achieve the best compromise between material properties, machine dimensions, and production costs.

3.2 Permanent Magnet Synchronous Machines (PMSM)

The choice of radial flux motors for electric vehicle propulsion is a critical decision influenced by various advantages and disadvantages. PMSMs, with their high efficiency and power density, are poised to play a pivotal role in the future of electric transportation. The integration of accurate analytical models and efficient optimisation techniques is imperative to harness the full potential of these motors and accelerate the development of next-generation electric vehicles.
In the realm of electrical engineering, the use of permanent magnets (PMs) in constructing electrical machines has emerged as a crucial innovation, yielding a host of benefits that revolutionise

machine performance and efficiency. This subsection delves into the endless list of advantages conferred by PMs, tracing their historical development, and exploring their contemporary applications in the context of power electronics and control technology.

3.2.1 The Historical Evolution

The origins of **PM excitation** systems can be traced back to the 19th century when pioneering individuals such as J. Henry (1831), H. Pixii (1832), W. Ritchie (1833), F. Watkins (1835), T. Davenport (1837), and M.H. Jacobi (1839) first employed them in electrical machines. These early experiments took advantage of the inherent properties of permanent magnets to create excitation systems. However, the use of inferior quality hard magnetic materials like steel and tungsten steel quickly overshadowed PMs in favour of electromagnetic excitation systems.

The revival of PM excitation systems occurred in 1932 with the advent of Alnico magnets. Nevertheless, their application remained confined primarily to small and fractional commutator machines. Currently, most PM direct current (D.C.) commutator motors featuring slotted rotors utilise ferrite magnets.

Throughout the 20th century, **cage induction motors** stood as the model of electric motors. Their widespread adoption can be attributed to their simplicity of construction, ease of maintenance, absence of commutators or slip rings, affordability, and reasonable reliability. These motors typically span a rated output power range from 70 W to 500 kW, with a majority operating at 1500 rpm. However, they exhibit certain drawbacks such as a smaller air gap, susceptibility to rotor bar cracking due to hot spots during plugging and reversal, and relatively lower efficiency and power factor compared to synchronous motors.

In recent times, the ascendancy of **PM brushless motors** has emerged as a compelling alternative to traditional induction motors. Notably, rare earth PMs have been in the spotlight, not only enhancing steady-state performance but also elevating power density, dynamic performance, and overall quality. Furthermore, the decreasing cost of rare earth magnets has made these motors increasingly accessible.

Crucially, advancements in semiconductor drives have simplified and reduced the cost of controlling brushless motors. This evolution enables these motors to operate efficiently across a wide range of speeds, all while maintaining high levels of performance.

3.2.2 Characteristics of the Machine

When delving into the domain of synchronous machines, the focus inevitably gravitates towards its mathematical model.

First, it is mandatory to see through its mechanical and electrical structure: it consists of a cylindrical stator with a symmetrical three-phase winding arrangement, generating a sinusoidal distribution of magnetomotive force in the air gap. The rotor is equipped with permanent magnets and lacks damping cages. Two primary rotor configurations are commonly employed: one with permanent magnets adhered to the surface (Figure 3.1a) and another with embedded magnets (Figure 3.1b). It is assumed that both the stator and rotor are constructed from fully laminated material with infinite permeability. In order to simplify the model, considerations on saturation, iron hysteresis, and machine anisotropies resulting from slots are neglected.

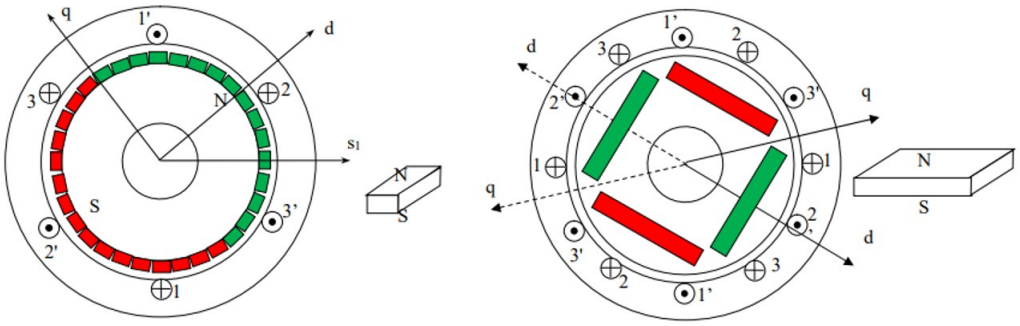

Figure 3.1: Example of PMSM's rotor types: (a) with permanent magnets glued on rotor surface, 2 poles; (b) rotor with interior permanent magnets, 4 poles. Source: [64]

The electrical dynamic equation in terms of phase variables can be written as:

$$V_a = R_s I_a + \frac{d\Psi_a}{dt} \tag{3.1}$$

$$V_b = R_s I_b + \frac{d\Psi_b}{dt} \tag{3.2}$$

$$V_c = R_s I_c + \frac{d\Psi_c}{dt} \tag{3.3}$$

Where V_a, V_b and V_c are the phase voltages, I_a, I_b and I_c are the phase current and R_s is the phase resistance. The phase flux linkage components that are provided by permanent magnets are:

$$\Psi_a = L_{aa} I_a + L_{ab} I_b + L_{ac} I_c + \Psi_{ma} \tag{3.4}$$

$$\Psi_b = L_{ab} I_a + L_{bb} I_b + L_{bc} I_c + \Psi_{mb} \tag{3.5}$$

$$\Psi_c = L_{ac} I_a + L_{bc} I_b + L_{cc} I_c + \Psi_{mc} \tag{3.6}$$

In these equations, inductances are functions of the angle *theta*. Since stator self-inductances ($L_a a$, $L_b b$, $L_c c$) are maximum when the rotor q-axis is aligned with the phase axis, while mutual inductances ($L_a b$, $L_a c$, $L_b c$) are maximum when the rotor q-axis is in the midway between two phases. In addition, the effect of saliency appeared in stator self and mutual inductances are indicated by the term 2θ. Whereas, flux linkage at the stator windings due to permanent magnet are:

$$\Psi_{ma} = \Psi_m \cos(\theta) \tag{3.7}$$

$$\Psi_{mb} = \Psi_m \cos(\theta - \frac{2\pi}{3}) \tag{3.8}$$

$$\Psi_{mc} = \Psi_m \cos(\theta + \frac{2\pi}{3}) \tag{3.9}$$

The input power, $P_i n$, can be calculated as:

$$P_{in} = Re(\overline{V_a}\underline{I_a} + \overline{V_b}\underline{I_b} + \overline{V_c}\underline{I_c}) \tag{3.10}$$

To go on with the analysis, it is suggested to project the $a-b-c$ frame to $d-q$ frame through the Park's transform:

$$\begin{bmatrix} S_q \\ S_d \\ S_0 \end{bmatrix} = \frac{2}{3} \begin{bmatrix} \cos\theta & \cos\theta - 2\pi/3 & \cos\theta + 2\pi/3 \\ \cos\theta & \sin\theta - 2\pi/3 & \sin\theta + 2\pi/3 \\ 1/2 & 1/2 & 1/2 \end{bmatrix} \begin{bmatrix} S_a \\ S_b \\ S_c \end{bmatrix} \tag{3.11}$$

The stator voltage equations in $d-q$ frame then becomes:

$$v_d = Ri_d + \frac{d\Psi_d}{dt} - \omega_s \Psi_q \tag{3.12}$$

$$v_q = Ri_q + \frac{d\Psi_q}{dt} + \omega_s \Psi_d \tag{3.13}$$

where:

$$\Psi_q = \Psi_{aq} = L_q i_q \tag{3.14}$$

$$\Psi_d = \Psi_{ad} + \Psi_m = L_d i_d + \Psi_m \tag{3.15}$$

Ψ_m is the permanent magnet flux linkage. In figure 3.2 the dynamic equivalent circuit for d and q frame is represented.

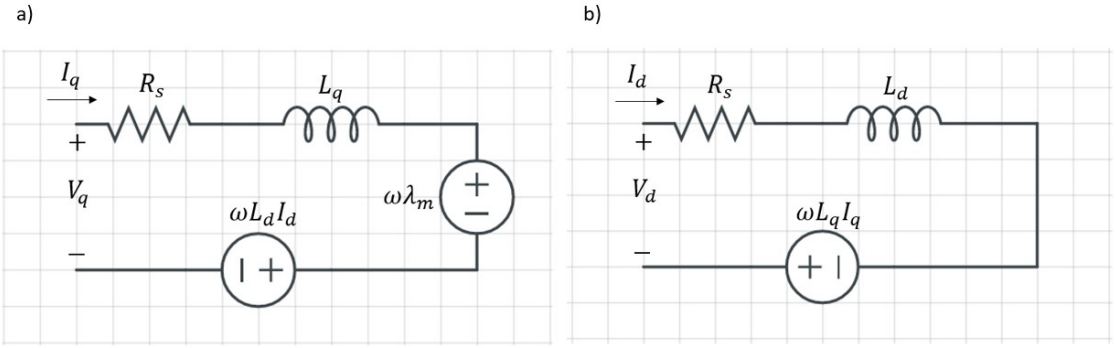

Figure 3.2: PMSM equivalent circuit

According to it, it is possible to draw the following phasor diagram:

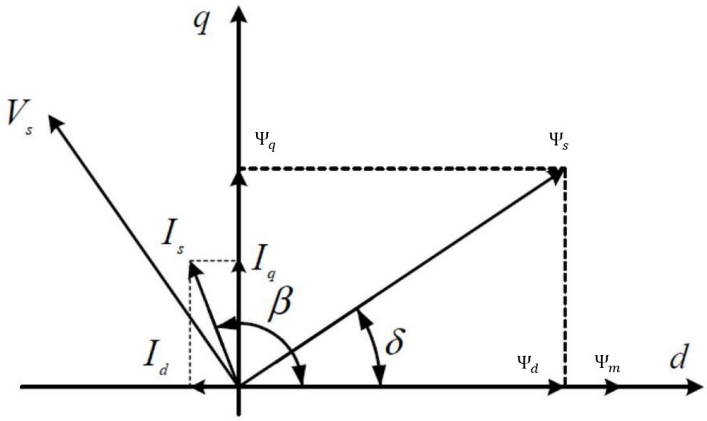

Figure 3.3: Stator flux linkage in $d-q$ reference frame

The input power, via Park transform:

$$P_{in} = \begin{bmatrix} v_a v_b v_c \end{bmatrix} \begin{bmatrix} i_a \\ i_b \\ i_c \end{bmatrix} = \frac{2}{3} \begin{bmatrix} v_q v_b \end{bmatrix} \begin{bmatrix} i_q \\ i_b \end{bmatrix} = \frac{2}{3}(v_q i_q + v_d i_d) \tag{3.16}$$

Neglecting the zero sequence quantities, the output power can be obtained by replacing v_q and v_d with the associated back EMF $\omega_s \Psi_d$ and $-\omega_s \Psi_q$:

$$P_o = \frac{3}{2}(-\omega_s \Psi_q i_d + \omega_s \Psi_d i_q) \tag{3.17}$$

The electromagnetic torque, that, from definition, is the ratio between power and mechanical speed, is then calculated with:

$$T_e = \frac{2}{3}\frac{p}{2}[\Psi_m i_q + (L_d - L_q) i_q i_d] \tag{3.18}$$

It is visible from this equation that the torque is composed by two elements: the first one represent the magnet excitation torque, or synchronous torque, occurring between i_q and the permanent magnet; the second one is the reluctance torque, generated by the difference between d and q reluctance axes. Nevertheless, the torque equation suggests that the interior PMSMs can be interpreted as hybrid combination of conventional synchronous reluctance motors and exterior permanent magnet motors.

3.2.3 Control and Operative Regions

Going more in detail in the control field: the vector control of the synchronous machine relies on an adequate selection of the d and q reference axes used by the controller of the power supply, ensuring that one component of the stator current exclusively affects the flux, while the other influences the torque. This approach allows the synchronous motor to be regulated similarly to a DC machine, where separate control is applied to the excitation current (flux) and the armature current (torque).
From the torque equation:

$$T_e = \frac{2}{3}\frac{p}{2}\lfloor \Psi_m i_q + (L_d - L_q) i_q i_d \rfloor \tag{3.19}$$

While analysing the torque expression, it is evident that rotor anisotropy, represented by the difference $(L_d - L_q)$, results in an anisotropic torque. In the following discussion, unless otherwise specified, only the case of an isotropic synchronous machine will be considered, where $L_d = L_q = L_s$, unless otherwise specified. In this isotropic case:

$$T_e = n_p \Psi_{pm} i_{sq} \tag{3.20}$$

From the above expression, it is evident that only the quadrature component of the stator current is effective for torque production purposes, while the direct component contributes nothing. To minimise the magnitude of the current phasor (and consequently minimise Joule heating losses), it is advisable to control the input converter such that, at all times:

$$i_{sd} = 0 \tag{3.21}$$

From a torque control perspective, the quadrature component of the stator current assumes the same role of the armature current for DC motors. However, under conditions of i_{sd} being zero, it is not possible to manipulate the excitation (flux weakening) since the latter is provided by permanent magnets.

It is important to note that, in the present context, i_{sd} and i_{sq} are not currents flowing in physically distinct windings but rather the components of a unified three-phase current system projected on d and q axes, which rotate synchronously with the rotor. The transition between the two systems is achieved through the spatial phasor transformation formulas. In the case of steady-state operation with the machine being supplied by a symmetrical three-phase voltage system at angular frequency ω, the mechanical speed $\dot{\theta}_m$ (also denoted as ω_m) coincides with the angular frequency ω. In the reference frame fixed to the rotor, the voltage phasor remains stationary and constant. Consequently, all electrical quantities remain constant, and it is assumed that (i_{sd} has been set to zero, and all derivatives are zero):

$$\dot{\theta}_m = \omega_m = \omega \tag{3.22}$$

$$v_{sq} = R_s i_{sq} + E \tag{3.23}$$

$$v_{sd} = -\omega_m L_s i_{sd} \tag{3.24}$$

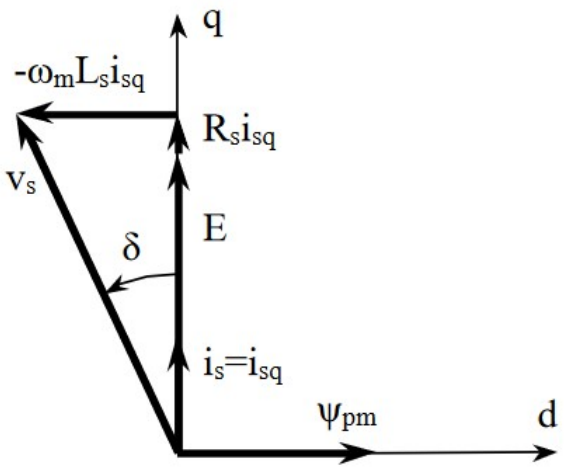

Figure 3.4: Phasor diagram of the brushless motor at steady state for $\omega < \omega_b$. Source: [64]

In situations where resistive voltage drop is negligible compared to E, it is observed that the phase angle δ remains constant as the angular frequency (mechanical speed) varies (both sides of the right triangle are proportional to mechanical speed). Additionally, the magnitude of the voltage vector grows proportionally with the angular frequency (mechanical speed). The speed at which the voltage vector reaches the maximum value provided by the power supply (within the limits of stator winding insulation) is referred to as the base speed ω_b. In the context of three-phase inverter supply, this limit can be depicted as a circle with a radius slightly smaller than the radius of the inscribed circle within the hexagon representing the inverter's operational range (to maintain a voltage margin for dynamic current control).

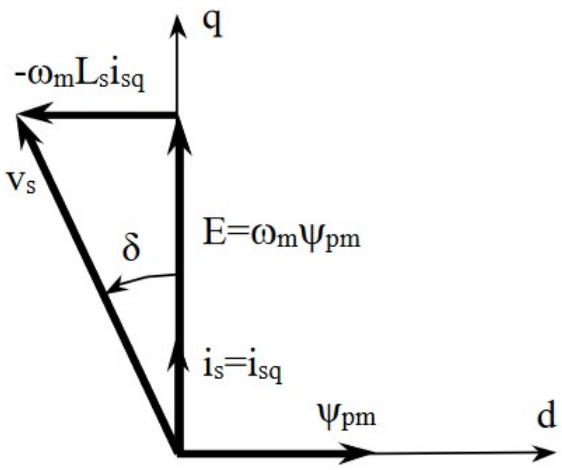

Figure 3.5: Phasor diagram of the brushless motor at steady state for $\omega < \omega_b$, neglecting the resistive voltage drop. Source: [64]

If then the motor is supposed to be powered to keep the direct current negative, the equations become the following:

$$v_{sd} = R_s i_{sd} - \omega_m L_s i_{sq} \tag{3.25}$$

$$v_{sq} = R_s i_{sq} + \omega_m L_s i_{sd} + E \tag{3.26}$$

From which, neglecting the resistive voltage drop, it is possible to reach this diagram:

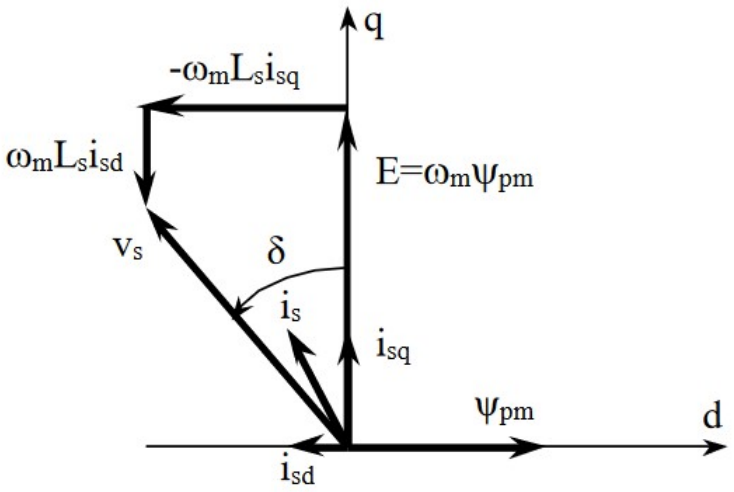

Figure 3.6: Phasor diagram of the brushless motor in the presence of negative current $i_s d$. Source: [64]

In the construction, it becomes evident that, for a given I_{sq} component (and therefore torque), the addition of a negative I_{sd} component leads to a reduction in the power supply voltage vector, but also to an increase in the current vector. The necessity to maintain the stator current within a predetermined maximum value, which is imposed by thermal constraints of the hardware, thus requires a reduction in I_{sq} (and hence torque) with an increase in I_{sd}. These observations suggest the following operational approach:

- For speeds below the base speed (ω_b), it is advantageous to keep I_{sd} at 0 and limit the I_{sq} component to the maximum value allowed by thermal constraints (I_max). This allows for operation in a constant torque region at the maximum possible torque. As the supply frequency (and hence the speed), increases, the back electromotive force (E) also increases, necessitating a higher supply voltage from the power supply. At the base speed, the supply voltage is equal to the maximum voltage provided by the power supply, with a certain margin required for current regulation.

- For speeds above the nominal speed, it is no longer possible to maintain $I_{sq} = I_{max}$ because the further increase in E would require a supply voltage higher than what the power supply can provide, which is already at its maximum. In this region, I_{sq} must be reduced to make room for a negative I_{sd} component so that the following condition always holds:

$$i_s = \sqrt{i_{sd}^2 + i_{sq}^2} \leq i_{max} \tag{3.27}$$

By doing so, V_s can be maintained at V_{max}, and I_s can be kept below I_{max}, but with a lower I_{sq} (and therefore torque) compared to the case where $I_{sd} = 0$. Indeed, in the limiting case where $E = v_{max}$, if $i_{sd} = 0$, then it should also be the case that $i_{sq} = 0$. This would lead to a velocity of:

$$\omega' = \frac{E'}{\Psi_{pm}} = \frac{v_{max}}{\Psi_{pm}} \tag{3.28}$$

with zero currents and torque (idle speed, of little significance). However, by imposing $i_{sd} < 0$, we can achieve a situation where the motor is still capable of generating torque. In this manner, a kind of demagnetisation occurs (the i_{sd} component opposes the flux of the permanent magnets Ψ_{pm}). The torque decreases as the value of i_{sq} must decrease to keep the magnitude of the stator current within limits:

$$i_{sq} = \sqrt{i_{max}^2 - i_{sd}^2} \tag{3.29}$$

The transition point is defined by the value of the mechanical velocity $\omega*$. For $\omega_m > \omega*$, the voltage $\omega_m L_s i_{sd}$ becomes equal to E, regardless of the mechanical velocity. It can be deduced that i_{sq} equals $v_{max}/(\omega_m L_s)$, and thus, the torque becomes inversely proportional to the mechanical velocity. From this point onwards, the magnitude of the stator current cannot be maintained at its maximum value but must decrease:

$$i_s = \sqrt{i_{sd}^2 + i_{sq}^2} = \sqrt{\left(\frac{\Psi_{pm}}{L_s}\right)^2 + \left(\frac{v_{max}}{\omega_m L_s}\right)^2} < i_{max} \tag{3.30}$$

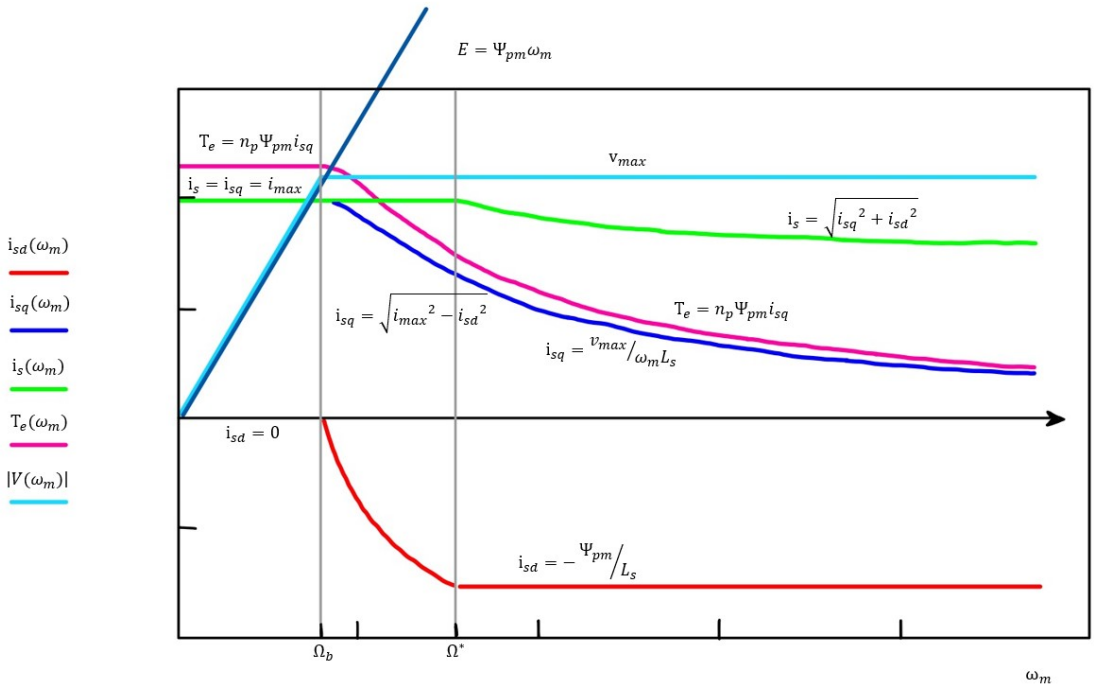

Figure 3.7: Operative regions. Source: [64]

3.3 The case of Nissan LEAF's Motor

The motor that will be analysed more in detail in chapters 5 and 6 is the practical case of the traction motor mounted on the Nissan LEAF Generation 1; this is a very interesting case since Nissan LEAF has been one of the first examples of electrical cars available on the market.

Nissan's LEAF has illuminated the path towards sustainable mobility over the last decade. Initially launched in Japan, Europe, and the United States, the LEAF has since permeated 59 global markets, with over half a million units sold worldwide. Despite its compact stature, the Nissan LEAF has left an indelible mark on the EV landscape, laying the cornerstone for contemporary electric mobility. By re-imagining the essence of an automobile, the LEAF has transcended conventional mobility paradigms and has begun to explore novel interfaces between electric vehicles and everyday life, facilitating a more sustainable future.

Remarkable among the LEAF's technological contributions is its pioneering battery technology, which extends its utility beyond mere transportation. By enabling power sharing between homes and vehicles through the innovative Vehicle-to-Home (V2H) system, LEAF owners gained the capability to store energy within their EV batteries for later use in their residences. This innovation not only bolstered energy self-sufficiency but also endowed the LEAF with the potential to serve as a mobile emergency power source during natural disasters.

- **2010:**
  Nissan's inaugural LEAF embodied a vision to combat urbanisation and industrial development while delivering exhilarating driving experiences without carbon emissions. This first-generation LEAF boasted powerful acceleration, smooth handling, and unique remote management features via smartphones. Its 24-kilowatt-hour lithium-ion battery endowed it with a 200-kilometre range. Moreover, Nissan actively collaborated with governmental bodies and utilities to expand charging infrastructure, heralding the rise of electric vehicle adoption.

- **2012:**
  Two years post-launch, Nissan unveiled the V2H system, allowing LEAF owners to store and share energy between their EVs and homes. The LEAF's adaptability as an emergency power source was showcased during electricity disruptions, such as the smart grid project on Maui.
  Further advancements in the electric powertrain improved the LEAF's power output and extended its range to 228 kilometres. These improvements did not entail an increase in component size; instead, they reduced volume and mass while enabling added features like heated seats and steering wheels.

- **2015:**
  Battery technology evolved as the LEAF adopted a 30-kilowatt-hour battery and a 280-kilometre range, all without compromising cabin space or charging time. This update also introduced safety technologies, including Intelligent Emergency Braking.

- **2017:**
  The second-generation LEAF introduced groundbreaking technologies such as the e-Pedal for one-pedal driving and ProPILOT advanced driver assistance. The electric powertrain was upgraded, resulting in a 400-kilometre range while maintaining the battery's compact size and boosting energy density by 67%. In 2017, the LEAF also spearheaded Nissan's car-sharing initiative in Japan.

- **2018:**
  The LEAF became even more versatile with innovations from the Nissan Energy program, allowing the car to share energy with homes and businesses. Initiatives like the Nissan Energy Home and battery reuse and recycling underscored Nissan's commitment to sustainability.

- **2019:**
  The LEAF e+ introduced a more powerful motor and extended range, thanks to its 62-kilowatt-hour battery. With a 458-kilometre range, it continued to deliver the instant torque that characterises the LEAF's dynamic driving experience.

The journey of the Nissan LEAF is a testament to its pivotal role in the transition from internal combustion engines to zero-emission electric vehicles. Initially met with scepticism, the LEAF has proven instrumental in dispelling myths and misconceptions surrounding electric cars. Its remarkable evolution demonstrates the rapid embrace of electric mobility by consumers and signifies a profound shift in the automotive industry. Ultimately, the Nissan LEAF has not only redefined how vehicles are conceived and constructed but has also reshaped the very fabric of our lives.

Chapter 4

Thermal Sizing Methods

Thermal sizing methods are essential for determining the optimal heat management solutions in electrical machines. These methods enable engineers to assess and optimise the thermal performance of machines, ensuring safe and efficient operation under various conditions. In the following paragraphs general and more specific rules for both Axial and Radial flux machines, will be analysed in detail.

4.1 General rules

4.1.1 Heat Exchange

The intricate nature of heat transfer poses significant analytical challenges. Within an electrical machine, the dissipation of heat involves a synergistic interplay of conduction, radiation, and convection processes, facilitating the transfer of thermal energy to the surrounding environment and ambient air.

4.1.1.1 Conduction

Conduction mainly takes place in solid materials and the heat rate is influenced by both the temperature difference and the material's thermal conductivity. In electrical devices, it becomes a significant issue when managing heat dissipation within solid components, including electrical conductors, magnetic iron, insulating materials and the framework. When a temperature gradient is present within a solid body, such as in materials like copper, steel, permanent magnets (PMs), or the insulation used in electrical machines, heat naturally flows from the higher-temperature region, denoted as θ_{hot}, to the lower-temperature region, represented by θ_{cold}. This thermal transfer follows Fourier's law, which can be expressed as:

$$\Delta P_c = -kA\frac{\delta\theta}{\delta x} = \frac{kA}{l}(\theta_{hot} - \theta_{cold}) \tag{4.1}$$

In this equation, ΔP_c stands for the rate of heat conduction, while A corresponds to the area of the heat flow path. The variable l denotes the length of this path, and k stands for the thermal conductivity of the material involved. It's worth noting that thermal conductivity, a material property, is determined experimentally and tends to exhibit relatively low sensitivity to temperature fluctuations.

The table 4.1 below shows the thermal properties of common materials utilised in axial flux permanent magnet (AFPM) machines, where c_p represents the specific heat of the material at constant pressure.

Material [20°C]	Grade	ρ [Kg/m^3]	c_p [$J/(Kg°C)$]	k [$W/(m\ °C)$]
Air	-	1.177	1005	0.0267
Water	-	1000	4184	0.63
Mica	-	3000	813	0.33
Epoxy resin	-	1400	1700	0.5
Copper	-	8950	380	360
aluminium	Pure	2700	903	237
	Alloy (cast)	2700	883	168
Steel	1% Carbon	7850	450	52
	Silicon	7700	490	20-30
Permanent magnet	Sintered NdFeB	7600 to 7700	420	9

Table 4.1: Thermal properties of materials. Source: [61]

4.1.1.2 Radiation

Radiation heat transfer is analogous to electromagnetic radiation, and within electrical machinery, it primarily occurs between solid surfaces separated by air gaps. The exchange of radiant energy between two surfaces at different temperatures is influenced by several factors, including the absolute temperature, emissivity, and the geometry of each surface. When heat is transferred via radiation between two finite-sized grey surfaces, denoted as A_1 and A_2, at temperatures θ_1 and θ_2 (in degrees Celsius), the rate of this heat transfer, denoted as ΔP_r, can be expressed as follows:

$$\Delta P_r = \sigma \frac{(\theta_1 + 273)^4 - (\theta_2 + 273)^4}{\frac{1-\epsilon_1}{\epsilon_1 A_1} + \frac{1}{A_1 F_{12}} + \frac{1-\epsilon_2}{\epsilon_2 A_2}} \tag{4.2}$$

In this equation, σ represents the Stefan-Boltzmann constant, and F_{12} accounts for the shape factor, which considers the relative orientation of the two surfaces. Additionally, ϵ_1 and ϵ_2 are the respective emissivities of the surfaces, which depend on their material properties and surface treatments.

A surface or body that ideally absorbs and emits energy at the maximum rate is referred to as a black surface or body. In practice, real surfaces or bodies are often approximated as grey surfaces or bodies, characterised by emissivities falling within the range of 0 to 1. Table 4.2 below provides selected emissivity values relevant to AFPM machines.

Material	Surface Condition	Emissivity ϵ
Copper	Polished	0.025
Epoxy	Black	0.87
	White	0.85
Mild Steel	-	0.2-0.7
Cast Iron	Oxidised	0.57
Stainless Steel	-	0.2-0.7
Permanent Magnet, NdFeB	Uncoated	0.9

Table 4.2: Emissivity of a selection of materials. Source: [61]

4.1.1.3 Convection

Convection stands out as the primary mode of heat transfer within liquid and gases, involving the conveyance of the thermal energy through fluid motion. In the context of electrical machinery, the utilisation of air liquid cooling systems prevails; convection, in fact, refers to the process of transferring heat from a surface to a moving fluid. The rate of convective heat transfer, denoted as ΔP_v, follows Newton's law of cooling, expressed as:

$$\Delta P_v = hA(\theta_{hot} - \theta_{cold}) \tag{4.3}$$

Here, the coefficient h represents the convection heat transfer coefficient, which exhibits complexity in its dependence on various factors such as surface finish, orientation, fluid properties, velocity, and temperature. Typically, this coefficient is determined through experimental methods, and it tends to increase with the velocity of the cooling medium relative to the surface being cooled. For surfaces subjected to forced ventilation, an empirical relation can be applied, as shown in:

$$h_f = h_n(1 + c_h\sqrt{v}) \tag{4.4}$$

In this equation, h_f and h_n denote the heat transfer coefficients for forced and natural convection, respectively. The variable v represents the linear velocity of the cooling medium, and the empirical coefficient c_h falls within the approximate range of 0.5 to 1.3.

The subsequent sections will delve into some essential formulas for the assessment of convective heat transfer coefficients specific to AFPM machines.

4.1.2 Conservation of Energy

The fields of thermodynamics and heat transfer are closely intertwined, complementing each other effectively. Heat transfer can be seen as an extension of thermodynamics, focusing on the rate at which heat moves.

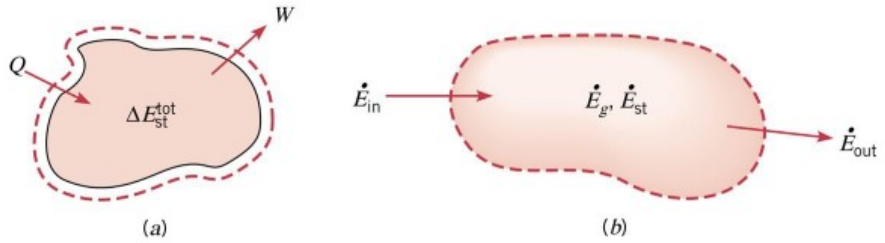

Figure 4.1: Conservation of energy. a) in the case of closed system within a time interval; b) for a control volume in a given time instant. Source: [65]

In various heat transfer scenarios, the first law of thermodynamics, which embodies the principle of energy conservation, becomes a valuable and often indispensable tool. To tackle these challenges, comprehensive formulations of the first law have been developed.

The first law of thermodynamics asserts the conservation of a system's total energy, with changes in energy occurring only when energy crosses its boundaries (Figure 4.1). It delineates how energy can flow through these boundaries.

For a closed system (with a fixed mass), there exist only two mechanisms: heat transfer across its boundaries and work performed on or by the system. This leads to the familiar expression for the first law in a closed system:

$$\Delta E_{st}^{tot} = Q - W \tag{4.5}$$

Here, ΔE_{st}^{tot} signifies the change in the total energy stored in the system, Q represents the net heat transfer to the system, and W is the net work done by the system.

In the context of a control volume (an open system), which includes a region enclosed by a control surface permitting mass flow, energy can also enter and exit with the flow of mass, known as energy advection.

In summary, the first law of thermodynamics can be concisely stated for both control volumes and closed systems as follows: "The increase in the energy stored in the control volume must equal the energy entering minus the energy leaving, accounting for energy advection."

4.1.3 Lumped Parameter Thermal Model

The lumped-capacitance model, often referred to as lumped system analysis, simplifies complex thermal systems by dividing them into discrete "lumps" and assuming negligible temperature differences within each lump. This mathematical approximation serves as an analogy to electrical capacitance and incorporates thermal analogous of electrical resistance.

In the field of electrical machines, this model finds widespread use in transient conduction, particularly when heat conduction within an object significantly outweighs heat transfer across its boundaries. When applied to electrical machines, such as motors and transformers, it simplifies the analysis of temperature distribution during operation. The key aspects of this model include:

- **Thermal Resistors:**
  These represent the resistance to heat flow within different parts of the machine, similar to electrical resistance. Thermal resistance (R) quantifies how effectively a material conducts, insulates, or dissipates heat (measured in units like °C/W).

- **Thermal Capacitors:**
  Thermal capacitors represent the thermal mass or heat storage capacity of machine components. Like electrical capacitors, they model the ability of materials or structures to store and release heat over time (measured in units such as J/°C).

- **Heat Sources:**
  Electrical machines generate heat through various mechanisms, including windings, core losses, and friction. These heat sources are integrated into the model as inputs contributing to temperature rise.

- **Node Analysis:**
  Similar to electrical circuit analysis, the model employs nodal analysis to calculate temperatures at specific points within the machine, with thermal resistors governing heat flows.

- **Time Constants:**
  Each thermal component has associated time constants (τ), indicating how quickly it responds to changes in heat input or disturbances. Time constants are crucial for understanding transient behaviour.

- **Steady-State and Transient Analysis:**
  The model aids in assessing both steady-state and transient temperature distributions, ensuring safe operation and efficient thermal management.

- **Limitations:**
  Recognition that lumped parameter thermal models are simplifications with assumptions of uniform temperature within each element. They may not capture fine-grained temperature variations.

The lumped parameter thermal model is a valuable tool in the realm of electrical machines. It simplifies complex thermal systems, allowing engineers to analyse temperature distributions, optimise designs, and ensure safe operating conditions.

4.2 Axial Flux Motor

4.2.1 Cooling Methods

Based on the machine's size and the enclosures employed, various cooling configurations may be adopted for AFPM machines. In terms of cooling, AFPM machines can be categorised into two distinct groups:

- **Self-Ventilated Machines:**
  In this category, cooling air is generated internally by components like rotating discs, PM channels, or similar fan-like mechanisms integrated into the machine's rotating components.
- **Externally-Ventilated Machines:**
  These machines rely on external devices, such as fans or pumps, to circulate the cooling medium for temperature control.

4.2.1.1 Self-Ventilation Machines

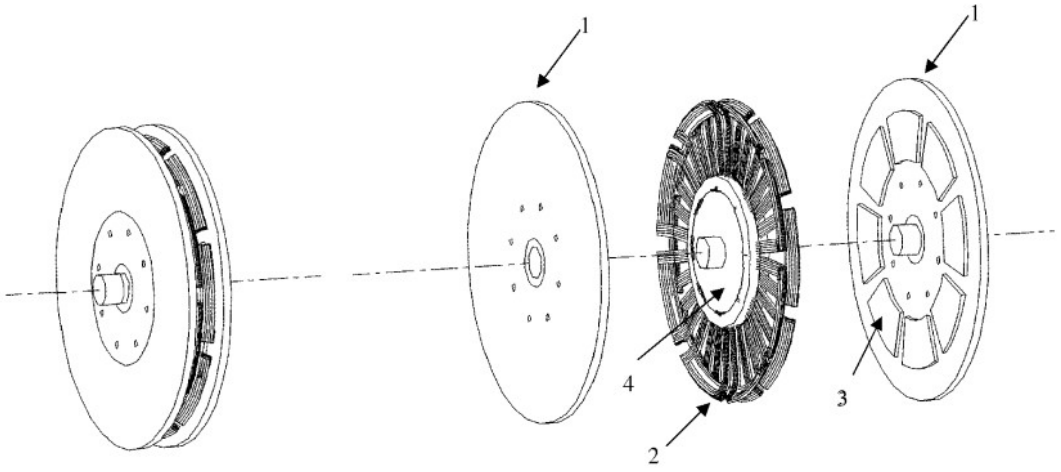

Figure 4.2: Exploded view of an AFPM machine: 1 — rotor disc, 2 — stator winding, 3 — PM, and 4 — epoxy core. Source: [61]

The majority of AFPM machines utilise air cooling as their primary cooling method. One particularly advantageous characteristic of disc-type AFPM machines, from a cooling perspective, is their inherent self-ventilation capability. The diagram (Figure 4.2) illustrates the arrangement and active components of a typical AFPM machine. A closer examination of the machine's structure reveals that as the rotor discs rotate, an airflow is induced through the air inlet openings into the machine and is subsequently directed outward into the radial channels.

Remarkably, the permanent magnets (PMs) effectively function as impeller blades in this process. The fluid behaviour within the AFPM machine closely resembles that of a centrifugal fan or compressor.

4.2.1.2 Externally-Ventilated Machines

In the case of medium to large power AFPM machines, there is a nearly linear correlation between the power ratings and the increase in loss per unit heat dissipation area. Consequently, the utilisation of external devices for forced cooling may become imperative. The ensuing paragraphs outline several methods for achieving this, i.e. external fans, heat pipes or direct water cooling.

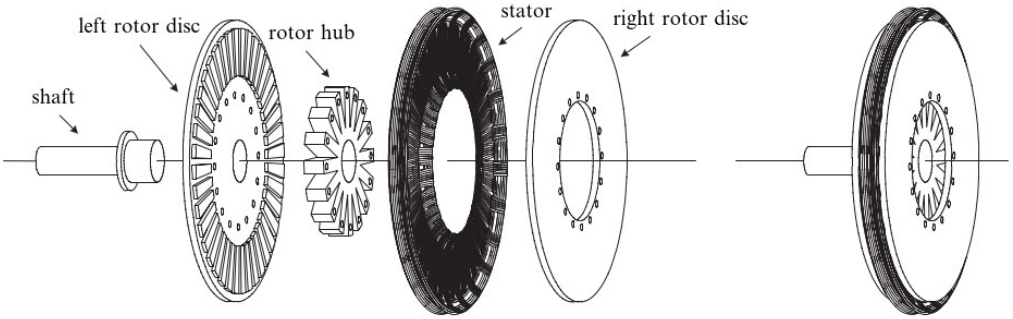

Figure 4.3: Exploded view of shaft-integral fan in AFPM machine. Source: [61]

4.2.1.2.1 External Fans: Large AFPM (Axial Flux Permanent Magnet) machines may demand a substantial volume of airflow per unit of time to effectively dissipate the heat generated within the stator windings. Depending on the operational conditions encountered on-site, the choice may lean towards either employing an air-blast fan or a suction fan. In either scenario, the utilisation of intake and/or discharge ducts becomes necessary to direct and regulate the airflow. It's worth noting that the temperature of the incoming air, at a given volumetric flow rate, exerts a noteworthy influence on the machine's overall temperature. Furthermore, this cooling arrangement serves the additional purpose of mitigating the possibility of hot air recirculation, particularly when the machine operates within confined spaces, such as a small machine room. In the case of high-speed AFPM machines, integrating a fan directly into the shaft (shaft-integral fan) can present an advantageous cooling solution (Figure 4.3).

4.2.1.2.2 Heat Pipes: A typical heat pipe comprises a sealed enclosure containing wicking material. This container is subjected to evacuation and subsequently filled with an appropriate quantity of liquid to completely saturate the wick. Within a heat pipe (Figure 4.4), there exist three distinct regions: (i) an evaporator, where heat is introduced, (ii) a condenser, where heat is dissipated, and (iii) an adiabatic or isothermal region.

When the evaporator region is exposed to elevated temperatures, heat is supplied, causing the working fluid within the wick to undergo vaporisation. The high temperature in this area, along with the resulting high pressure, drives the vapour toward the cooler condenser region. Here, the vapour condenses, releasing its latent heat of vaporisation. Capillary forces within the wick structure facilitate the return of the liquid to the evaporator. This wicking mechanism ensures that a heat pipe can efficiently transfer heat, regardless of whether the heat source is situated above or below the cooled end.

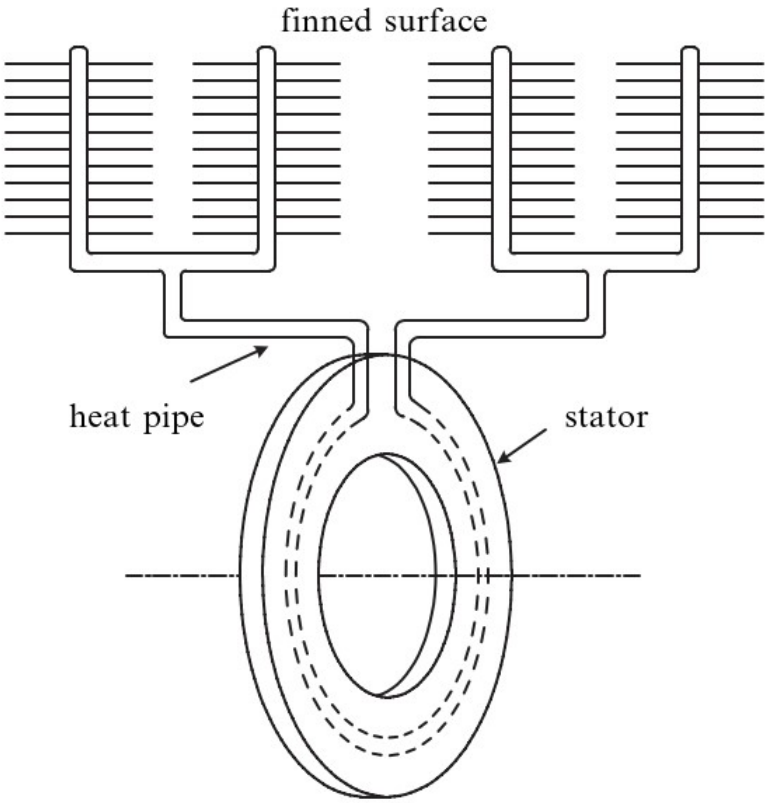

Figure 4.4: AFPM machine cooled by heat pipes. Source: [61]

A heat pipe offers an alternative approach for dissipating heat from the AFPM (Axial Flux Permanent Magnet) machine. In an AFPM machine, the heat pipe can be configured as depicted in the figure. Heat is then transferred to the surroundings through the finned surface, which is cooled by the movement of air over the fins. The heat loss removed by the heat pipe (P_{hp}) can be calculated using the formula:

$$\Delta P_{hp} = \frac{\theta_{hot} - \theta_{cold}}{\frac{1}{h_{hot}A_{hot}} + \frac{1}{h_{cold}A_{cold}} + \frac{1}{\eta_{fin}h_{fin}A_{fin}}} \tag{4.6}$$

where various parameters such as the average temperature of surrounding elements (θ_{hot} and θ_{cold}), convective heat transfer coefficients (h_{hot} and h_{cold}), exposed areas (A_{hot} and A_{cold}), fin efficiency (η_{fin}), convection heat transfer coefficient on fin surfaces (h_{fin}), and total exposed area of the finned surface (A_{fin}) are taken into account.

4.2.1.2.3 Direct Water Cooling: In many cases, it becomes necessary to employ a method of forced water circulation to achieve effective cooling of the stator windings in AFPM machines, particularly those with significant power output. The implementation of this cooling process entails the use of an external water pump to facilitate the circulation of water. When it comes to AFPM machines featuring an internal iron core stator, an optimal strategy is to position cooling channels along the outer edge of the stator disc, as this location offers the most efficient heat transfer area. In the case of coreless winding AFPM machines, the winding coils may adopt a rhomboidal shape, allowing for the placement of a cooling water duct in the space between the two active sides of each coil. The removed heat can be calculated with the formula (4.6), where the values h_{hot} and h_{cold} can be evaluated as follow, depending on the conditions of the fluid flow:

- Laminar flow: $Re_d = \frac{\rho v d}{\mu} < 2000$
  where d is the pipe's diameter and v the flow velocity, while μ and ρ are proper parameters of the fluid.
  The Nusselt number is then calculate as:

$$Nu_d = 1.86(Re_d Pr)^{1/3}(\frac{d}{L_p})^{1/3}(\frac{\mu}{\mu_w})^{0.14} \tag{4.7}$$

  L_p is the length of the water pipe and μ_w is the wall temperature.

- Turbulent flow: $Re_d = \frac{\rho v d}{\mu} > 2000$
  The Nusselt number is then:

$$Nu_d = 0.023 Re_d^{0.8} Pr^n \tag{4.8}$$

  and

$$n = \begin{cases} 0.4 \text{ for water heating} \\ 0.3 \text{ for water cooling} \end{cases} \tag{4.9}$$

4.2.2 Lumped Parameter Model: Thermal Equivalent Circuit

As previously said in this chapter, lumped-parameter circuits have been widely employed to model the intricate distributed thermal characteristics found in electrical machines. These circuits encompass a network of thermal resistances, thermal capacitances, nodal temperatures, and heat sources for this purpose. It is interesting to analyse in detail the procedure used to build the **thermal equivalent circuit** of a AFPM machine.
A thermal equivalent circuit operates on the principle of analogy with an electrical circuit. In this analogy, the flow of heat, similar to electrical current, within each pathway of the circuit is determined by the temperature difference, akin to voltage, divided by a thermal resistance, which is analogous to electrical resistance. Examining the case of AFPM machine, it is possible to model only half of the machine, given its symmetrical structure (Figure 4.5).

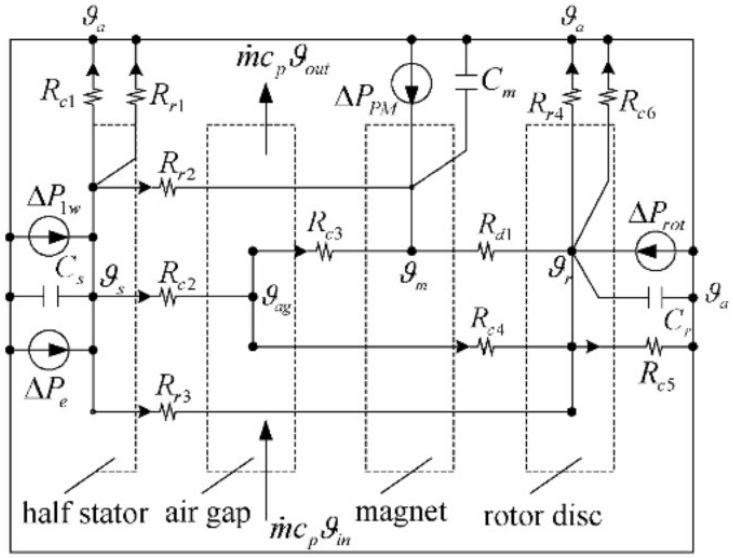

Figure 4.5: Thermal equivalent circuit of AFPM machine. Source: [61]

The heat sources are the losses, in particular rotational losses per one rotor disc ΔP_{rot} (eq. 2.37), losses in PMs ΔP_{PM}, winding losses ΔP_{1w} (eq. 2.31) and eddy current losses in one half of the stator winding ΔP_e (eq. 2.32). Heat resistances present in the circuit are (R_c stands for convection resistance, R_r is the radiation resistance and R_d the conduction resistance):

Symbols	from	to
R_{c1}	Stator end-winding	Open air
R_{c2}	Stator	Air-gap
R_{c3}	Air-gap	Permanent magnets
R_{c4}	Air-gap	Rotor disc plate
R_{c5}	Rotor disc	Open air
R_{c6}	Rotor radial periphery	Open air
R_{r1}	Stator end-winding	Environment
R_{r2}	Stator	Permanent magnets
R_{r3}	Stator	Rotor disc
R_{r4}	Rotor radial periphery	Environment
R_{d1}	PMs	Rotor disc

Table 4.3: Heat resistances

While the thermal capacitances:

Symbols	
C_s	Stator
C_m	PMs
C_r	Rotor

Table 4.4: Thermal capacitances

In case of conduction, the resistance formula is:

$$R_d = \frac{l}{A_d k} \tag{4.10}$$

where k is the thermal conductivity of the material, l is the length and A_d the cross-sectional area of the heat flow path.
The thermal convection resistances:

$$R_c = \frac{1}{A_c h} \tag{4.11}$$

where h is the convection coefficient and A_c is the surface area of convective heat transfer between two regions.
For what concerns the radiation thermal resistance, its equation hinges on the combination of differences of factors, namely the third power of the temperature, the surface's spectral property represented by ϵ, and the surface's orientation, which is factored in through a form factor denoted as F:

$$R_r = \frac{\frac{1-\epsilon_1}{\epsilon_1 A_1} + \frac{1}{A_1 F_{12}} + \frac{1-\epsilon_2}{\epsilon_2 A_2}}{\sigma[(\theta_1 + 273) + (\theta_2 + 273)][(\theta_1 + 273)^2 + (\theta_2 + 273)^2]} \tag{4.12}$$

The heat capacitances:

$$C = \rho V c_v = m c_v \tag{4.13}$$

where c_v is the heat capacity, ρ the density, m the mass and V the volume of the material. In a steady-state condition, the thermal circuit is comprised of thermal resistances and heat sources that link different nodes within the motor components. However, when conducting transient analysis, thermal capacitances are introduced as well.
These capacitances are essential to accommodate the alterations in internal energy within the different sections of the machine over time.
In the analysis of lumped parameter thermal circuits, it is common to assume that temperature variations within specific sections of the machine are negligible. This assumption is valid only when the resistance to heat transfer within the machine is much smaller than the resistance outside of it. To assess the validity of this assumption, the Biot number, denoted as Bi, is often employed. The Biot number is calculated as follows:

$$B_i = \frac{\bar{h}_c L}{k_s} \tag{4.14}$$

Where:
k_s represents the thermal conductivity of the solid material;
L is the characteristic length of a solid body;
h_c is the convective heat transfer coefficient.
A widely accepted criterion is $B_i < 0.1$, which ensures that the internal temperature does not deviate by more than 5% from the temperature at the surface of a solid body. This criterion is frequently used to determine the applicability of the assumption.
When the principle of energy conservation is employed, the alteration in internal energy rate within individual sections of a machine can be expressed, commonly, referred to as a control volume. In the case of steady state condition the formula is the following one:

$$0 = \Delta P_{in} - \Delta P_{out} + \dot{m}_{in} i_{in} - \dot{m}_{out} i_{out} \tag{4.15}$$

The last two elements of this equation represent the heat flow exchange due to the air pumped through the machine. These equations are employed for each component of the AFPM machine to derive a system of equations in which the temperatures of these components serve as the sole variables.

4.3 Radial Flux Motor

The rules used to make a thermal model and analysis of PMSM machines are not so far from the ones used in the case of AFPM machines. The main difference is represented by the thermal equivalent circuit, used to determine the internal temperature distribution and to model the heat transfer of the machine. Table 4.5 presents a comparison of thermal and electrical parameters in a manner that draws analogies between them. Specific aspects like resistive losses, iron losses, windage losses, and friction losses are depicted as distinct heat sources. Additionally, the thermal resistances of components such as iron cores, insulation, and the frame are quantified as resistance values. The circuit elements presented for representations in terms of concentrated parameters can also be interpreted as values per unit length and used for distributed equivalents, as both examples will be explored further.

Thermal flow	Symbol	Unit	Electric flow	Symbol	Unit
Heat quantity	Q_{th}	J	Electric charge	Q	C
Heat flow rate	Φ_{th}	W	Electric current	I	A
Heat flow density	q_{th}	W/m^2	Current density	J	A/m^2
Temperature	T	K	Electric potential	V	V
Temperature rise	Θ	K	Voltage	U	V
Thermal conductivity	λ	W/mK	Electric conductivity	σ	$S/m = A/Vm$
Thermal resistance	R_{th}	K/W	Electric resistance	R	$\Omega = V/A$
Thermal conductance	G_{th}	W/K	Electric conductance	G	S=A/V
Heat capacity	C_{th}	J/K	Capacitance	C	$F = C/V$

Table 4.5: Thermal and electrical quantities relationship. Source: [66]

The analogy between heat capacity and electric capacitance is evident as follows:
In the case of an electric capacitor, the stored electric charge Q can be expressed as:

$$Q = C\Delta V = CU \tag{4.16}$$

Here, C represents the capacitance of the capacitor, and U is the voltage applied across it.
On the other hand, when it comes to the quantity of heat Q_{th} stored within a substance, it can be represented as:

$$Q_{th} = mc_p\Theta \tag{4.17}$$

In this equation, m denotes the mass of the substance, c_p signifies the specific heat capacity, and Θ indicates the temperature increase resulting from the heat Q_{th}.
Upon comparing these equations, it is possible to conclude that the heat capacity C_{th}, can be analogously likened to the electric capacitance C:

$$C_{th} = mc_p \tag{4.18}$$

In Figure 4.6, a thermal equivalent circuit for a typical electrical machine is presented. This circuit assumes that heat primarily travels radially within the stacks, as axial thermal conductivity is considerably lower. Furthermore, it assumes that heat flows from the slots to the teeth and not directly to the yoke, as slots are typically deep and narrow, limiting heat transfer to the yoke.

This equivalent circuit comprises a total of 21 nodes, with specific nodes (indicated by circles with node numbers) representing where the machine's losses are supplied. The circuit is connected to a cooling system through nodes 18 to 21.

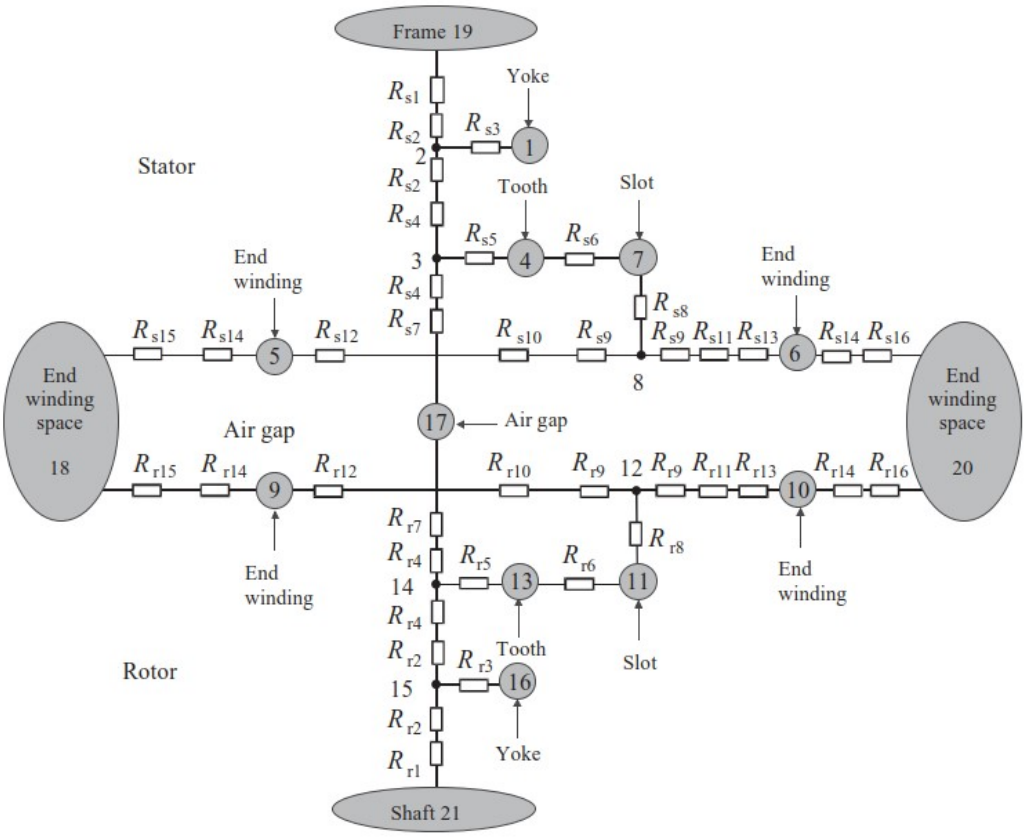

Figure 4.6: Typical thermal equivalent circuit. Source: [66]

The parameters for individual components of the equivalent circuit will be explained shortly. The modelling initially focuses on a winding with rectangular-shaped conductors in a slot (Figure 4.8). It considers factors such as copper temperature variation along the axial direction, insulation layers, and wire insulation.

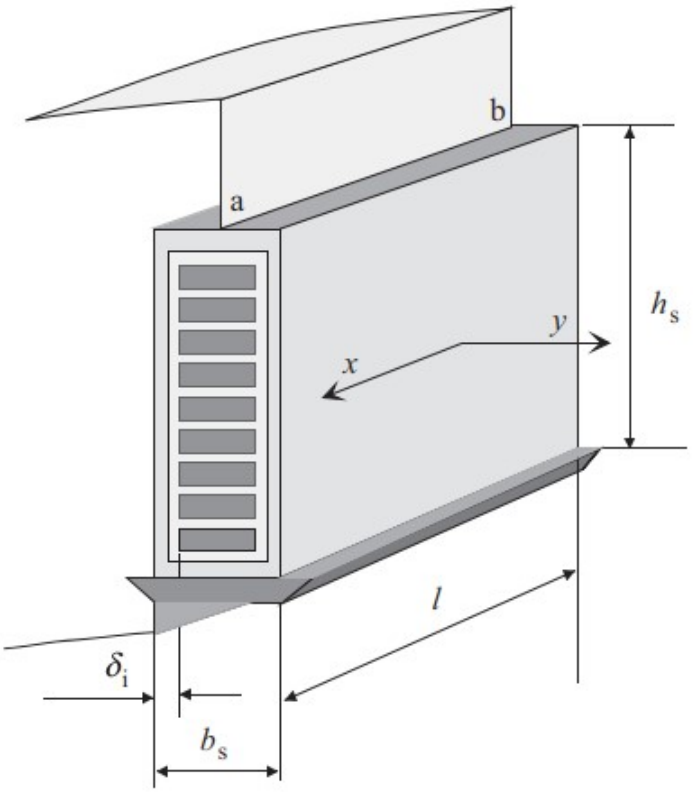

Figure 4.7: Section of a winding with rectangular conductors in a slot. Source: [66]

The winding and tooth components are simplified in Figure 4.8a and extended into an equivalent circuit with distributed constants in Figure 4.8b. The winding is divided into small sections of length dx, and resistive losses (P_{Cu}) divided by the core length (l) are represented as

$$p = P_{Cu}/l \tag{4.19}$$

The thermal resistance (R) between points a and b divided by the core length is given by :

$$r = \frac{R}{l} = \frac{1}{\lambda_{Cu} S_{Cu}} \tag{4.20}$$

where λ_{Cu} is the thermal conductivity, and S_{Cu} is the total cross-sectional area of conductors in a slot.

The thermal conductance (G), the inverse of thermal resistance, from conductors to the tooth per unit core length is represented as

$$g = G/l \tag{4.21}$$

This conductance includes insulation resistance and contact resistance between insulation and the tooth. The overall heat transfer coefficient ($k_t h$) is given by the equation:

$$k_{th} = 1/(\sigma_i/\lambda_i + 1/\alpha_{th}) \tag{4.22}$$

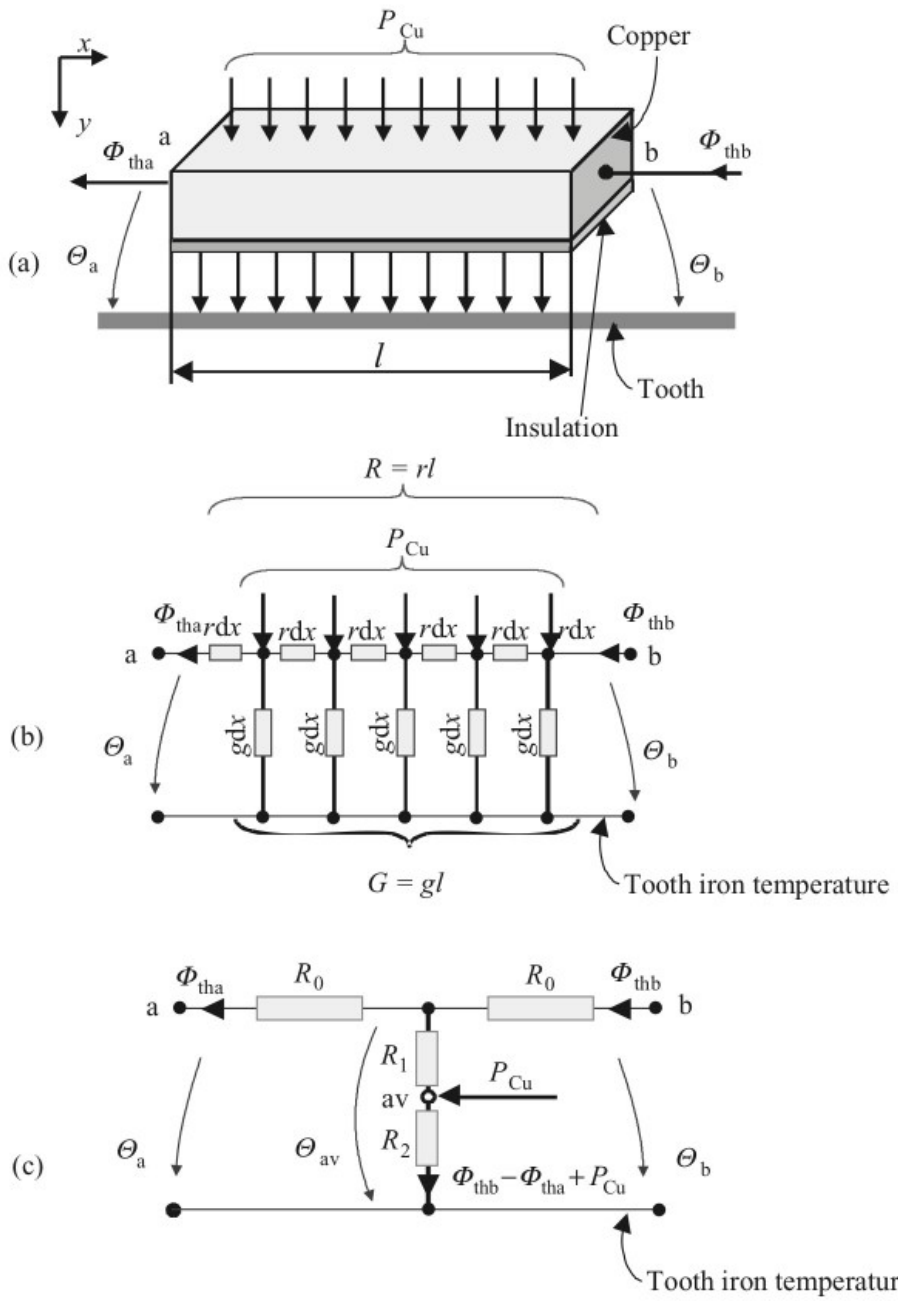

Figure 4.8: (a) A simplified depiction of Figure 4.8. (b) The thermal equivalent circuit represented using distributed constants. (c) The circuit represented using lumped constants. Source: [66]

The equivalent circuit with lumped constants is presented in Figure 4.8c. This provides temperature rise information for points a and b and the average temperature rise (Θ_{av}) of the winding part in the slots. The total losses (P_{Cu}) in the slots are supplied to the node representing the average temperature.
To calculate the components of the equivalent circuit, equations for temperature distribution are derived from the circuit with distributed constants.

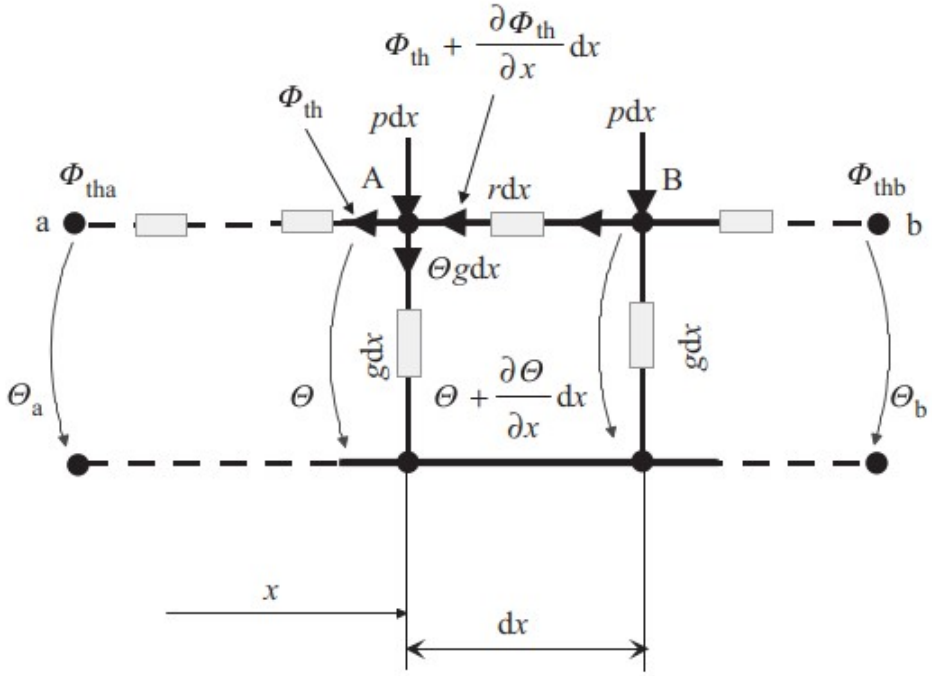

Figure 4.9: Equivalent circuit used to derive the differential equation for the heat flow in a winding. Source: [66]

At distance x from point a, heat generation at point A is $p \cdot dx$, and the heat flow through the insulation is $\Theta \cdot g \cdot dx$. Applying heat flow principles, equations for heat flow and temperature rise at points A and B are established:

$$g\Theta = p + \frac{\delta \Phi_{th}}{\delta x} \tag{4.23}$$

and

$$\frac{\delta \Theta}{\delta x} = \Phi_{th} r \tag{4.24}$$

These equations are used to derive the temperature distribution equation:

$$\frac{\delta^2 \Phi_{th}}{\delta x^2} - rg\Phi_{th} = 0 \tag{4.25}$$

which has a solution Φ_{th}:

$$\Phi_{th} = C_1 e^{\sqrt{rg}x} + C_2 e^{-\sqrt{rg}x} \tag{4.26}$$

and temperature rise Θ at any distance x from point a.

$$\Theta = \frac{1}{g}(C_1\sqrt{rg}e^{\sqrt{rg}x} - C_2\sqrt{rg}e^{-\sqrt{rg}x} + p) \tag{4.27}$$

Integration constants C_1 and C_2 are determined using boundary conditions:

$$C_1 = \frac{1}{2}(\Phi_{tha} + \sqrt{\frac{g}{r}}\Theta_a - \frac{p}{\sqrt{rg}} \tag{4.28}$$

$$C_2 = \frac{1}{2}(\Phi_{tha} - \sqrt{\frac{g}{r}}\Theta_a + \frac{p}{\sqrt{rg}} \tag{4.29}$$

and the final expressions for Φ_{th} and Θ are obtained with:

$$\Phi_{th} = \Phi_{tha}cosh(\sqrt{rg}x) + \Theta_a\sqrt{\frac{g}{r}}sinh(\sqrt{rg}x) - \frac{p}{\sqrt{rg}}sinh(\sqrt{rg}x) \tag{4.30}$$

$$\Theta = \Phi_{tha}\sqrt{\frac{g}{r}}sinh(\sqrt{rg}x) + \Theta_a cosh(\sqrt{rg}x) + \frac{p}{g}[1 - cosh(\sqrt{rg}x)] \tag{4.31}$$

The average temperature (Θ_{av}) is calculated using this expression:

$$\Theta_{av} = \frac{1}{G}(cosh(\sqrt{RG}) - 1)\Phi_{tha} + \frac{sinh(\sqrt{RG})}{\sqrt{RG}}\Theta_a + \frac{P_{Cu}}{G}(1 - \frac{sinh(\sqrt{RG})}{\sqrt{RG}}) \tag{4.32}$$

The components of the equivalent circuit with lumped constants are then determined using equations that relate Φ_{thb}, Θ_b, Φ_{tha}, and Θ_a:

$$\Phi_{thb} = \Phi_{tha}cosh(\sqrt{RG}) + \Theta_a\sqrt{\frac{G}{R}}sinh(\sqrt{RG}) - \frac{P_{Cu}}{\sqrt{RG}}sinh(\sqrt{RG}) \tag{4.33}$$

$$\Theta_b = \Phi_{tha}\sqrt{\frac{G}{R}}sinh(\sqrt{RG}) + \Theta_a cosh(\sqrt{RG}) + \frac{P_{Cu}}{G}[1 - cosh(\sqrt{RG})] \tag{4.34}$$

These equations allow the calculation of R_0, R_1, R_2, and other resistances in the equivalent circuit (Figure 4.8c).

$$R_0 = \sqrt{\frac{R}{G}}tanh(\frac{\sqrt{RG}}{2}) \tag{4.35}$$

$$R_1 = \frac{1}{G}(\frac{\sqrt{RG}}{sinh(\sqrt{RG})} - 1) \tag{4.36}$$

$$R_2 = \frac{1}{G} \tag{4.37}$$

With reference to the equivalent circuit in Figure 4.6, the stator winding resistances in the slots are: R_{s6}, R_{s8}, R_{s9}, and node 7, while the end windings are R_{s10}, R_{s12}, R_{s14}, R_{s15}, R_{s11}, R_{s13}, R_{s14}, R_{s16}, and nodes 5 and 6. The yoke's resistances: R_{s2}, R_{s3}, and node 1 and air gap (node 17) are also represented, with the relevant thermal resistances calculated based on their respective parameters. The rotor's equivalent circuit is similar to the stator but with rotor-specific parameters.

Chapter 5

Motor Parameters Design

5.1 General Rules

In light of recent advancements in power electronics, the emergence of novel magnetic materials, and evolving applications and manufacturing techniques for electric machines, there is a growing demand for a more streamlined and efficient design approach to harness these enhancements. The conventional design methodology has long relied on semi-empirical sizing equations, offering general and heuristic principles that primarily draw from designers' practical insights. Additionally, it has been built upon a finite set of material curves that are not inherently designed to provide precise or universally reliable results for all scenarios. Following the establishment of electrical and magnetic loadings for the machine, the traditional procedure necessitates iterative processes for fine-tuning certain parameters. Here are the main steps typically followed in the design process (Figure 5.1):

- **Define the Purpose and Specifications:**
  Determine the specific application and purpose of the electric machine. What is it intended to do? What are the desired performance characteristics (e.g., power output, efficiency, voltage, current, speed)? Consider environmental factors such as temperature, humidity, and operating conditions that may affect the machine's design.

- **Select the Type of Machine:**
  Choose the appropriate type of electric machine for the application. Common types include generators, motors and transformers, each with unique designs and functions.

- **Design the Electrical Circuit:**
  Create the electrical circuit for the machine, including the arrangement of coils, windings, and connections. For motors and generators, determine the number of phases (single-phase or three-phase) and the type of winding (e.g., lap, wave, concentric).

- **Determine Magnetic Circuit Parameters:**
  Calculate the magnetic circuit parameters, such as magnetic flux density and magnetic path length. Magnetic design is crucial for efficient energy conversion in electric machines.

- **Select Materials:**
  Choose suitable materials for the core, windings, insulation, and other components. Material selection impacts the machine's performance, efficiency, and cost.

- **Size and Dimensioning:**
  Determine the physical dimensions of the machine, including the core size, coil dimensions, and rotor/stator geometry. These dimensions should align with the electrical and magnetic design parameters.

- **Mechanical Design:**
  Design the mechanical components of the machine, such as the shaft, bearings, and housing. Mechanical design considerations include load-bearing capacity and alignment.

- **Electromagnetic Analysis:**
  Conduct electromagnetic analysis, such as finite element analysis (FEA), to assess the machine's performance, magnetic field distribution, and losses. This helps refining the design for optimal efficiency.

- **Cooling and Thermal Management:**
  Implement cooling mechanisms to dissipate heat generated during operation. Proper thermal management is essential to prevent overheating and ensure long-term reliability.

- **Simulation and Prototyping:**
  Create computer simulations or physical prototypes to validate the design and test its performance under various conditions. Iterate on the design as necessary to meet specifications.

- **Manufacturing and Assembly:**
  Once the design is finalised and validated, proceed with manufacturing the components and assembling the machine. Pay close attention to quality control to ensure reliability.

- **Testing and Validation:**
  Perform rigorous testing to verify that the machine meets the specified performance criteria. This includes electrical testing (voltage, current, efficiency), mechanical testing (vibration, noise), and thermal testing.

- **optimisation:**
  Continuously seek opportunities to optimise the design for improved performance, efficiency, and cost-effectiveness. This may involve fine-tuning parameters or exploring new materials and technologies.

- **Compliance and Certification:**
  Ensure that the electric machine complies with relevant industry standards, safety regulations, and certification requirements.

- **Deployment and Maintenance:**
  Install the electric machine in its intended application and establish a maintenance plan to ensure long-term reliability and performance.

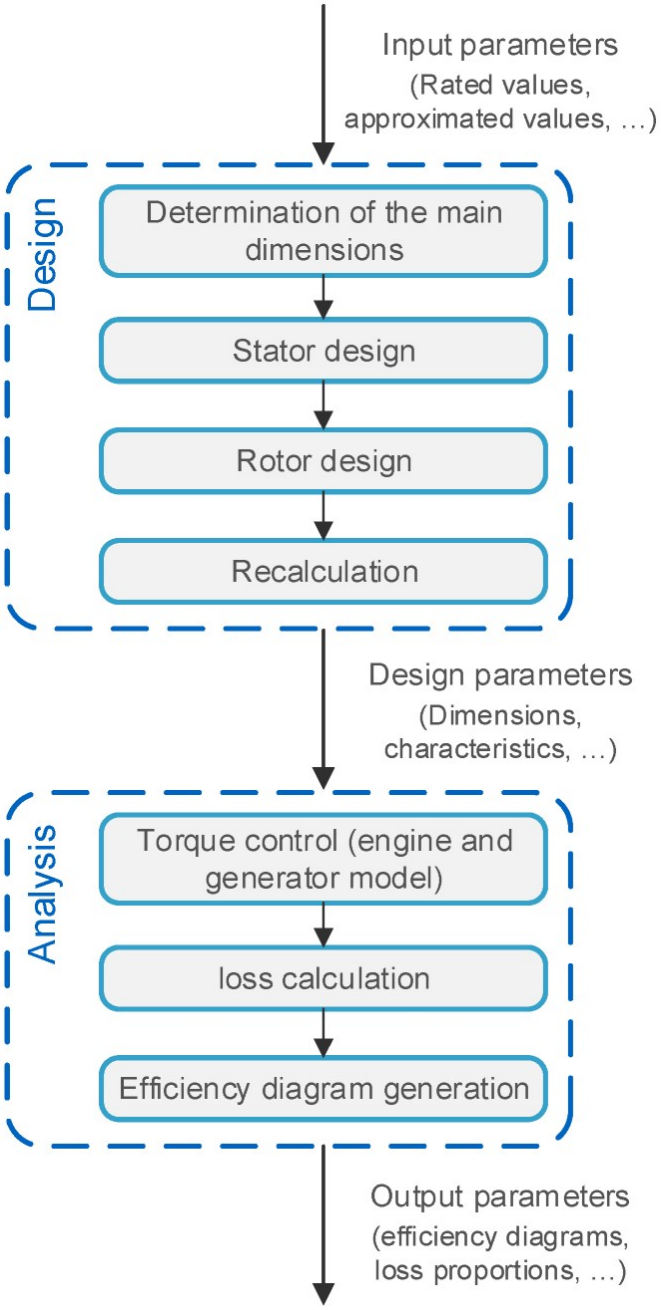

Figure 5.1: Overview of implementation of electric machine design model.

This paragraph will comprehensively address the selection and optimisation of parameters for both axial and radial flux electric machine models, ensuring alignment with the project partners' PNRR requirements. Additionally, an analysis of the thermal model for both machines will be conducted, and an effective cooling method will be proposed.

5.2 Axial Flux Machine Model

As axial flux motors are part of a relatively unexplored domain, the initial challenges of this project were encountered during the model development due to the limited available references for constructing an adequately accurate equivalent model.
The initial step for the production of an electric machine, as previously said, involves creating the equivalent model using software capable of swiftly performing complex calculations and allowing for the adjustment of input values without the need to alter the basic model. MATLAB is well-suited for this purpose. The results are then validated through finite element analysis with the Ansys Maxwell and MotorXP software.
Given the high power and torque requirements imposed by the groups involved in the PNRR project (Figure 5.2), the challenge proved to be intriguing.

FPT ON axis Specs	Value	eAxle [Ferrari]	P2 Hybrid [Ferrari]
Machine Type	3 Phase		
Battery Voltage Range	520V...810V w/o derating	550-870V max	
Peak Power	>350kW		
Cont. Power	>250kW		
Peak Torque	>1200Nm @0rpm, >1400Nm with motion		
Cont. Torque	>800Nm		
Max. Operating Speed	10 000rpm		
Peak Efficiency	>97%		
Stator OD	≤400mm		
Rotor ID	≥245mm		
Axial Length	<200mm		
Cooling Provision	Liquid Cooling, W-G and or Oil		
Max. Winding Temp	180°C to 200°C		
Max. PM	165°C	TBC (verifica)	

Figure 5.2: Requirements set by the industrial partners of PNRR project.

To summarise the steps accomplished so far: the purpose and specifications are defined by the PNRR project partners, the chosen type of machine is the axial flux permanent magnet machine, and the theoretical rules to follow have been largely explained in Chapter 2.
The next step along the route is then to choose an appropriate set of parameters that meet the requirements. To achieve the maximum efficiency, output torque, and power while adhering to constraints, MATLAB analysis employed an optimisation algorithm. Specifically, it was utilised to define validity intervals for specific variables, their associated correlations, and relevant constraints, ensuring the fulfilment of specified requirements without the need for trial-and-error procedures.
The chosen function to use has been *"fmincon"* MATLAB function, it is a nonlinear programming solver which finds the minimum of a problem specified by:

$$\min_x f(x) \, such \, that \begin{cases} c(x) \leq 0 \\ ceq(x) = 0 \\ A \cdot x \leq b \\ Aeq \cdot x = beq \\ lb \leq x \leq ub \end{cases} \tag{5.1}$$

b and beq are vectors, A and Aeq are matrices, $c(x)$ and $ceq(x)$ are functions that return vectors, and $f(x)$ is a function that returns a scalar. $f(x)$, $c(x)$, and $ceq(x)$ can be nonlinear functions. x, lb, and ub can be passed as vectors or matrices [67].
In particular, the used structure is:

$$x = fmincon(fun, x0, A, b, Aeq, beq, lb, ub, nonlcon, options) \tag{5.2}$$

which minimises with the optimisation options specified in *options* by the use of *optimoptions*. *nonlcon* contains nonlinear inequality or equality constraints. The function returns an optimised solution, i.e., the values of your variables that maximise the efficiency η.

5.2.1 The Developed Design

When provided with the input vector x_0, which sets the initial values, and the arrays lb and ub, defining the lower and upper bounds for each element, as explained previously, the algorithm produces a new array containing optimal values that adhere to the specified constraints. These optimised values are compiled in Table 5.1 and serve as input for the custom script used to estimate prospective output torque, power, losses, efficiency, and various motor parameters.

B_r[T]	μ_{rrec}	t[mm]	t_w[mm]	h_M[mm]	D_{out}[m]	D_{in} [m]	p	s_1	N_{ct}
1.125	1.051	18.00	16.00	10.53	0.4000	0.2450	20	60	12
a_w	d_w[mm]	w_c	I_a[A]	k_{sat}	m_r[kg]	m_{sh}[kg]	R_{sh}[mm]	m_1	rpm
100	13.10	1	115.0	1	15.78	0	0	3	3000

Table 5.1: Output optimised values that are the input for the motor model MATLAB script

Recalling from Chapter 2.2 B_r is the residual induction, μ_{rrec} the recoil permeability ($\mu_{rrec} = 1.125/(mu_o 852000)$ where $m_o = 0.4\pi 10^{-6}$), t the non-magnetic distance between opposite PMs, t_w the winding thickness, h_M the height of the PMs in axial direction, D_{out} and D_{in} outer and inner diameters, p the pole pair number, s_1 the number of slots, N_{ct} the number of turns per coil, a_w the number of parallel conductors, d_w the diameter of the wire, w_c the coil pitch per coil side, I_a input armature current, k_{sat} the saturation factor of the magnetic circuit, m_r the rotor mass, m_{sh} and R_{sh} the mass and radius of the shaft (which will be neglected for this first analysis due to the absence of specific indications from the PNRR project partners and to simplify the already complex motor design), m_1 the number of phases and rpm the motor velocity in revolution per minute.
The following paragraph presents various results related to the performance and characteristics of the described motor system. These results encompass a range of parameters, including losses and physical properties, shedding light on the motor's efficiency and behaviour. Each result is associated with its corresponding equation:

$\sigma_{copper} = 5.960 \cdot 10^7\,\mathrm{S/m}$	$\rightarrow$	Conductivity of copper conductors at 75°C
$\rho_{copper} = 8.940 \cdot 10^3\,\mathrm{kg/m^3}$	$\rightarrow$	Specific density of copper conductors
$\rho_{PM} = 7.600 \cdot 10^3\,\mathrm{kg/m^3}$	$\rightarrow$	Density of PMs
$\rho_{air} = 1.200\,\mathrm{kg/m^3}$	$\rightarrow$	Air density
$\rho_{fe} = 7.850 \cdot 10^3\,\mathrm{kg/m^3}$	$\rightarrow$	Density of iron
$\mu_{air} = 1.800 \cdot 10^{-5}\,\mathrm{Pa \cdot s}$	$\rightarrow$	Dynamic viscosity of the air
$k_{fb} = 1.500$	$\rightarrow$	Coefficient of bearing friction
$\eta_d = 1.000$	$\rightarrow$	Coefficient of distortion of the magnetic flux density

Continuing the analysis in accordance with reference to the structure outlined in Chapter 2:

$n_c = 20$	$\rightarrow$	Number of coils per phase (Eq. 2.1)
$q_1 = 0.500$	$\rightarrow$	Number of coil side per pole per phase (Eq. 2.3)
$\tau_c = 1.500$	$\rightarrow$	Pole pitch measured in coil sides (Eq. 2.4)
$f = 1.000 \cdot 10^3\,\text{Hz}$	$\rightarrow$	Input frequency (Eq. 2.5)
$B_{mg} = 0.593\,\text{T}$	$\rightarrow$	Air gap magnetic induction (Eq. 2.6)
$\phi_f = 7.407 \cdot 10^{-4}\,\text{Wb}$	$\rightarrow$	Magnetic flux (Eq. 2.7)
$k_{d1} = 1.155$	$\rightarrow$	Distribution factor (Eq. **??**)
$k_{p1} = 0.866$	$\rightarrow$	Pitch factor (Eq. 2.10)
$k_{w1} = 1.000$	$\rightarrow$	Winding factor (Eq. 2.8)
$\beta = 0.667$	$\rightarrow$	Coil pitch-to-pole pitch ratio (Eq. 2.11)
$k_E = 0.263\,\text{V/rpm}$	$\rightarrow$	EMF constant (Eq. 2.13)
$k_T = 7.542\,\text{Nm/A}$	$\rightarrow$	Torque constant (Eq. 2.14)
$E_f = 7.898 \cdot 10^2\,\text{V}$	$\rightarrow$	EMF at the given speed (Eq. 2.15)

The results of note include an electromagnetic torque (T_d) of $8.673 \cdot 10^2\,\text{Nm}$ (Eq. 2.16). This torque represents the rotational force generated, and an electromagnetic power (P_{elm}) of $2.725 \cdot 10^5\,\text{W}$ (Eq. 2.17), indicating the mechanical power output. These results are essential for assessing performance and understanding the system's ability to perform work or generate mechanical power.

$\tau = 0.025\,\text{m}$	$\rightarrow$	Average pole pitch (Eq. 2.19)
$L_i = 0.078\,\text{m}$	$\rightarrow$	Length of conductors (Eq. 2.20)
$l_{1emin} = 0.013\,\text{m}$	$\rightarrow$	Length of shorter end connection (Eq. 2.21)
$l_{1emax} = 0.021\,\text{m}$	$\rightarrow$	Length of the longer end connection (Eq. 2.22)
$l_{1av} = 0.189\,\text{m}$	$\rightarrow$	Average length of the stator turn (Eq. 2.23)
$R_1 = 0.282\Omega$	$\rightarrow$	Stator winding resistance at 75°C (Eq. 2.24)
$k_{fmax} = 0.100$	$\rightarrow$	Maximum value of the coil packing factor (Eq. 2.29)
$j_a = 85.32\,\text{A/mm}^2$	$\rightarrow$	stator current density (Eq. 2.30)

This list highlights crucial losses within the motor system, encompassing stator winding losses, eddy current losses, friction losses in bearings, windage losses, and total rotational losses:

$\Delta P_{1w} = 1.119 \cdot 10^4\,\text{W}$	$\rightarrow$	Stator winding losses (Eq. 2.31)
$m_{con} = 1.345\,\text{Kg}$	$\rightarrow$	Overall mass of the copper conductors (Eq. 2.33)
$\Delta P_e = 1.334 \cdot 10^2\,\text{W}$	$\rightarrow$	Eddy current losses in stator conductors (Eq. 2.32)
$\Delta P_{fr} = 71.01\,\text{W}$	$\rightarrow$	Friction losses in bearings (Eq. 2.34)
$\Delta P_{wind} = 25.17\,\text{W}$	$\rightarrow$	Windage losses (Eq. 2.31)
$Re = 8.378 \cdot 10^5$	$\rightarrow$	Reynolds number (Eq. 2.36)
$\Delta P_{rot} = 96.18\,\text{W}$	$\rightarrow$	Total rotational losses (Eq. 2.37)

The motor's performance can be succinctly summarised through key parameters: the output power, represented by $P_{out} = 2.724 \cdot 10^5\,\text{W}$ (Eq. 2.38); the shaft torque, denoted as $T_{sh} = 867.023\,\text{Nm}$ (Eq. 2.39); the input power, quantified as $P_{in} = 2.838 \cdot 10^5\,\text{W}$ (Eq. 2.40); and the motor's efficiency, indicated as $\eta = 0.960$ (Eq. 2.41). These results are particularly noteworthy as they satisfy the stringent constraints set by the industrial partners of the PNRR project, requiring a minimum torque of $800.000\,\text{Nm}$ and an output power of $250.000\,\text{kW}$. This not only

underscores the motor's capability but also its efficiency in meeting these specified performance criteria.

$\lambda_{1e} = 0.150$	$\rightarrow$	End connection leakage flux (Eq. 2.42)
$\lambda_{1s} = 0.150$	$\rightarrow$	Differential leakage fluxes (Eq. 2.43)
$\lambda_{1d} = 0.002$	$\rightarrow$	(Eq. 2.44)
$\tau_{d1} = 0.011$	$\rightarrow$	Differential leakage factor (Eq. 2.45)
$g' = 0.038\,\text{mm}$	$\rightarrow$	Equivalent air gap in the d axis (Eq. 2.46)
$g'_q = 0.039\,\text{mm}$	$\rightarrow$	Equivalent air-gap in the q axis (Eq. 2.47)

Here are calculated values of reactances, which are electrical parameters reflecting the electrical response and operational characteristics of motors, helping to define the currents, voltages, and overall behaviour of such motors when powered by alternating voltage:

$X_1 = 1.304\,\Omega$	$\rightarrow$	Armature leakage reactance (Eq. 2.48)
$X_{ad} = 0.713\,\Omega$	$\rightarrow$	Armature reaction reactance on the d-axis (Eq. 2.50)
$X_{aq} = 0.695\,\Omega$	$\rightarrow$	Armature reaction reactance on the q-axis (Eq. 2.51)
$X_{sd} = 2.018\,\Omega$	$\rightarrow$	Synchronous reactance on the d-axis (Eq. 2.52)
$X_{sq} = 1.999\,\Omega$	$\rightarrow$	Synchronous reactance on the d-axis (Eq. 2.53)

Notable results within the system analysis include the input phase voltage, $V_1 = 853.760\,\text{V}$ (Eq. 2.54), which plays a pivotal role in motor operation. Additionally, the line-to-line voltage, $V_{1L-L} = 1.479{\cdot}10^3\,\text{V}$ (Eq. 2.55), is of paramount importance for evaluating electrical connections and power distribution within the motor system. The power factor, $cos\phi = 0.963o$ (Eq. 2.56), is noteworthy for its high value, signifying enhanced system efficiency by reducing reactive power and minimising losses.

$S_{PM} = 0.050\,\text{m}^2$	$\rightarrow$	Surface area of permanent magnets (Eq. 2.57)
$m_{PM} = 8.001\,\text{Kg}$	$\rightarrow$	Mass of all PMs (Eq. 2.58)
$m_{Fe} = 7.779\,\text{Kg}$	$\rightarrow$	Mass of backing steel discs (Eq. 2.59)
$J_{PM} = 0.220\,\text{Kgm}^2$	$\rightarrow$	PMs moment of inertia (Eq. 2.60)
$J_{Fe} = 0.156\,\text{Kgm}^2$	$\rightarrow$	Moment of inertia of the backing steel disc (Eq. 2.61)
$J_r = 0.376\,\text{kgm}^2$	$\rightarrow$	Moment of inertia of the rotor (Eq. 2.62)

Values of stator current:

$\delta = 15.62^\circ$	$\rightarrow$	Load angle (Eq. 2.63)
$I_{ashd} = 3.839 \cdot 10^2\,\text{A}$	$\rightarrow$	Stator current on the d-axis (Eq. 2.64)
$I_{ashq} = 1.691 \cdot 10^2\,\text{A}$	$\rightarrow$	stator current on the q-axis (Eq. 2.65)
$I_{ash} = 4.195 \cdot 10^2\,\text{A}$	$\rightarrow$	Stator current magnitude (Eq. 2.66)

It is crucial to examine a series of key values and parameters that directly influence the behaviour and performance of such systems, including electromagnetism, mechanical dynamics, and structural robustness:

$T_{dst} = 1.276 \cdot 10^3\,\text{Nm}$	$\rightarrow$	Electromagnetic starting torque (Eq. 2.67)
$n_0 = 1.562 \cdot 10^2\,\text{rev/s}$	$\rightarrow$	No load speed (Eq. 2.68)
$T_{mech} = 0.289\,\text{s}$	$\rightarrow$	Mechanical time constant (Eq. 2.69)
$L_{sd} = 3.211 \cdot 10^{-4}\,\text{H}$	$\rightarrow$	Synchronous inductance on the d axis (Eq. 2.70)
$L_{sq} = 3.182 \cdot 10^{-4}\,\text{H}$	$\rightarrow$	Synchronous inductance on the q axis (Eq. 2.71)
$T_{elm} = 0.001\,\text{s}$	$\rightarrow$	Electromagnetic time constant (Eq. 2.72)
$F_z = 6.987 \cdot 10^3\,\text{N}$	$\rightarrow$	Axial magnetic attractive force between steel discs (Eq. 2.73)
$p_z = 1.398 \cdot 10^5\,\text{Pa}$	$\rightarrow$	Magnetic pressure (Eq. 2.75)
$d_{Fe} = 0.006\,\text{m}$	$\rightarrow$	Backing steel disc thickness (Eq. 2.76)

Based on the provided values for F_z, p_z, and d_{Fe}, the outer diameter is sufficient to ensure the required stiffness of the disc under a 139.78 kPa magnetic pressure in the axial direction.
The result virtual prototype that need to be tested is represented in Figure 5.3, in the next chapter the values presented here will be tested to validate them.

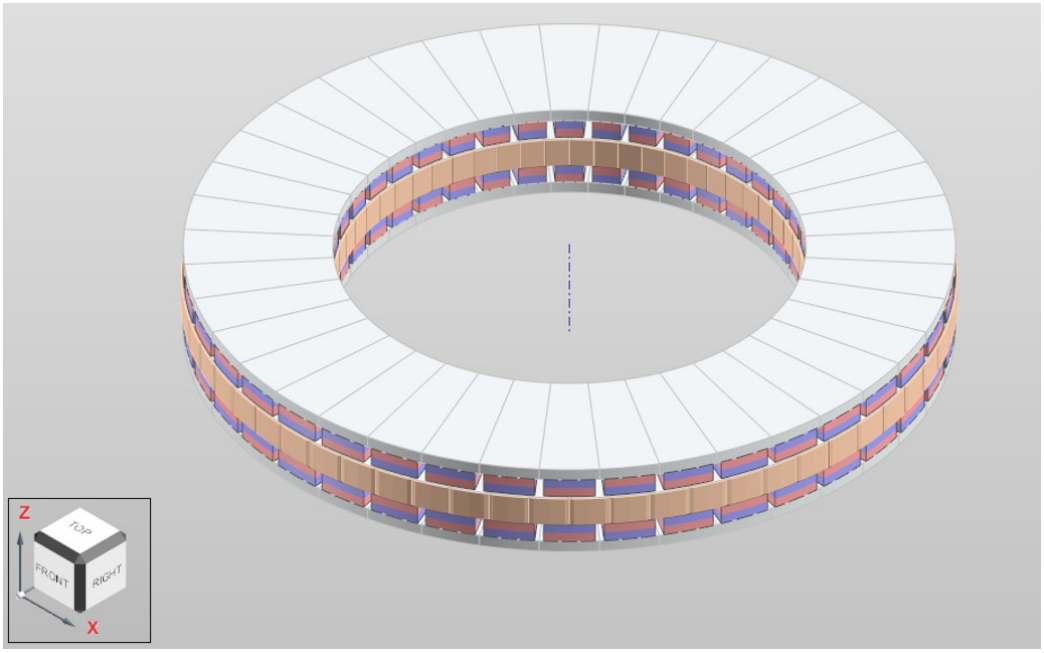

Figure 5.3: Virtual prototype of the developed axial flux machine model

5.3 Radial Flux Machine Model

The rules needed to build an electric machine prototype have already been studied in detail in the previous paragraph. In this section, a more specific case for radial flux machine is analysed, with a highlight on the case study of the Nissan Leaf motor. To attain the requisite design specifications, the designer initiates the process by carefully selecting appropriate values for the primary design parameters:

$$S = P_{out} k_w \overline{B} a_C D^2 L n \tag{5.3}$$

Where S represents the power rating of the electric motor (in Watts, W), K_w is the fundamental winding factor, $\overline{B}$ denotes the specific magnetic loading (in Tesla, T), a_c signifies the specific electrical loading (in Amperes per meter, A/m), D stands for the stator's inner diameter (in meters, m), L represents the active length of the machine (in meters, m) and n represents the rated speed (in revolutions per second rps).
The designer, guided by the chosen cooling strategy, proceeds to estimate values for magnetic and electrical loading. The selection of magnetic loading (B) hinges on the saturation point and core loss characteristics of the available materials, while the value of electrical loading (a_c) is contingent upon current density (δ) and the type of winding insulation materials in use. Both B and a_c values are derived from comprehensive data sources and the collective wisdom of designers.
Subsequent to the determination of specific magnetic and electrical loading, the designer calculates the ratio between the stator's inner diameter (D) and the machine's active length (L). At this juncture, the designer once again calls upon empirical curves and additional sizing equations to approximate a suitable number of pole-pairs (p) for the machine, enabling the calculation of the machine's aspect ratio (λ), as illustrated in the following equation:

$$\lambda = \frac{L}{\pi D p} \tag{5.4}$$

Nonetheless, the selection of the aspect ratio (λ) through Equation 5.3 may not be applicable in certain scenarios, particularly when compact machine dimensions and high power density are pivotal. Moreover, the determination of aspect ratio (λ) extends beyond the parameters employed in Equation 5.3, encompassing various machine variables, including material utilisation, required performance, manufacturing feasibility, and cooling considerations.
Following the selection of values for B, a_c, p, and λ, the designer must evaluate another critical factor: current density (J). In its simplest form, current density is defined as the amperes passing through a conductor divided by the cross-sectional area of the conductor, represented by $J = I/A_{wire}$. Elevating the current density leads to increased copper losses and, consequently, a rise in temperature. Excessive current density in an electric machine is a frequent cause of machine failure. When operating at rated current and high frequency, especially with a slender wire diameter, eddy currents tend to concentrate near the outer surface of the conductor, underneath the insulation. This can lead to localised heating, potentially causing insulation material degradation and bubbling. It is important to note that the recommended current density range of 5-7 A/mm^2 applies primarily to air-cooled systems and may not account for modern advancements, where current densities can sometimes extend up to 10 A/mm^2 for air-cooled systems and up to 28 A/mm^2 for liquid and gas-cooled systems.
The intricate nature of electric machine design poses a formidable and complex challenge. Electric machine design revolves around the careful consideration of factors such as machine weight, cost, volume, and efficiency. The optimisation problem inherent in electric machine design presents a multifaceted challenge, involving continuous and discrete variables from diverse realms of physics. These complexities render the objective functions nonlinear, lacking analytical expressions.
Over the past decade, an array of optimisation algorithms has been explored in the context of electric machine design. The primary objective of these investigations has been to identify an optimal optimisation method capable of delivering optimal solutions across the entire spectrum of design challenges. However, the "No Free Lunch Theorem" reminds us that if an algorithm excels in one problem class, it inevitably comes at the cost of reduced performance in other problem domains. Thus, there exists no universal algorithm perfectly suited for all optimisation tasks. Instead, an effective optimisation method is one that can systematically explore the search space and discover optimal solutions with minimal iterations.

Consequently, the principal challenge in employing design optimisation lies in the selection of an appropriate optimisation approach for a given problem.
In broad terms, an optimisation search procedure can be defined as the quest for a combination of independent variable parameters that maximise or minimise a given single or multi-objective function, often subject to certain constraints within defined parameter bounds.
Mathematically, the optimisation process can be outlined as follows:

- Commencing with the initial design parameter vector:

$$\overline{X_0} = [x_{01}, x_{02}, ..., x_{0D}], \overline{X_0} \in R^D \tag{5.5}$$

- Seeking the final design parameter vector:

$$\overline{X_m} = [x_{m1}, x_{m2}, ..., x_{mD}], \overline{X_m} \in R^D \tag{5.6}$$

- Ensuring that it satisfies the set of objective functions:

$$f(\overline{X_m}) = [f_1(\overline{X_m}), f_2(\overline{X_m}), ..., f_k(\overline{X_m})] \tag{5.7}$$

- Subject to the design constraints:

$$g_i(f_1(\overline{X_m})) \leq 0 for i = 1, 2, ..., n \tag{5.8}$$

- Where the design parameter bounds are defined as:

$$x_j^{(L)} \leq x_j \leq x_j^{(u)} for j = 1, 2, ..., D \tag{5.9}$$

Based on these search criteria, a variety of computational optimisation techniques need to be applied and refined to address engineering challenges.

5.3.1 The Developed Design

The construction and analysis of the radial flux machine model were performed using the Ansys MotorCAD software. To obtain meaningful results for comparison with the axial flux machine model, the Nissan Leaf motor underwent modifications to achieve a power output similar to that of the model.

RADIAL VIEW:
Stator Parameters:

Slot Number	=	48
Stator Lamination Diameter	=	$198\,mm$
Stator Bore	=	$132\,mm$
Tooth Width	=	$4.15\,mm$
Slot Depth	=	$21.1\,mm$
Slot Corner Radius	=	$2\,mm$
Tooth Tip Depth	=	$1.2\,mm$
Slot Opening	=	$2.814\,mm$
Tooth Tip Angle	=	$27°$
Sleeve Thickness	=	$0\,mm$

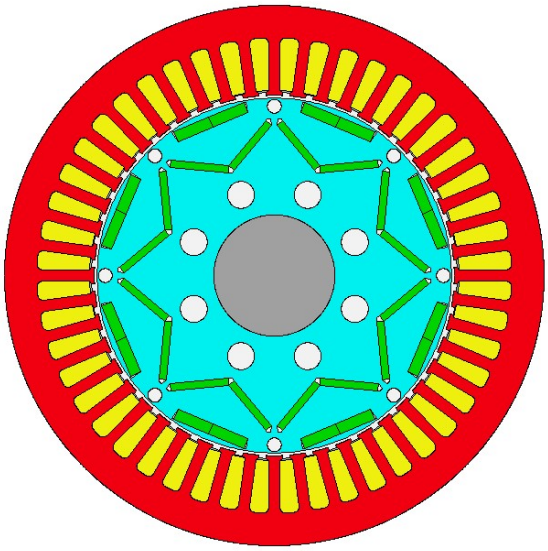

Figure 5.4: Radial view of the virtual prototype of the developed radial flux machine model

Rotor Parameters:

Pole Number	=	8	L2 Pole V Angle	=	124°
Notch Depth	=	0	L2 Pole Arc [ED]	=	159°
Magnet Layers	=	2	L2 Magnet Post	=	0
L1 Magnet Thickness	=	3.862 mm	L2 Magnet Separation	=	0 mm
L1 Magnet Bar Width	=	13.9 mm	L2 Magnet Segments	=	0
L1 Bridge Thickness	=	0.6 mm	L2 Mag Gap Inner	=	0 mm
L1 Web Thickness	=	21 mm	L2 Mag Gap Outer	=	0 mm
L1 Web Length	=	0 mm	air-gap	=	1 mm
L1 Pole V Angle	=	180°	Banding Thickness	=	0 mm
L1 Pole Arc [ED]	=	150°	Shaft Diameter	=	44.45 mm
L1 Magnet Post	=	0	Shaft Hole Diameter	=	0 mm
L1 Magnet Separation	=	0 mm	Rotor Duct Layers	=	2
L1 Magnet Segments	=	1	L1 RDuct Rad Diameter	=	63.94 mm
L1 Magnet Gap Inner	=	0 mm	L1 RDuct Channel	=	8
L1 Magnet Gap Outer	=	0 mm	L1 RDuct Diameter	=	9.88 mm
L2 Magnet Thickness	=	2.6 mm	L1 RDuct Angle	=	0°
L2 Magnet Bar Width	=	21.33 mm	L2 RDuct Rad Diameter	=	124 mm
L2 Bridge Thickness	=	7.65 mm	L2 RDuct Channel	=	8
L2 Web Thickness	=	2.5 mm	L2 RDuct Diameter	=	5.1 mm
L2 Web Length	=	0 mm	L2 RDuct Angle	=	22.5°

AXIAL VIEW:

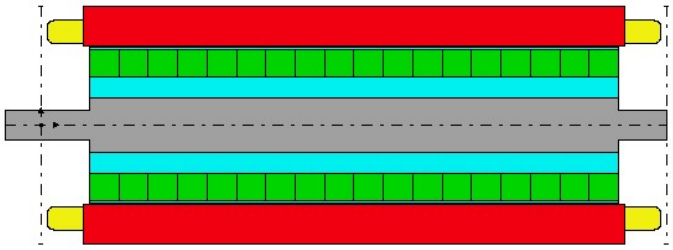

Figure 5.5: Axial view of the virtual prototype of the developed radial flux machine model

Radial dimensions:

Stator Lam Diameter	=	$198\,mm$
Stator Bore	=	$132\,mm$
air-gap	=	$1\,mm$
Banding Thickness	=	$0\,mm$
Sleeve Thickness	=	$0\,mm$
Shaft Diameter	=	$44.45\,mm$
Shaft Diameter [F]	=	$25\,mm$
Shaft Diameter [R]	=	$25\,mm$
Shaft Hole Diameter	=	$0\,mm$

Axial dimensions:

Motor Length	=	$520\,mm$
Stator Lam Length	=	$450\,mm$
Magnet Length	=	$440\,mm$
Magnet Segments	=	18
Rotor Lam Length	=	$440\,mm$
EWdg OH Mult [F]	=	1
EWdg OH Mult [R]	=	1
Wdg Extension [F]	=	$5\,mm$
Wdg Extension [R]	=	$5\,mm$
Shaft Extension [F]	=	$30\,mm$
Shaft Extension [R]	=	$0\,mm$

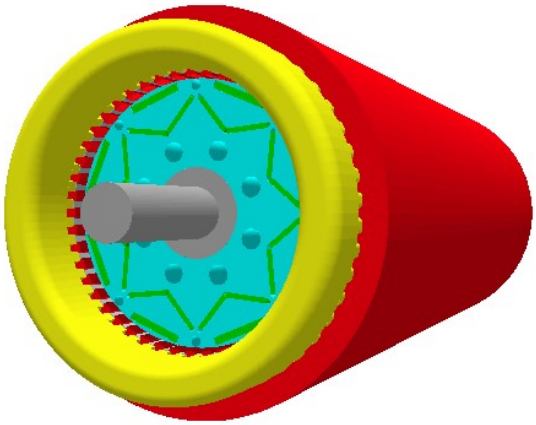

Figure 5.6: 3D virtual prototype of the developed radial flux machine model

WINDING CONFIGURATION:

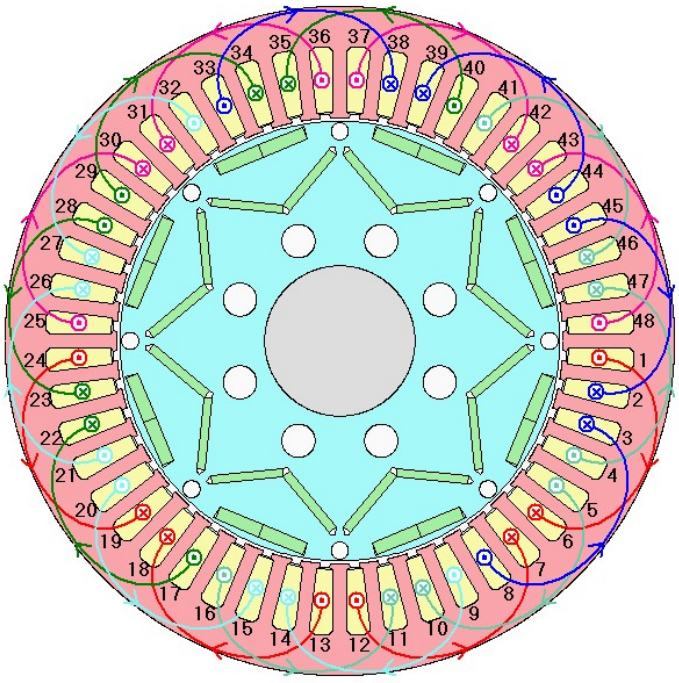

Figure 5.7: Winding configuration of the developed radial flux machine model

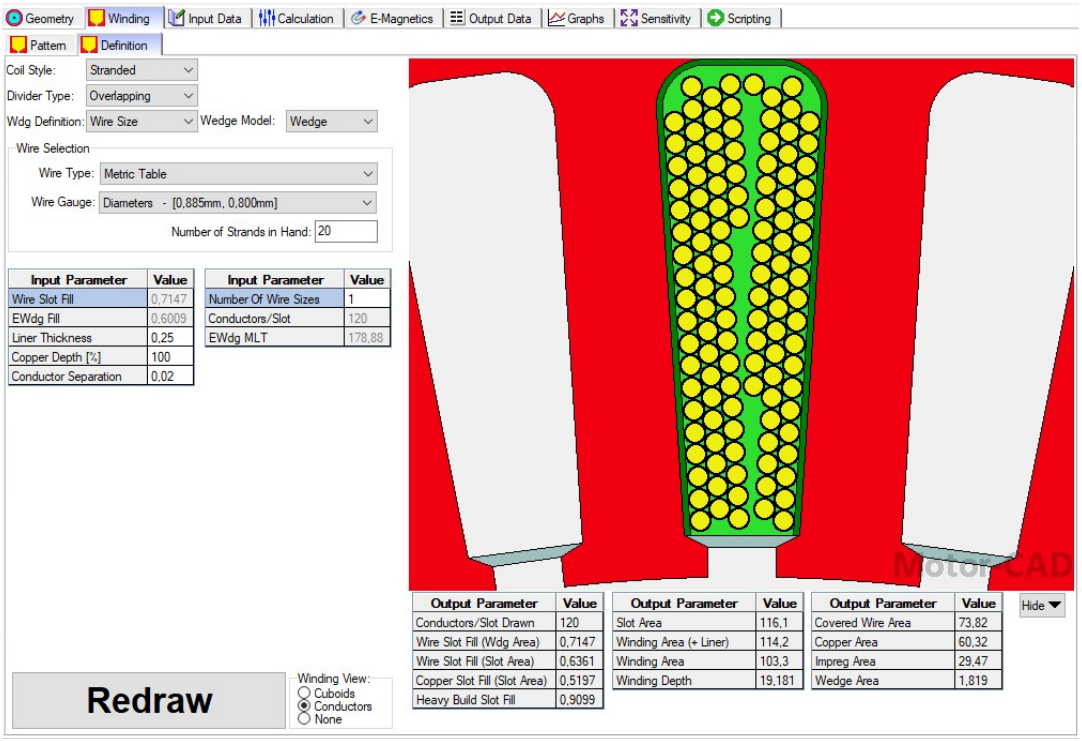

Figure 5.8: Winding wire selection of the developed radial flux machine model

5.4 Thermal Analysis and Cooling System

This paragraph will focus on the thermal machine model (built following the rules presented in Chapter 4) and on the project of a simplified cooling system, the highlight is made on the more interesting and less renowned axial flux machine case.

5.4.1 Thermal Equivalent Model

Recalling the case study of an axial flux permanent magnet machine with ironless stator and the parameters needed for thermal analysis: external and internal diameters $D_{out} = 0.4\,m$ and $D_{in} = 0.245\,m$, $\alpha_i = 0.6366$ magnet width-to-pole pitch ratio, $d = 0.0168m$ the rotor disc thickness (given by the sum of $h_M = 0.0105\,m$ and $d_{Fe} = 0.0063\,m$), $rpm = 3000$ rated speed in revolution per minute, rotational losses $\Delta P_{rot} = 96.1811W$, eddy current losses in the stator $\Delta P_e = 133.3519\,W$ and stator winding losses $\Delta P_{1w} = 1.1188 \cdot 10^4\,W$, the air density $\rho_{air} = 1.2\,Kg/m^3$, the dynamic viscosity of air $\mu_{air} = 1.8 \cdot 10^{-5}\,Pa \cdot s$ and $k = 0.0262\,W/(m°C)$ the thermal conductivity, $\nu = 1.5690 \cdot 10^{-5}\,m^2/s$ the kinematic viscosity of the fluid. The first challenge consists in evaluating steady state temperature of different parts of the machine. Starting from the evaluation of the convective heat transfer coefficient, it is possible to divide the motor in three different areas: outside rotor disc surface, rotor disc peripheral edge and rotor-stator system.

- **Outside rotor disc surface:**
  In analysing the thermal characteristics of various components within the system, the first step will be to examine the outer rotor disc surface. The Reynolds number at rated speed, denoted as Re, is determined by:

$$Re = \rho \frac{\Omega D_{out}^2}{4\mu} = 8.3776 \cdot 10^5 \tag{5.10}$$

  The transition between laminar and turbulent flow occurs at a critical radius (r_c), calculated as:

$$r_c = \sqrt{\frac{2.5 \cdot 10^5 \nu}{2\pi n_s}} = 0.1117\, m \tag{5.11}$$

  It is important to note that r_c must be smaller than half of the outer disc diameter ($D_{out}/2 = 0.2\, m$). The average Nusselt number ($\overline{Nu}$) for the disc surface is then evaluated using:

$$\overline{Nu} = 0.015 Re^{4/5} - 100(\frac{2r_c}{D_{out}})^2 = 790.2452 \tag{5.12}$$

  Subsequently, the average heat transfer coefficient at the outer surface of the disc ($\overline{h}_{fr}$) is determined as:

$$\overline{h}_{fr} = \frac{k}{D_{out}/2} \overline{Nu} = 103.6802\, W/(m^2\,^\circ C) \tag{5.13}$$

- **Rotor disc peripheral edge:**
  Moving on to the rotor disc peripheral edge, the Prandtl number (Pr) at atmospheric pressure ($Pr = 0.7$) has been utilised to compute the Reynolds number at the disc periphery (Re_D) as:

$$Re_D = \Omega \frac{D_{out}^2}{\nu} = 3.2037 \cdot 10^6 \tag{5.14}$$

  The average Nusselt number for this region is then expressed as:

$$\overline{Nu}_D = 0.133 Re_D^{2/3} Pr^{1/3} = 2.5663 \cdot 10^3 \tag{5.15}$$

  The average heat transfer coefficient around the radial periphery $\overline{h}_{rs}$:

$$\overline{h}_p = \frac{k}{D_{out}} \overline{Nu}_D = 168.3524\, W/(m^2\,^\circ C) \tag{5.16}$$

- **Rotor-stator system:**
  In the rotor-stator system, assuming equal flow on both sides of the stator and defining the equivalent flow rate as Q, the average Nusselt number ($\overline{Nu}$) is determined as:

$$\overline{Nu}_{rs} = 0.333 \frac{Q}{\pi \nu (D_{out}/2)} = 878.2431 \tag{5.17}$$

  the average heat transfer coefficient between the two discs ($\overline{h}_{rs}$) is found as:

$$\overline{h}_{rs} = \frac{2k}{D_{out}} \overline{Nu}_{rs} = 115.2255\, W/(m^2\,^\circ C) \tag{5.18}$$

Given the identified thermal characteristics, the thermal equivalent circuit can be addressed. The circuit takes into account the neglect of radiation from the rotor disc to the ambient, convection from the stator overhang to the airflow, and conduction resistance between magnets and the rotor. A simplified version of this circuit is employed to assess the steady-state temperatures of the system's various components (Figure 5.9):

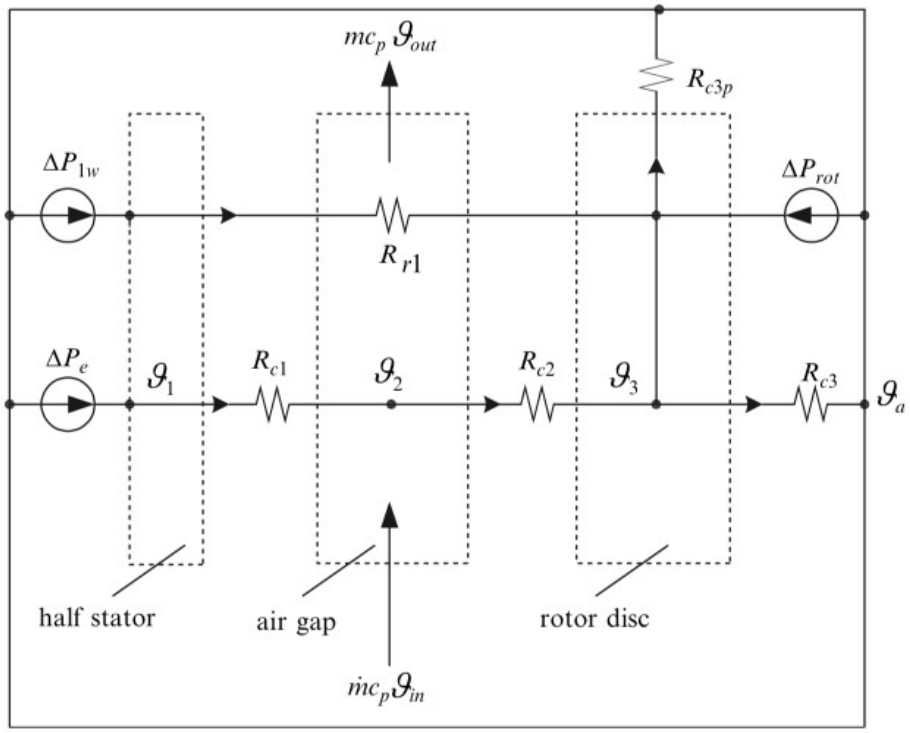

Figure 5.9: Simplified thermal equivalent circuit. Source: [61]

- **Half of the stator:**
  Starting with half of the stator, the convection heat transfer resistance between the stator and the airflow within the air gap is computed as R_{c1}:

$$R_{c1} = \frac{1}{\overline{h}_{rs}\frac{\pi}{4}(D_{out}^2 - D_{in}^2)} = 0.1105\,\Omega \tag{5.19}$$

  The radiation heat transfer resistance between the stator and rotor discs R_{r1}:

$$R_{r1} = \frac{\frac{1-\epsilon_1}{\epsilon_1 A_1} + \frac{1}{A_1 F_{12}} + \frac{1-\epsilon_2}{\epsilon_2 A_2}}{\sigma[(\theta_1+273)+(\theta_2+273)][(\theta_1+273)^2+(\theta_2+273)^2]} \tag{5.20}$$

  in which the areas of both discs can be taken as the same, i.e. $A_1 = A_2 = \pi(D_{out}^2 - D_{in}^2) = 0.0785\,m^2$, the shape factor $F = 1$, the Stefan-Boltzmann constant $\sigma = 5.67 \cdot 10^{-8}\,W/(m^2K^4)$, the emissivity of epoxy encapsulated stator $\epsilon_1 = 0.85$. Since part of the rotor disc is covered with PMs, the emissivity of the rotor disc is defined based on the proportion of different materials, i.e.:

$$\epsilon_2 = \epsilon_{fe}\alpha_i + \epsilon_{pm}(1-\alpha_i) = 0.518 \tag{5.21}$$

An iterative approach is employed to solve for R_{r1} over a range of temperatures.
The conservation of energy is expressed in the steady-state energy equation for control volume 1:

$$\frac{1}{2}(\Delta P_{1w} + \Delta P_e) - \frac{(\theta_1 - \theta_2)}{R_{c1}} - \frac{(\theta_1 - \theta_3)}{R_{r1}} = 0 \tag{5.22}$$

- **Air gap:**
  Moving to the air gap, the convection heat transfer resistance from the air gap to the rotor disc (R_{c2}) is approximated to be the same as R_{c1}. The mass flow rate (mm) is computed as ρQ. The steady-state energy equation for control volume 2 is described as follows: Assuming the air temperature at the machine inlet as ambient temperature ($\theta_{in} = \theta_a$) and the air gap average temperature as: $\theta_2 = \frac{1}{2}(\theta_{out} + \theta_{in})$; the steady-state energy equation for control volume 2 is:

$$\frac{\theta_1 - \theta_2}{R_{c1}} - \frac{\theta_2 - \theta_3}{R_{c2}} - 2\dot{m}c_p(\theta_2 - \theta_a) = 0 \tag{5.23}$$

- **Rotor disc:**
  For the rotor disc, the convection heat transfer resistance at the outer surface of the disc (R_{c3}):

$$R_{c3} = \frac{4}{\overline{h}_{fr}\pi D_{out}^2} = 0.0768\,\Omega \tag{5.24}$$

  and at the periphery of the disc (R_{c3p}):

$$R_{c3p} = \frac{1}{\overline{h}_p \pi D_{out} d} = 0.2807\,\Omega \tag{5.25}$$

  The steady-state energy equation for control volume 3 is expressed as:

$$\frac{\theta_2 - \theta_3}{R_{c2}} + \frac{\theta_1 - \theta_3}{R_{r1}} + \frac{1}{2}\Delta P_{rot} - \frac{\theta_3 - \theta_a}{R_{c3}} - \frac{\theta_3 - \theta_a}{R_{c3p}} = 0 \tag{5.26}$$

The equations 5.22, 5.23 and 5.26 have been established to represent the energy balance for each part of the machine. To determine the steady-state temperatures, these equations are solved. Notably, since R_{r1} exhibits temperature dependency, a simple computer program utilising Gauss-Seidel iteration has been developed to obtain solutions for these equations. The results of the system are: $R_{r1} = 0.4298\,\Omega$, $t_1 = 594.6707°C$ which represents the temperature of the stator winding, $t_2 = 96.8858°C$ which is the air-gap flow temperature and $t_3 = 97.3698°C$ that is the rotor disc temperature.

5.4.2 Cooling System Design

In addressing the thermal management of the system, a particular focus is placed on the stator, which is known to operate at higher temperatures. To accomplish this, heat pipes are employed for the direct cooling of the motor, as depicted in Figure 4.4. Convection heat transfer coefficients on the inner surfaces of the heat pipes within the stator and the finned area are considered as $h = 1000\,W/(m^2\,°C)$. Additionally, parameters such as the average convective heat transfer coefficient on the fin surfaces ($h_{fin} = 50\,W/(m^2\,°C)$), the finned area ($A_{fin} = 1.8\,m^2$), the efficiency ($\eta_{fin} = 0.92$), and the length of the heat pipes embedded in the finned surface ($l_{fin} = 1.5\,m$) are taken into account.

The primary objective is to minimise the steady-state temperature of the stator by utilising a heat pipe positioned along the stator's average radius with a designated diameter ($D_{hp} = 0.025\,m$). It is assumed that the outer wall of the heat pipe maintains full contact with both the stator winding and the finned surface. Consequently, the exposed area of the heat pipe within the stator (A_{hot}) and within the finned surface (A_{cold}) are calculated:

$$A_{hot} = \pi D_{hp} \frac{\pi(D_{out} + D_{in})}{2} = 0.0796\,m^2 \tag{5.27}$$

$$A_{cold} = \pi D_{hp} l_{fin} = 0.1178\,m^2 \tag{5.28}$$

In evaluating the cooling system's effectiveness, the highest temperature among various parts of the system, taking into account the results of three specific equations (5.22, 5.23 and 5.26) is identified. After the implementation of the cooling system, the final temperature, denoted as θ_{cold}, representing the stator's steady-state temperature, is determined as:

$$\theta_{cold} = \theta_{stator} - \Delta P_{hp}\left(\frac{1}{h_{hot}A_{hot}} + \frac{1}{h_{cold}A_{cold}} + \frac{1}{\eta_{fin}h_{fin}A_{fin}}\right) = 219.5616^{\circ}C \tag{5.29}$$

Shifting the focus to an alternative scenario, the consequences of replacing the heat pipe with a liquid cooling pipe has been explored. This liquid cooling pipe, with a specific diameter ($d = 0.025\,m$) through which a liquid flows at a velocity ($v_{liquid} = 0.5\,m/s$), introduces variations in properties such as density (ρ), specific heat constant (c_p), dynamic viscosity (μ), and thermal conductivity (k) for different types of liquids at different temperatures.

The chosen liquid for this scope is the DOWTHERM™ SR-1 Fluid at different percentage of concentration by volume of ethylene glycol, the values of specific heat, density, thermal conduction and viscosity change with temperature and concentration of the liquid (Figure 5.10, 5.11 and 5.12)

Saturation Properties of DOWTHERM SR-1 Fluid at 30% Ethylene Glycol Concentration by Volume

Temperature °C	(°F)	Specific Heat kJ/(kg)(K) (Btu/lb. °F)		Density kg/m³ (lb./ft.³)		Therm. Cond. W/mK [Btu/hr. ft.² (°F/ft.)]		Viscosity mPa•s (cps)	
-10	(14)	3.562	(0.851)	1055.47	(65.89)	0.4154	(0.2400)	6.1788	(6.18)
10	(50)	3.619	(0.865)	1049.91	(65.54)	0.4420	(0.2554)	2.9482	(2.95)
40	(104)	3.704	(0.885)	1037.92	(64.80)	0.4731	(0.2733)	1.3398	(1.34)
65	(149)	3.775	(0.902)	1024.59	(63.96)	0.4909	(0.2836)	0.8246	(0.82)
90	(194)	3.846	(0.919)	1008.20	(62.94)	0.5015	(0.2897)	0.5599	(0.56)
120	(248)	3.931	(0.939)	984.53	(61.46)	0.5044	(0.2915)	0.5044	(0.38)

Figure 5.10: Properties of DOWTHERM™ SR-1 Fluid at 30% Ethylene Glycol Concentration by Volume. Source: [68]

Saturation Properties of DOWTHERM SR-1 Fluid at 40% Ethylene Glycol Concentration by Volume

Temperature °C	Temperature (°F)	Specific Heat kJ/(kg)(K) (Btu/lb. °F)		Density kg/m³ (lb./ft.³)		Therm. Cond. W/mK [Btu/hr. ft.² (°F/ft.)]		Viscosity mPa•s (cps)	
-20	(-4)	3.336	(0.797)	1073.23	(67.00)	0.3707	(0.2142)	15.7533	(15.75)
10	(50)	3.436	(0.821)	1064.73	(66.47)	0.4053	(0.2342)	4.0451	(4.05)
40	(104)	3.537	(0.845)	1051.85	(65.66)	0.4312	(0.2491)	1.7731	(1.77)
65	(149)	3.621	(0.865)	1037.76	(64.79)	0.4462	(0.2578)	1.0646	(1.06)
90	(194)	3.705	(0.885)	1020.63	(63.72)	0.4552	(0.2630)	0.7013	(0.70)
120	(248)	3.805	(0.909)	996.06	(62.18)	0.4582	(0.2647)	0.4614	(0.46)

Figure 5.11: Properties of DOWTHERM™ SR-1 Fluid at 40% ethylene glycol concentration by Volume. Source: [68]

Saturation Properties of DOWTHERM SR-1 Fluid at 50% Ethylene Glycol Concentration by Volume

Temperature °C	Temperature (°F)	Specific Heat kJ/(kg)(K) (Btu/lb. °F)		Density kg/m³ (lb./ft.³)		Therm. Cond. W/mK [Btu/hr. ft.² (°F/ft.)]		Viscosity mPa•s (cps)	
-30	(-22)	3.090	(0.739)	1090.31	(68.07)	0.3333	(0.1926)	43.9970	(44.0)
-20	(-4)	3.129	(0.748)	1088.15	(67.93)	0.3442	(0.1989)	22.0816	(22.08)
10	(50)	3.245	(0.776)	1078.72	(67.34)	0.3724	(0.2152)	5.5071	(5.51)
40	(104)	3.361	(0.803)	1064.91	(66.48)	0.3937	(0.2275)	2.2567	(2.26)
65	(149)	3.457	(0.826)	1050.05	(65.55)	0.4062	(0.2347)	1.2936	(1.29)
90	(194)	3.554	(0.849)	1032.15	(64.44)	0.4139	(0.2391)	0.8227	(0.82)
120	(248)	3.670	(0.877)	1006.66	(62.84)	0.4168	(0.2408)	0.5252	(0.53)

Figure 5.12: Properties of DOWTHERM™ SR-1 Fluid at 50% Ethylene Glycol Concentration by Volume. Source: [68]

Transitioning to liquid cooling entails the assessment of critical dimensionless parameters. The Prandtl number (Pr) is computed, taking into consideration the properties mentioned earlier:

$$Pr = \frac{\mu c_p}{k} \tag{5.30}$$

Furthermore, the Reynolds number (Re_d) is evaluated, considering density (ρ), liquid velocity (v_{liquid}), and diameter (d):

$$Re_d = \frac{\rho v_{liquid} d}{2\mu} \tag{5.31}$$

For both the heating and cooling phases of the liquid within the pipe, the Nusselt number (Nu) is determined. Nu_{dh} pertains to the heating phase, while Nu_{dc} relates to the cooling phase, and they are calculated as follows:

$$Nu_{dh} = 0.023 Re_d^{0.8} Pr^{0.4} \tag{5.32}$$

$$Nu_{dc} = 0.023 Re_d^{0.8} Pr^{0.3} \tag{5.33}$$

The convection heat transfer coefficients for the water pipe within the stator (h_{hot}) and in the finned area (h_{cold}) are subsequently computed based on the Nusselt numbers and diameter d:

$$h_{hot} = \frac{k Nu_{dh}}{d} \tag{5.34}$$

$$h_{hot} = \frac{kNu_{dc}}{d} \tag{5.35}$$

With these parameters established, the steady-state temperature within the stator can be calculated, following the methodology discussed earlier in 5.29. This evaluation provides valuable insights into the implications of substituting heat pipes with liquid cooling pipes. The table (Table 5.2) collects the results of the estimated stator temperatures under the cooling system with DOWTHERM™ SR-1 fluid at various concentrations of ethylene glycol by volume and different temperatures:

Liquid temperature	Ethylene glycol 30%	Ethylene glycol 40%	Ethylene glycol 50%
40°C	191.0731°C	135.0048°C	73.2901°C
65°C	247.2662°C	205.7455°C	163.6017°C
90°C	281.8848°C	250.1117°C	219.3227°C
120°C	288.5876°C	284.3707°C	261.6834°C

Table 5.2: Results of stator temperatures in different conditions

From the results, it can be observed that an appropriate choice might be to use the 40% concentration liquid to maintain the stator at an adequate temperature within the 40-65°C range.

Chapter 6

Validation of Sizing Results

In this chapter, the focus is placed on the critical process of validating selected parameters for a motor through finite element analysis (FEA). The utilisation of computational methods to assess and confirm the chosen values for the motor represents a pivotal step in ensuring the accuracy and reliability of its design. The fundamental objective of this chapter is to rigorously evaluate the chosen values for essential motor parameters, ensuring that they conform with the desired design objectives and meet the stringent standards of performance and reliability.

6.1 Finite Element Analysis Method

Finite Element Analysis (FEA) is a computational technique used to analyse and simulate the behaviour of complex structures and systems by dividing them into smaller, interconnected elements. It is widely employed in engineering and design to assess various physical phenomena, including stress distribution, heat transfer, and electromagnetic fields. FEA provides valuable insights into the performance, safety, and efficiency of components or systems under various conditions.
When it comes to validating parameters of a motor using FEA, the process typically involves the following steps:

1. **Model Creation:** An accurate 3D model of the motor is created using specialised software. This model should represent the physical geometry and characteristics of the motor, including its materials, dimensions, and components.

2. **Mesh Generation:** The motor model is divided into a mesh of small, interconnected elements. These elements can be triangles, quadrilaterals, tetrahedra, or other shapes, depending on the analysis requirements. The more elements in the mesh, the more precise the analysis, but it also requires more computational resources.

3. **Material Properties:** The properties of the motor's materials, such as conductivity, thermal expansion coefficients, and magnetic permeability, are defined within the FEA software.

4. **Boundary Conditions:** Boundary conditions are set to simulate real-world operating conditions. For a motor, this might include specifying fixed points, applying loads, or defining temperature boundaries.

5. **Solver Execution:** The FEA software solves a set of mathematical equations that describe the physical behaviour of the motor under the specified conditions. These equations consider factors like stress, strain, temperature distribution, and electromagnetic fields.

6. **Analysis of the Results:** Once the solver has completed its calculations, the FEA software provides a wealth of information, including stress distribution, temperature profiles, magnetic field strengths, and other relevant parameters.

7. **Validation:** The analysis results are compared to the desired parameters for the motor. If the results align with the intended design goals, it validates the chosen values for the motor's parameters. If discrepancies are found, adjustments may be made to optimise the motor's design.

8. **Iterative Process:** FEA allows for an iterative approach to refining the motor's design. Engineers can make changes to the motor's parameters and rerun the analysis until the desired performance and safety criteria are met.

FEA is an indispensable tool for motor design and optimisation, as it helps ensure that the selected parameters, such as materials, dimensions, and electromagnetic properties, lead to a motor that performs as expected and meets safety and efficiency standards. This process of validation through FEA contributes to more robust and reliable motor designs, reducing the need for costly physical prototypes and testing.

In the following sections, an examination of the results from three distinct FEA analyses will be undertaken. The first analysis focuses on the validation of parameters for the axial flux motor, shedding light on the electromagnetic and mechanical aspects of its design. The second analysis centres on the validation of values for a radial flux motor. Finally, an exploration of the outcomes of an FEA analysis devoted to the assessment of thermal performance and cooling strategies for both axial and radial flux motors will be conducted. These results will collectively contribute to a comprehensive understanding of the motors behaviour and inform critical decisions regarding their design and operation.

6.2 Validation of the Axial Flux Machine Model

The validation of the axial flux motor was carried out using a rigorous approach involving two distinct software tools, Ansys Maxwell and MotorXP, in order to achieve a double-check of the results. Both of these software programs are widely recognised in the field of finite element analysis, but they exhibit significant differences in their implementation and capabilities. Ansys Maxwell is known for its power and versatility in handling complex electromagnetic analyses and simulations, offering a wide range of customisable options and advanced tools for optimising designs. On the other hand, MotorXP excels in the specific domain of electric motors, providing specialised tools for analysing electromagnetic flows in axial flux motors, ensuring greater precision in results. This combination of expertise and resources proved essential for accurate and comprehensive validation of our axial flux motor, allowing for a detailed assessment of device performance and efficiency.

6.2.1 Ansys Maxwell

Ansys Maxwell serves as an electromagnetic field solver designed for a wide range of applications, including electric machines, transformers, wireless charging systems, permanent magnet latches, actuators, and various electric mechanical devices. It is proficient in solving static, frequency-domain, and time-varying magnetic and electric fields, offering specialised design interfaces tailored to electric machines and power converters.

Through Maxwell, the precise characterisation of nonlinear and transient motion in electromechanical components, along with their impacts on drive circuitry and control system design, can be achieved. This software leverages advanced electromagnetic field solvers and seamlessly integrates them with integrated circuit and systems simulation technology, facilitating an in-depth understanding of the performance of electromechanical systems long before physical hardware prototyping becomes necessary.

The analysis using Ansys Maxwell was conducted with two different input currents to validate the results. First, an input current with an RMS value of 115 A and three currents out of phase by 120° were employed (Figure 6.1). Subsequently, a constant input current with a net zero sum was used for the second part of the analysis.

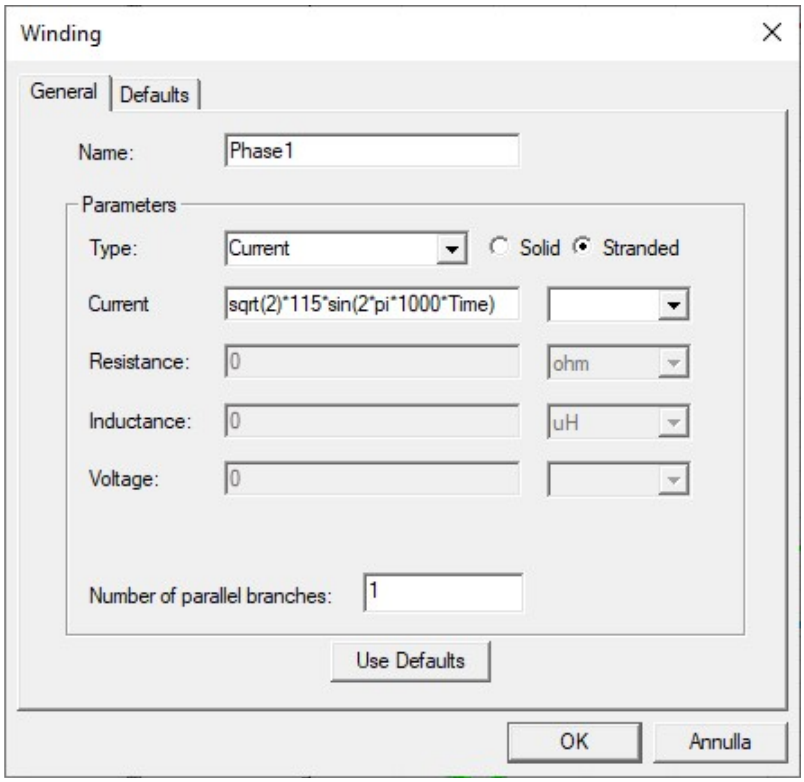

Figure 6.1: Input current for phase 1. The input currents for phases 2 and 3 are respectively: $\sqrt{2}\ 115 \sin\left(2\pi 1000\ t - 2\pi/3\right)$ and $\sqrt{2}\ 115 \sin\left(2\pi 1000\ t + 2\pi/3\right)$, with t = Time

To verify the accuracy of the induced phase voltages and input phase current, they have been plotted in Figure 6.2 and Figure 6.3.

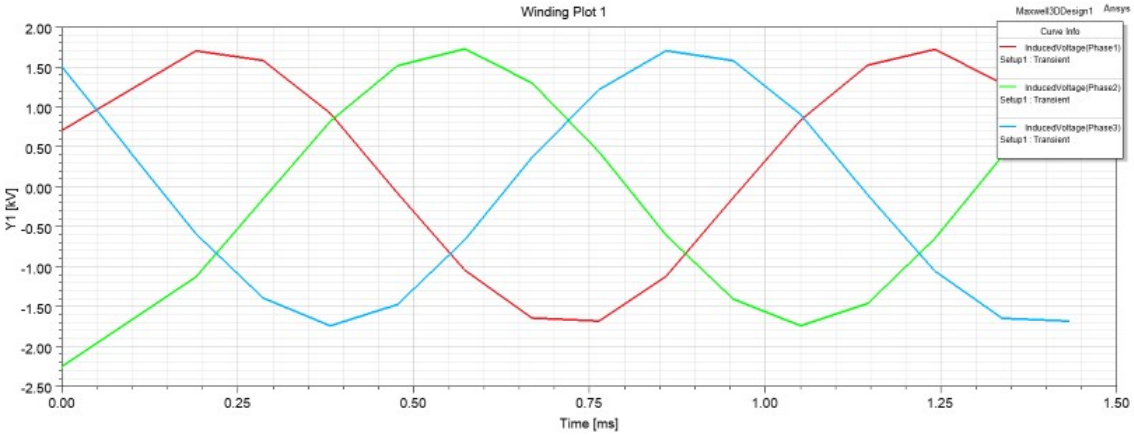

Figure 6.2: Induced phase voltages. Peak value $\simeq$ 1.70kV

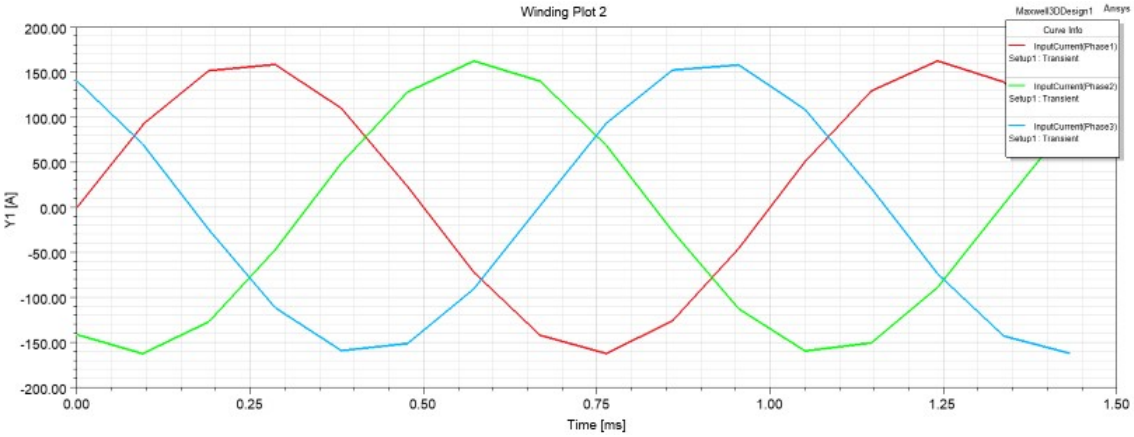

Figure 6.3: Input phase currents. Peak value $\simeq$ 1.60A

Focusing then on the output torque value of Figure 6.4, the observed value is indeed higher than the one simulated in Chapter 5.2.1, but this difference can also be attributed to the initial phase misalignment between the rotor and stator, which are not perfectly aligned in the 3D model. Hence, this variation in the results is reasonable and can be attributed to the inherent misalignment between these components.

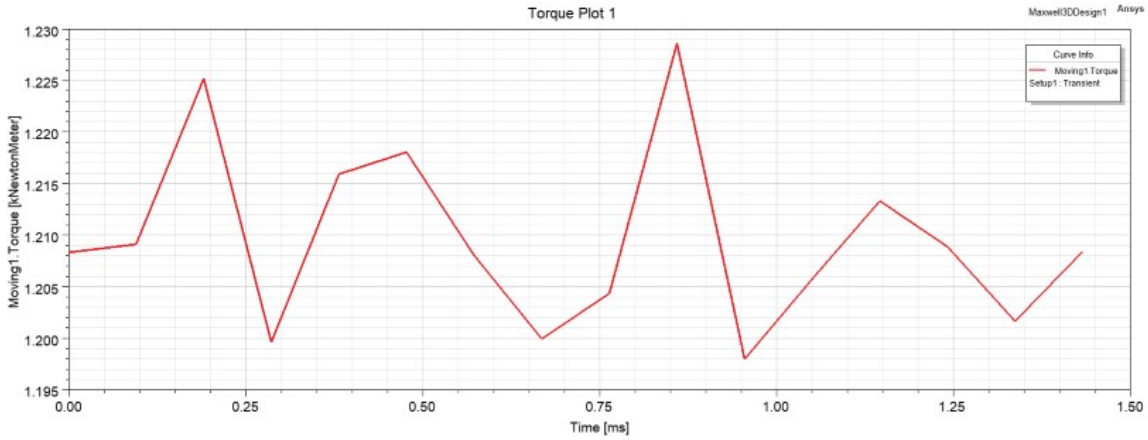

Figure 6.4: Output torque plot. Average value $\simeq$ 1.210kNm

Moving to simulations with constant currents as input (as depicted in Figure 6.5), the phase currents for Phase 1, Phase 2, and Phase 3 are, respectively, $\sqrt{2}115$ A, $-\sqrt{2}115$ A, and $-\sqrt{2}115$ A.

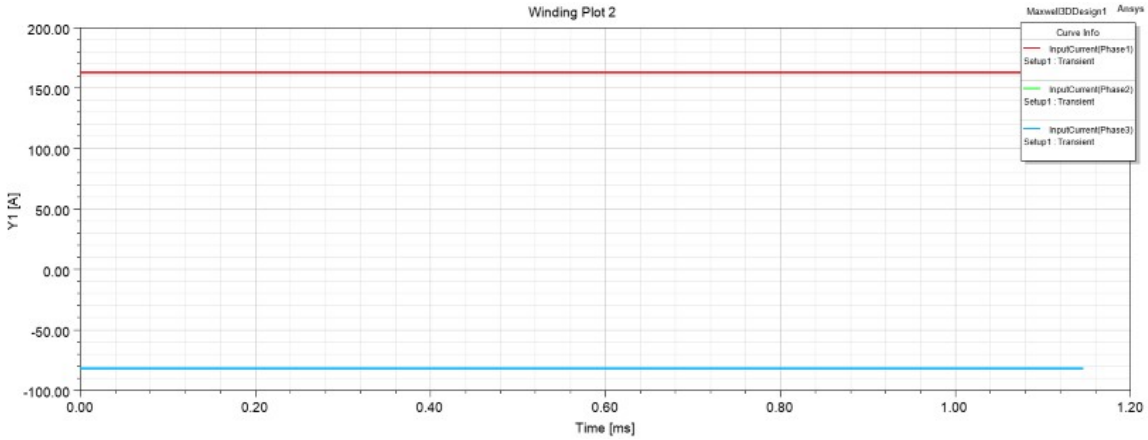

Figure 6.5: Constant input phase currents. $I_a = 115\sqrt{2}$ A, $I_b = -\sqrt{2}115$ A, $I_c = -\sqrt{2}115$ A

As it could have been expected, the phase voltage (Figure 6.6) corresponds to the one of the previous scenario.

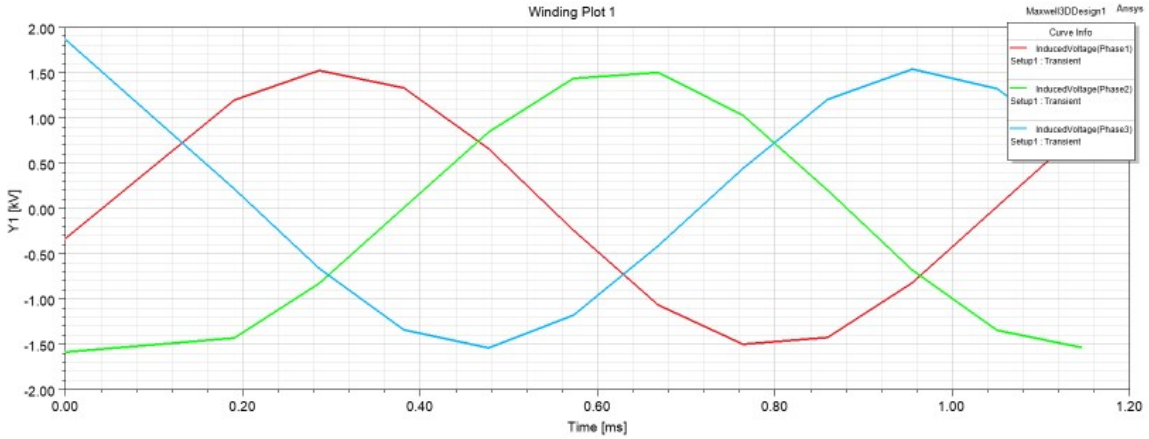

Figure 6.6: Induced phase voltages plot with constant input currents. Peak value $\simeq$ 1.70kV

Clearly, with a constant input, the average torque value will be zero (Figure 6.7). The interesting point to focus on is that the peak value is 1200 Nm, which is the same as the average value obtained in the case of a sinusoidal input. This confirms the reliability of the simulation.

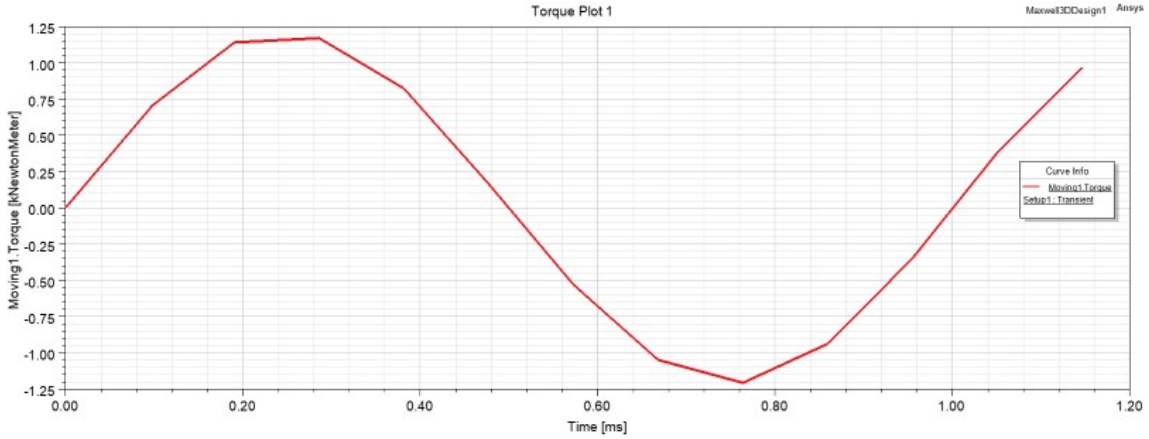

Figure 6.7: Output torque plot with constant input currents. Peak value $\simeq$ 1.210kNm

6.2.2 MotorXP-AFM

MotorXP-AFM stands out as the sole software presently accessible in the market exclusively dedicated to the electromagnetic design and evaluation of axial flux machines (AFM) featuring permanent magnets, encompassing brushless DC and permanent magnet synchronous motors and generators. Its distinctive quasi-3D finite element modelling approach revolutionises AFM design by delivering computational speeds up to ten times faster than full 3-D FEA, all while maintaining the highest level of precision. MotorXP-AFM boasts a range of analysis types, integrating a combination of FEA and analytical methods, providing over a hundred output parameters, built-in and customisable geometry templates, a versatile material library, as well as parametric analysis and optimisation API, establishing a flexible and robust e-machine design workflow. MotorXP-AFM is accessible both as a MATLAB-based application and as a standalone program that operates independently of MATLAB.

In this case, when providing the RMS value of the current and the rated mechanical speed as input (Figure 6.8), the analysis yields torque results very similar to those obtained with Ansys Maxwell. As mentioned earlier, the deviation in the results is attributed to a different alignment between the stator and rotor.

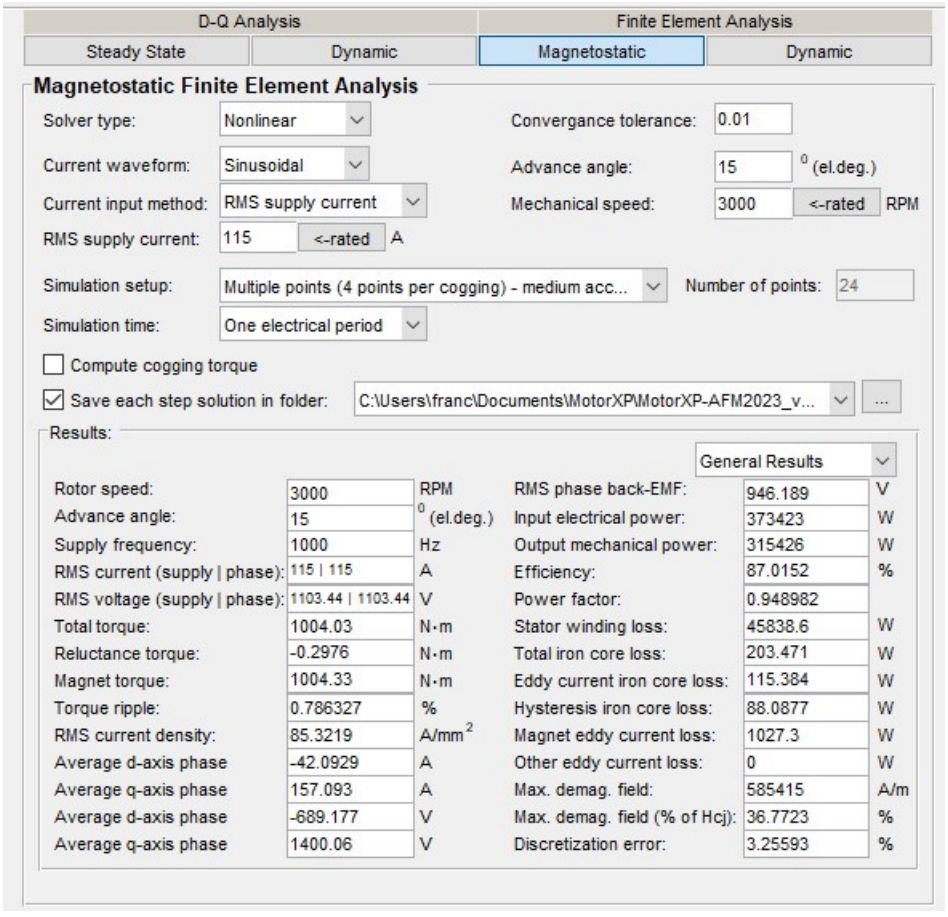

Figure 6.8: Input values for MotorXP simulation

MotorXP allows for the plotting of a wider range of results compared to Ansys Maxwell. Notable results are presented below:

Current:

Firstly, to check the correctness of the analysis, it is essential to check the input current (6.9):

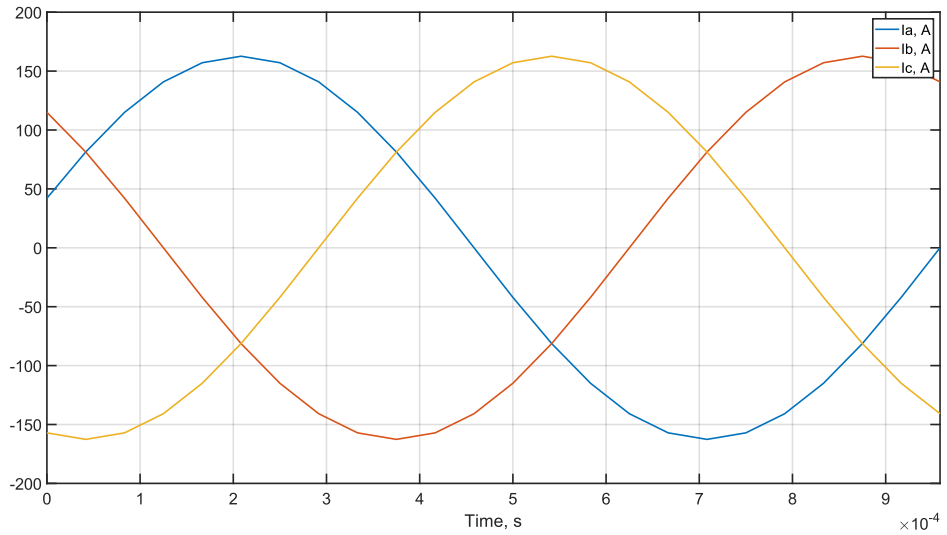

Figure 6.9: Phase currents. Peak value $\simeq$ 1.60A

And the **induced phase voltage:**

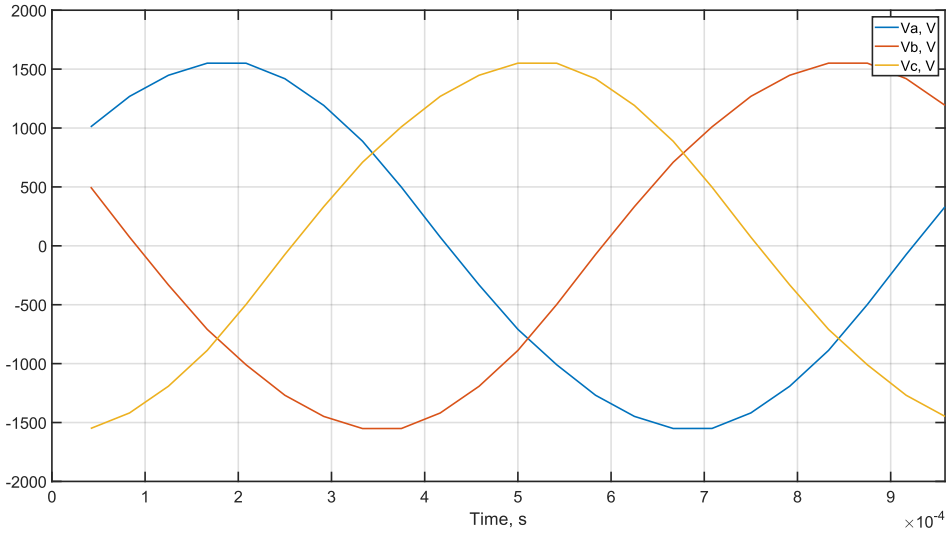

Figure 6.10: Phase voltages. Peak value $\simeq$ 1.70kV

Magnetostatic Flux Density:
Magnetostatic Flux Density (Bm), it represents the distribution of the magnetostatic flux within a system and is used to describe the magnetic field in that system. The associated Figure 6.11 in the analysis results visually shows how the magnetic field is distributed within the studied system.

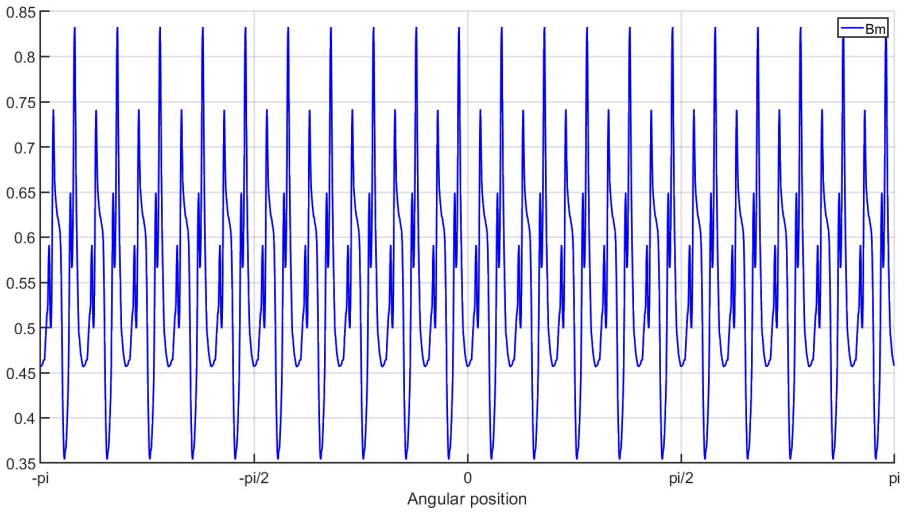

Figure 6.11: Magnetostatic analysis: Bm. Average value $\simeq$ 0.55T

It is intriguing to also examine the 2D sectional view plot for the magnetic flux density, as depicted in Figure 6.12:

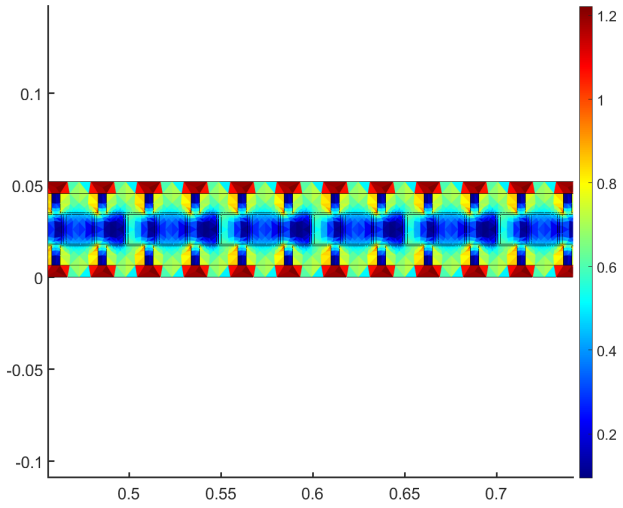

Figure 6.12: Magnetic flux density 2D

Magnet Torque:
The output torque generated by the magnets is depicted in Figure 6.13, and, as mentioned earlier, this value confirms the accuracy of the estimated torque.

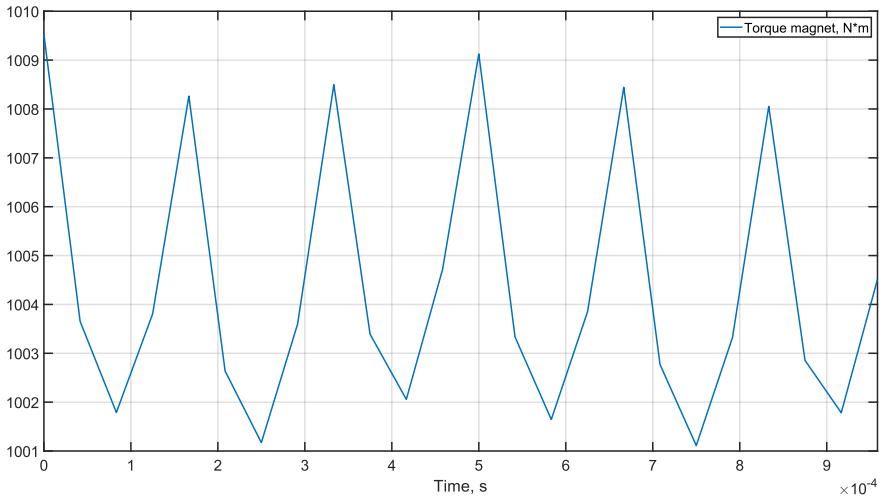

Figure 6.13: Magnet torque. Average value $\simeq$ 1005Nm

Reluctance Torque:
The reluctance torque (Figure 6.14) is anticipated to remain relatively low due to its primary sensitivity to axial alignment. This alignment exerts a more significant influence on the torque produced by the magnets, as they seek a more direct alignment in contrast to the variable reluctance between the d and q axes.

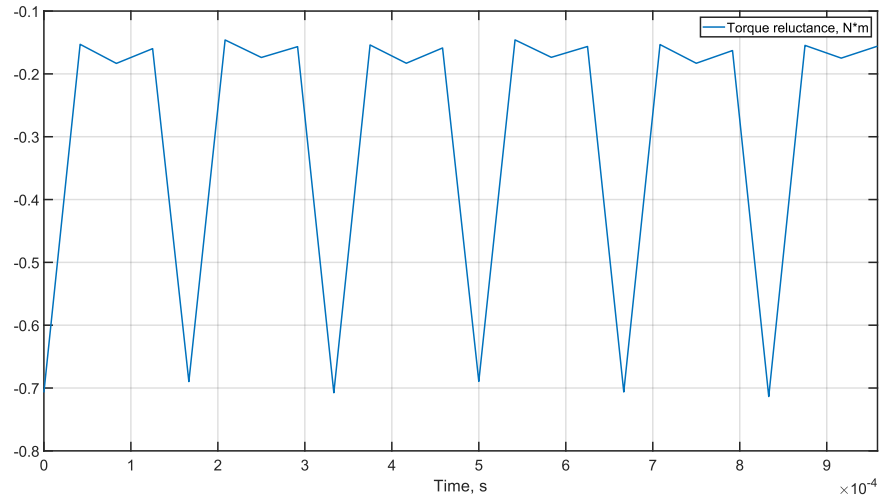

Figure 6.14: Torque produced by the presence of reluctance. Average value $\simeq$ -0.35Nm

6.3 Validation of the Radial Flux Machine Model

The validation process for the radial flux machine model has been developed with the Ansys software Motor-CAD. Motor-CAD empowers design engineers to assess a wide spectrum of motor topologies and concepts, encompassing the entire operational range, in order to generate designs that are finely tuned for superior performance, efficiency, and compactness. This comprehensive software comprises four interconnected modules – EMag, Therm, Lab, Mech – facilitating rapid and iterative multiphysics simulations. This streamlined approach accelerates the journey from initial concept to the ultimate design, significantly reducing the time required for this process. Once the geometric and winding configuration are complete and the materials have been selected correctly, it is possible to move to the calculation tab where it is possible to set operational characteristics (Figure 6.15).

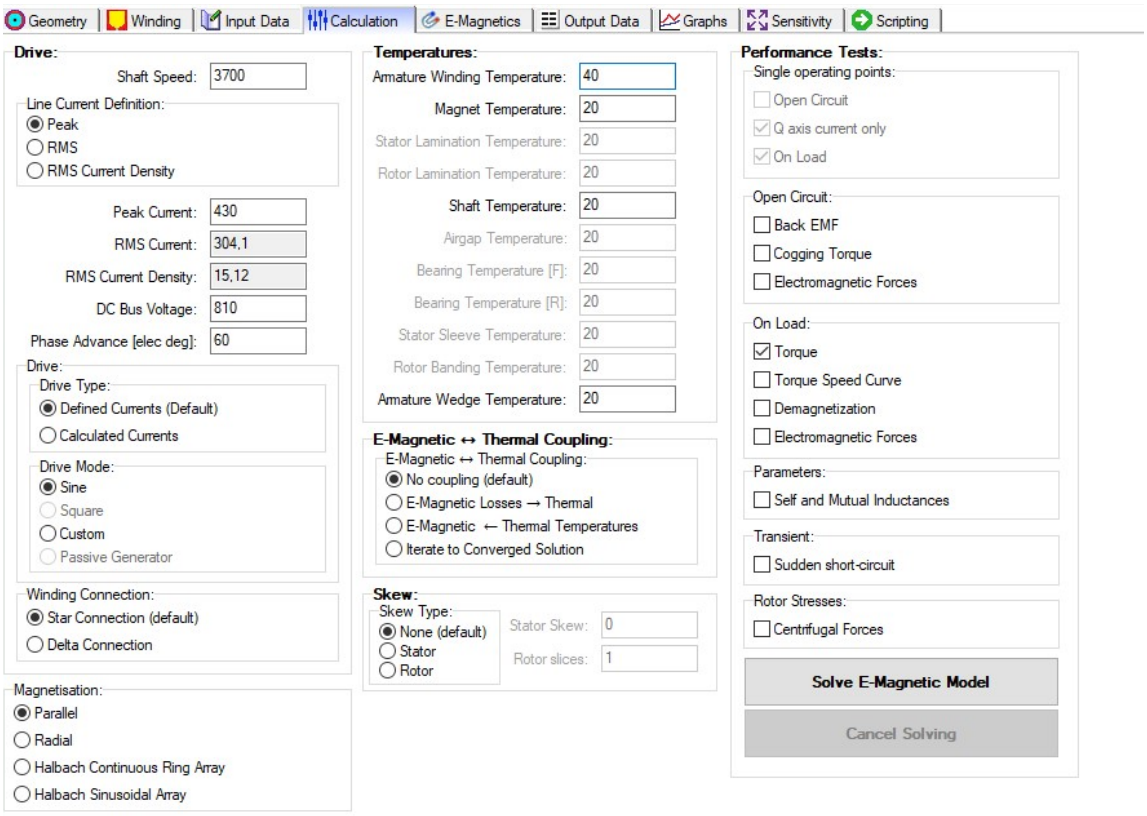

Figure 6.15: Calculation tab view with input values for Motor-CAD analysis

The following plots provide a comprehensive visualisation of various aspects of the motor's performance and characteristics through MotorCAD analysis:

Phase current:

As previously explained, it is essential to check the correctness of the input phase current (Figure 6.16):

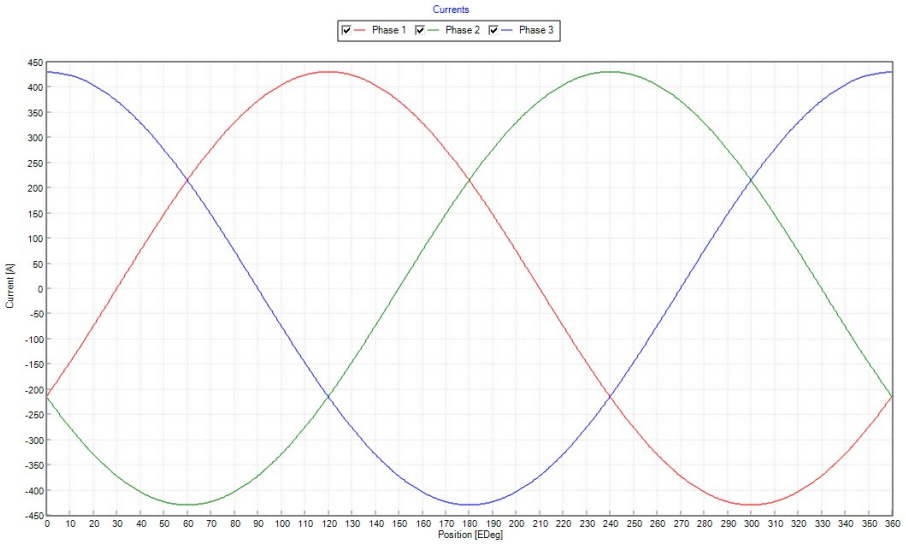

Figure 6.16: Phase currents. Peak value $\simeq$ 430A

and of the **phase voltage plot** (Figure 6.17):

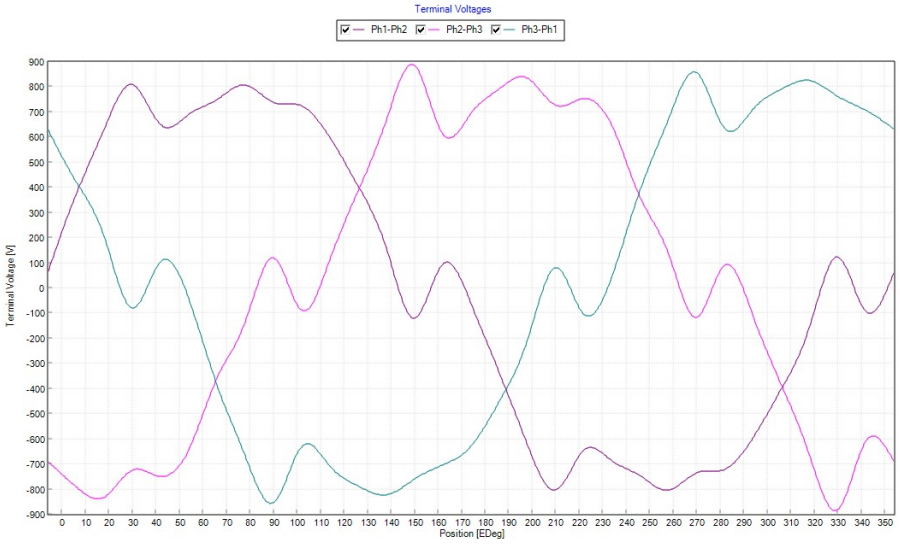

Figure 6.17: Phase voltages. Peak value $\simeq$ 810V

Torque:
The most noteworthy plot in this chapter is the torque (Figure 6.18, as it remains the focal point of this analysis throughout.

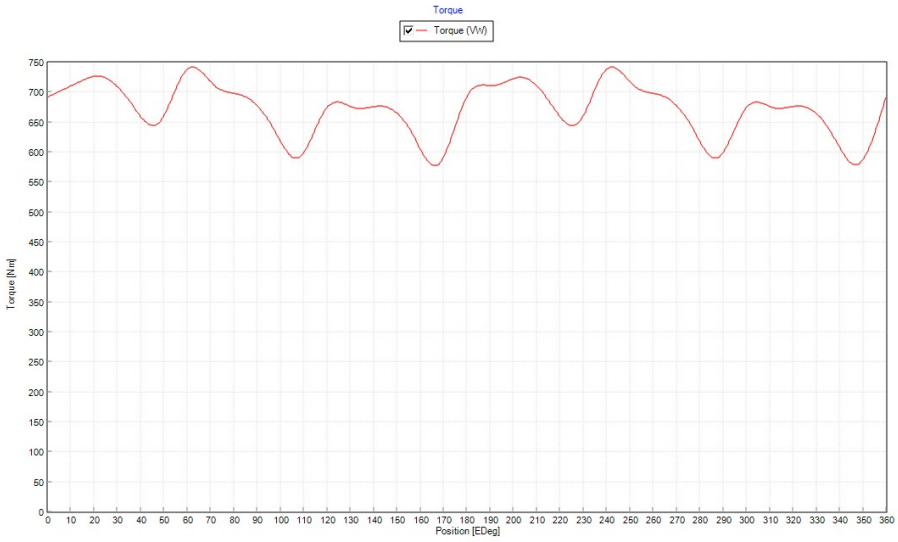

Figure 6.18: Torque. Average value $\simeq$ 700Nm

Magnetic phasor diagram:
The magnetic phasor diagram (Figure 6.19) provides insights into the magnetic field dynamics within the system, helping to understand the relationships between magnetic variables.

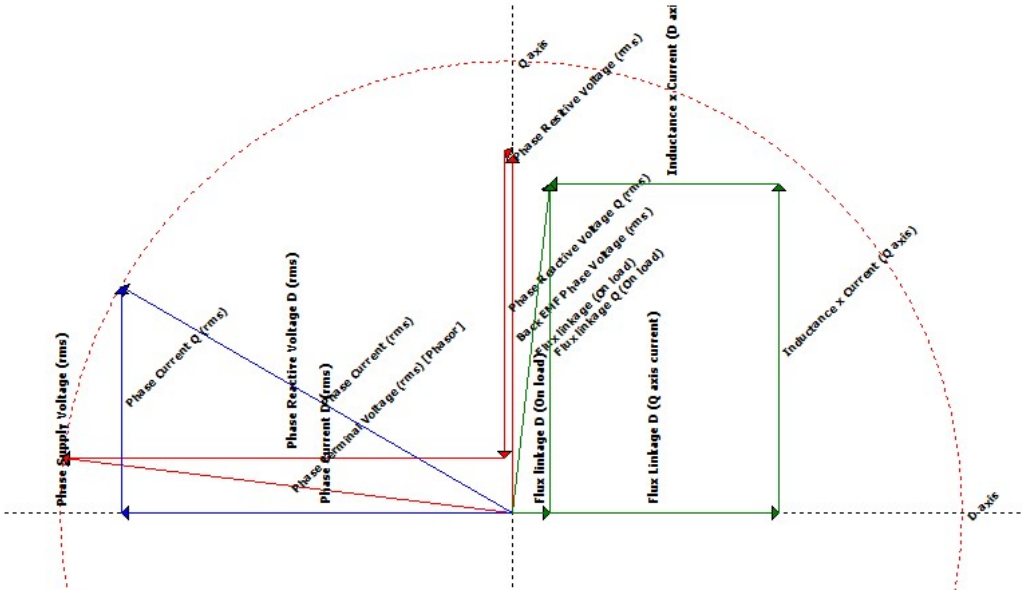

Figure 6.19: Magnetic phasor diagram

Electro-magnetic Finite Element analysis:
The plot from electromagnetic finite element analysis (Figure 6.20) offers a detailed view of the magnetic properties and behaviours within the motor, enabling in-depth analysis and optimisation.

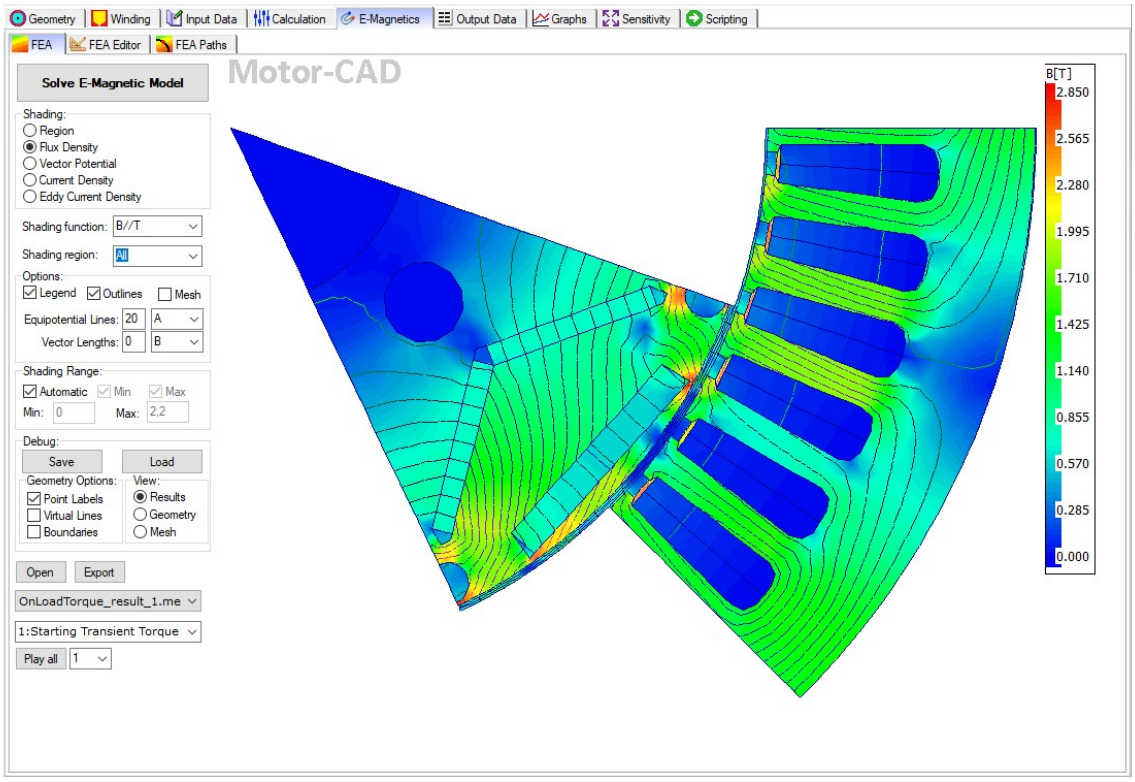

Figure 6.20: Magnetic finite element analysis plot

As explained in the previous chapters, the Nissan Leaf motor model has been adapted to satisfy the output power request of 250kW (Figure 6.21).
In conclusion, when comparing the results of axial and radial flux motor models, it is evident that the radial flux motor is bulkier and tends to deliver inferior performance for the same output power, considering input values pushed near the limit to meet the requirements. Notably, the torque produced by the radial flux motor is nearly half that of the axial flux motor. These considerations underscore the advantages of the axial flux motor design in terms of compactness and torque efficiency.

Geometry | Winding | Input Data | Calculation | E-Magnetics | Output Data | Graphs | Sensitivity | Scripting

Drive | E-Magnetics | Phasor Diagram | Equivalent Circuit | Flux Densities | Losses | Winding | Miscellaneous | Materials

Variable	Value	Units	Variable	Value	Units
Maximum torque possible (DQ) (For Phase Advance of 33,91 EDeg)	931,72	Nm	Flux Linkage D (Q axis current)	238,462	mVs
Average torque (virtual work)	671,51	Nm	Flux Linkage Q (Q axis current)	282,348	mVs
Average torque (loop torque)	696,35	Nm	Flux linkage D (On load)	33,2687	mVs
Torque Ripple (MsVw)	157,04	Nm	Flux linkage Q (On load)	294,741	mVs
Torque Ripple (MsVw) [%]	23,407	%	----		
Speed limit for constant torque (For Phase Advance of 60 EDeg)	3688	rpm	Torque Constant (Kt)	1,56025	Nm/A
No load speed	4681,8	rpm	Motor Constant (Km)	8,23749	Nm/(Watts^0.5)
Speed limit for zero q axis current	INF	rpm	Back EMF Constant (Ke) (fundamental)	1,65212	Vs/Rad
----			----		
Electromagnetic Power Operating point near voltage limit.	2,5995E005	Watts	Stall Current	16933,5	Amps
Input Power	2,8006E005	Watts	Stall Torque	26420,5	Nm
Total Losses (on load)	22656	Watts	----		
Output Power Operating point near voltage limit.	2,574E005	Watts	Cogging Period	7,5	MDeg
System Efficiency	91,91	%	Cogging Frequency	2960	Hz
----			Fundamental Frequency	246,667	Hz
Shaft Torque	664,33	Nm	Mechanical Frequency	61,6667	Hz
----			Optimum Skewing Angle	7,5	MDeg
Power Factor [Waveform] (lagging)	0,9267		----		
Power Factor Angle [Waveform]	22,074	EDeg	Magnetic Symmetry Factor (Automatic calculation)	8	
Power Factor [THD]	0,90472		Magnetic Axial Length (Slice1)	440	mm
Power Factor [Phasor] (lagging)	0,9205				
Power Factor Angle [Phasor]	23	EDeg			
Load Angle [Phasor]	83,058	EDeg			
Phase Terminal Voltage (rms) [Phasor]	331,74	Volts			

Rotor Inertia	0,083753	kg.m²			
Shaft Inertia	0,0013781	kg.m²			
Total Inertia	0,085131	kg.m²			
Torque per rotor volume	114,88	kNm/m³			

Figure 6.21: Motor-CAD analysis results

6.4 Validation of the Cooling System Design

6.4.1 Axial Flux Machine Case

ANSYS Fluent is a sophisticated Computational Fluid Dynamics (CFD) software widely employed for simulating and analysing fluid flow and heat transfer phenomena. Renowned for its versatility and robust capabilities, Fluent is extensively used in engineering applications to model and understand complex fluid dynamics scenarios. In the context of this thesis, it is employed to validate the outcomes of thermal analysis conducted on axial-flux motors with liquid cooling, as outlined in Chapter 5.4. Its sophisticated capabilities make it an invaluable tool in ensuring the accuracy and reliability of results in the thermal assessment of such systems.

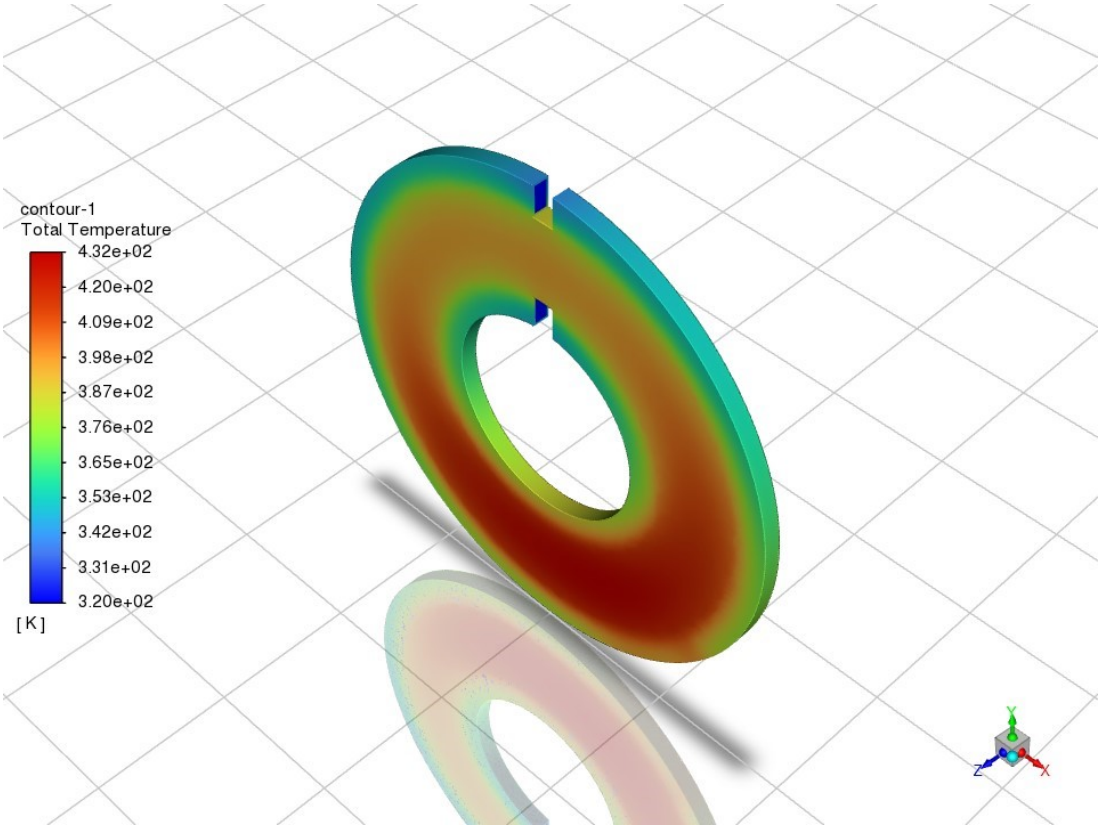

Figure 6.22: Contour figure of the thermal distribution in stator and cooling pipes

In order to gain a clearer insight into the heat distribution across the most temperature-sensitive components of the machine, the motor model underwent simplification. The focus was particularly on unravelling the intricacies of heat patterns within the winding sections, recognized as the hottest regions of the machine. The simulation accounted for heat exchange occurring between the two tubes and the stator. Notably, a deliberate cut was introduced in the tubes to simulate the fluid's entry, a necessary step in replicating the real-world fluid dynamics. The simulation was conducted under the conditions specified in Chapter 5.4.2, utilising a 40% ethylene-glycol solution at approximately 50°C (around 320K) as cooling fluid. Figure 6.22 illustrates the simulation outcome, which demonstrates convergence based on residual analysis. A peak temperature of 413K can be observed, aligning with the estimated value in Table 5.2, both corresponding to approximately 140°C. This temperature is notably below the requested 180°C specified by the PNRR project partner. Furthermore, the asymmetry in Figure 6.22 is noteworthy, indicating that the hottest point is furthest from the fluid inlet. This asymmetry is a direct consequence of the temperature increase as one moves farther away from the fluid inlet, emphasizing the dissimilar temperature distribution within the system.

6.4.2 Radial Flux Machine Case

MotorCAD simplifies thermal analysis relatively easily with the implementation of housing and fins (Figure 6.23):

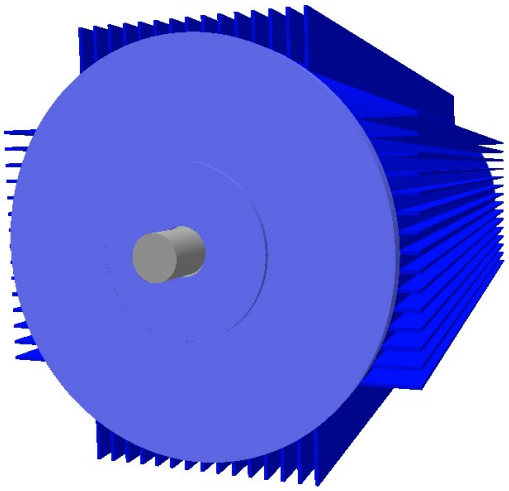

Figure 6.23: 3D motor model with finned case

By utilising finite element analysis, it extracts the temperature distribution across various areas of the motor (Figure 6.24):

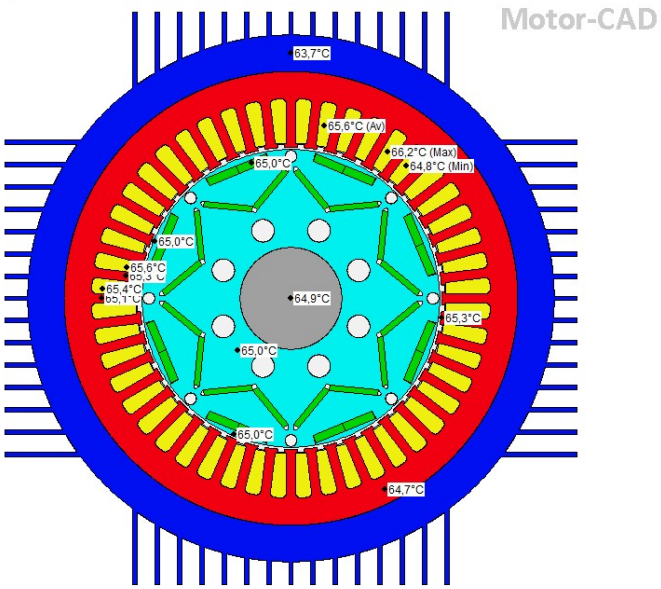

Figure 6.24: Temperature inside motor model with finned case

MotorCAD streamlines the study further by automatically generating the equivalent thermal circuit (Figure 6.25) and the corresponding schematic of temperature distribution (Figure 6.26).

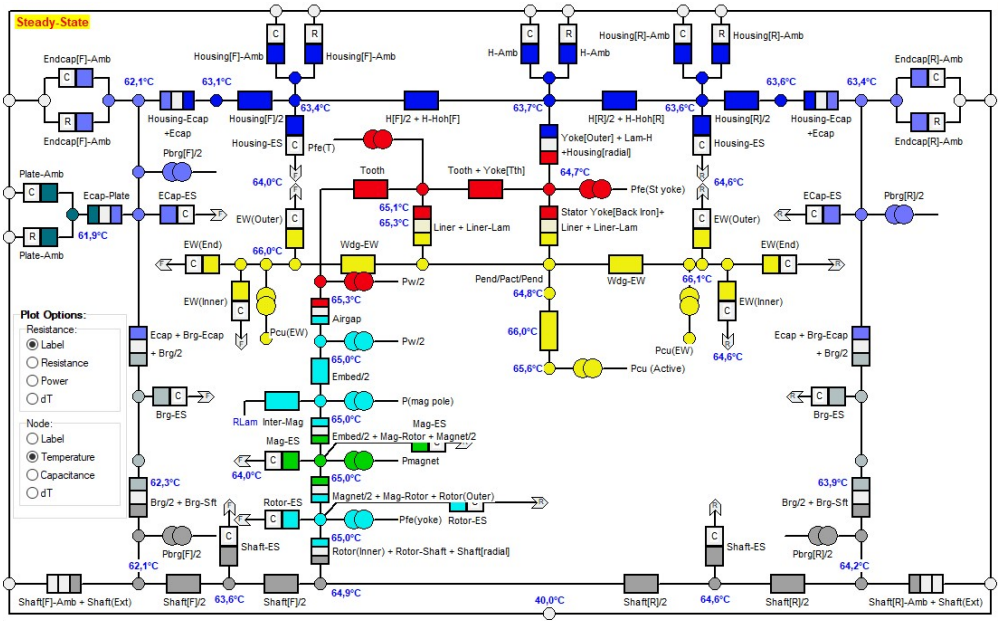

Figure 6.25: Thermal equivalent circuit of motor model with finned case

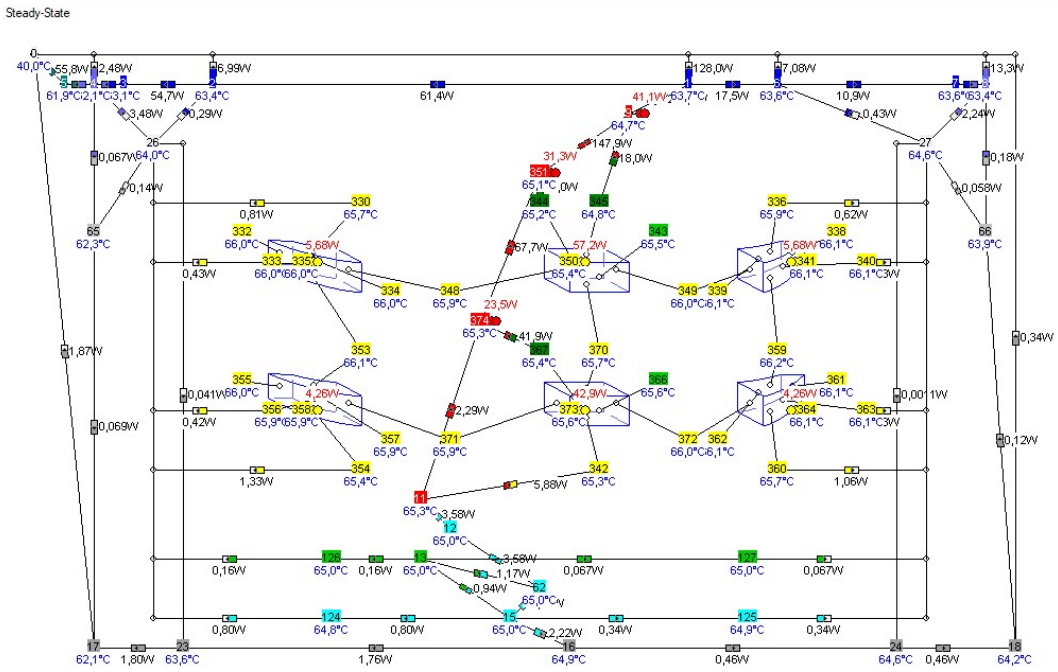

Figure 6.26: Detail schematic of temperatures inside motor model with finned case

Additionally, the finite elements analysis in MotorCAD provides a detailed view of thermal distribution within the windings (Figure 6.27):

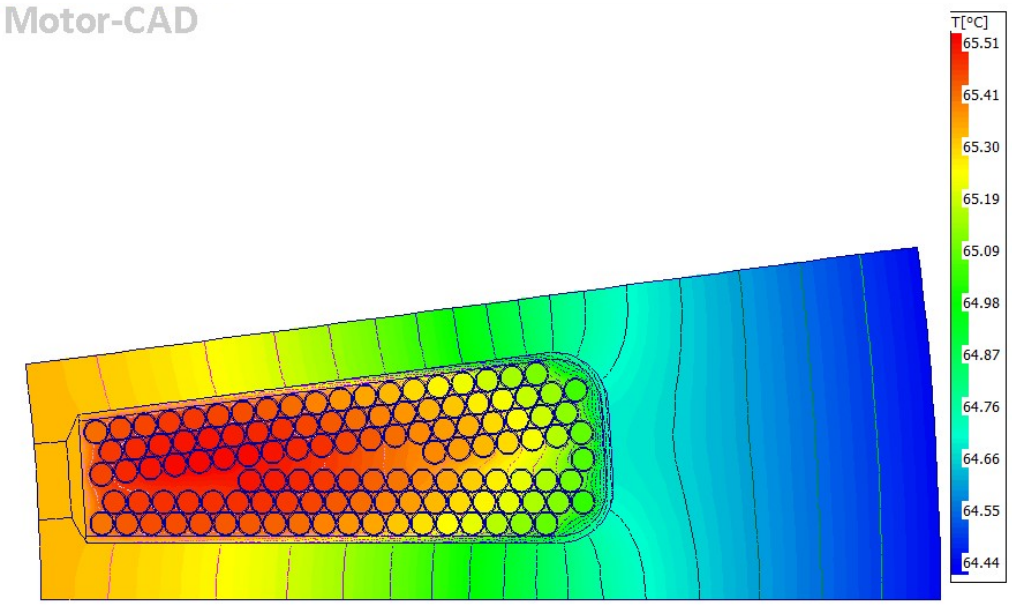

Figure 6.27: Thermal finite element analysis, windings view

These results clearly indicate that the internal motor temperatures are maintained around 65°C, even without a liquid cooling system. This stands as a significant advantage for radial flux motors, especially when compared to their axial counterparts with larger dimensions. It is worth noting that radial flux motors benefit from more extensive temperature-related research, making it easier to design an efficient cooling system to control and maintain the appropriate operating temperature. This outcome also aligns with expectations, as rotors of radial flux machines typically have a larger exchange surface and lower current to dissipate compared to axial designs.

Chapter 7

Conclusions and Future Developments

The PNRR project source of this thesis is a 3-year initiative aimed at producing various prototypes of electric motors for automotive applications. The primary objective is to facilitate the transition to electric propulsion and enhance its efficiency, especially in a context where Italy remains somewhat sceptical about electric vehicles. This scepticism is partly due to the limited infrastructure and incentives for electric vehicles compared to other European countries. Projects like this are crucial not only for technical advancement but also for raising awareness and promoting electric vehicle adoption.

In this thesis, the initial steps of designing electric motors were addressed, which are delicate and of fundamental importance in laying a solid foundation for subsequent phases. The steps involved in creating a functional electric motor prototype include determining its application purpose (in this case, the automotive sector), iteratively optimising motor design, conducting steady-state thermal analysis, and validating the axial flux motor model. The results were then compared to those obtained from the analysis of a conventional radial flux motor to better understand the potential of this new motor type.

The question of which motor type is superior, axial or radial flux, remains complex to answer definitively. The choice largely depends on the specific application. In the automotive context, the axial flux motor exhibits significant potential for success, as evidenced by investments from companies like Koenigsegg and Mercedes-Benz, as mentioned in Chapter 2.3. When a compact, high-performance motor is needed, the axial flux design is a suitable option. However, it's essential to note that there is still limited research in this field, making venturing into this area both innovative and challenging. One critical consideration is the limited research on adaptive cooling for these motors, as their compact nature can lead to significant heating issues, particularly in the winding area.

The steps to be followed to complete this project include a more comprehensive transient temperature analysis, considering the potential use of robust predictive control, taking into account the motor's operating environment.

Possible control methods to consider are Model Predictive Control (MPC) or Linear-Quadratic Model Predictive Control (LQ-MPC). MPC is commonly used for managing complex dynamic systems like motors, relying on a mathematical model of the system to predict its future behaviour and adjusting control to minimise an objective function, such as maintaining the motor's temperature within desired limits.

Subsequent steps will involve integrating the onboard vehicle drive system and the battery management and power supply system. This will culminate in the production of a physical prototype, which will undergo laboratory testing and validation. During this process, discrepancies may arise, necessitating parameter adjustments and revisiting certain previous steps to ensure the development of an efficient and, most importantly, safe product.

It is also imperative to ensure that the electric machine complies with relevant industry standards, safety regulations, and certification requirements. Lastly, the electric machine should be installed in its intended application, and a maintenance plan should be established to ensure long-term reliability and performance.

Bibliography

[1] R. Aydoun, G. Parent, A. Tounzi, and J.-P. Lecointe, "Performance comparison of axial-flux switched reluctance machines with non-oriented and grain-oriented electrical steel rotors," *Open Physics*, vol. 18, no. 1, pp. 981–988, 2020.

[2] J. Ma, J. Li, H. Fang, Z. Li, Z. Liang, Z. Fu, L. Xiao, and R. Qu, "Optimal design of an axial-flux switched reluctance motor with grain-oriented electrical steel," *IEEE Transactions on Industry Applications*, vol. 53, no. 6, pp. 5327–5337, 2017.

[3] J.-F. TSAI and Y.-P. CHEN, "Design and performance analysis of an axial-flux disk-type switched reluctance motor for hybrid scooters," *JSME International Journal Series C Mechanical Systems, Machine Elements and Manufacturing*, vol. 49, no. 3, pp. 882–889, 2006.

[4] R. Madhavan and B. G. Fernandes, "Comparative analysis of axial flux srm topologies for electric vehicle application," in *2012 IEEE International Conference on Power Electronics, Drives and Energy Systems (PEDES)*, pp. 1–6, 2012.

[5] C. H. T. Lee, C. Liu, and K. T. Chau, "A magnetless axial-flux machine for range-extended electric vehicles," *Energies*, vol. 7, no. 3, pp. 1483–1499, 2014.

[6] W. Sun, Q. Li, K. Liu, and L. Li, "Design and analysis of a novel rotor-segmented axial-field switched reluctance machine," *CES Transactions on Electrical Machines and Systems*, vol. 1, no. 3, pp. 238–245, 2017.

[7] M. J. Kermanipour and B. Ganji, "Modification in geometric structure of double-sided axial flux switched reluctance motor for mitigating torque ripple," *Canadian Journal of Electrical and Computer Engineering*, vol. 38, no. 4, pp. 318–322, 2015.

[8] M. Belhadi, G. Krebs, C. Marchand, H. Hannoun, and X. Mininger, "Evaluation of axial srm for electric vehicle application," *Electric Power Systems Research*, vol. 148, pp. 155–161, 2017.

[9] H. Arihara and K. Akatsu, "A basic property of axial type switched reluctance motor," 01 2010.

[10] Y. Li and J. D. Lloyd, "Axial flux reluctance machine with two stators driving a rotor," July 1999.

[11] F. Daldaban and N. Ustkoyuncu, "New disc type switched reluctance motor for high torque density," *Energy Conversion and Management*, vol. 48, no. 8, pp. 2424–2431, 2007.

[12] P. Desai and A. Emadi, "Switched reluctance machine," May 2006.

[13] H. Goto, T. Shibamoto, K. Nakamura, and O. Ichinokura, "Development of high torque density axial-gap switched reluctance motor for in-wheel direct-drive ev," pp. 1–7, 09 2013.

[14] R. Madhavan and B. G. Fernandes, "A novel axial flux segmented srm for electric vehicle application," in *The XIX International Conference on Electrical Machines - ICEM 2010*, pp. 1–6, 2010.

[15] R. Madhavan and B. G. Fernandes, "Axial flux segmented srm with a higher number of rotor segments for electric vehicles," *IEEE Transactions on Energy Conversion*, vol. 28, no. 1, pp. 203–213, 2013.

[16] L. Jia, K. Lin, M. Lin, W. Le, and S. Wang, "Comparative analysis of dual-rotor modular stator axial-flux permanent magnet machines with different rotor topologies," *IEEE Transactions on Applied Superconductivity*, vol. 31, no. 8, pp. 1–5, 2021.

[17] W. Geng, J. Hou, and Q. Li, "Electromagnetic analysis and efficiency improvement of axial-flux permanent magnet motor with yokeless stator by using grain-oriented silicon steel," *IEEE Transactions on Magnetics*, vol. 58, no. 2, pp. 1–5, 2022.

[18] M. T. Bin Tarek and Y. Sozer, "Design of a novel axial flux permanent magnet assisted synchronous reluctance motor," in *2019 IEEE Energy Conversion Congress and Exposition (ECCE)*, pp. 3004–3009, 2019.

[19] J. Wang, W. Geng, Q. Li, L. Li, and J. Guo, "A novel spoke-type ipm rotor with hybrid radial and axial flux concentration for reduction of interpolar leakage flux," *IEEE Transactions on Magnetics*, vol. 58, no. 8, pp. 1–6, 2022.

[20] J. M. Seo, J.-S. Ro, S.-H. Rhyu, I.-S. Jung, and H.-K. Jung, "Novel hybrid radial and axial flux permanent-magnet machine using integrated windings for high-power density," *IEEE Transactions on Magnetics*, vol. 51, no. 3, pp. 1–4, 2015.

[21] R. Lehmann, M. Künzler, M. Moullion, and F. Gauterin, "Comparison of commonly used cooling concepts for electrical machines in automotive applications," *Machines*, vol. 10, no. 6, 2022.

[22] C. Dong, Y. Qian, Y. Zhang, and W. Zhuge, "A review of thermal designs for improving power density in electrical machines," *IEEE Transactions on Transportation Electrification*, vol. 6, no. 4, pp. 1386–1400, 2020.

[23] F. P. McCluskey, Y. Saadon, Z. Yao, and A. Camacho, "Cooling for electric aircraft motors," in *Proc. 18th IEEE Intersociety Conf. Thermal Thermomechanical Phenomena Electron. Syst. (ITherm)*, pp. 1–5, 2019.

[24] H. Lin, H. Guo, and H. Qian, "Design of high-performance permanent magnet synchronous motor for electric aircraft propulsion," in *Proc. 21st Int. Conf. Electr. Mach. Syst. (ICEMS)*, pp. 174–179, 2018.

[25] P. H. Mellor, J. Yon, J. L. Baker, D. North, and J. D. Booker, "Electromagnetic and thermal coupling within a fault-tolerant aircraft propulsion motor," in *Proc. IEEE Int. Electr. Mach. Drives Conf. (IEMDC)*, pp. 1–7, 2017.

[26] S. Mizuno, S. Noda, M. Matsushita, T. Koyama, and S. Shiraishi, "Development of a totally enclosed fan-cooled traction motor," *IEEE Trans. Ind. Appl.*, vol. 49, no. 4, pp. 1508–1514, 2013.

[27] N. Putra and B. Ariantara, "Electric motor thermal management system using l-shaped flat heat pipes," *Appl. Thermal Eng.*, vol. 126, pp. 1156–1163, 2017.

[28] S. Wang, Y. Li, Y.-Z. Li, J. Wang, X. Xiao, and W. Guo, "Transient cooling effect analyses for a permanent-magnet synchronous motor with phase-change-material packaging," *Appl. Thermal Eng.*, vol. 109, pp. 251–260, 2016.

[29] Z. Huang, S. Nategh, V. Lassila, M. Alakula, and J. Yuan, "Direct oil cooling of traction motors in hybrid drives," in *Proc. IEEE Int. Electr. Vehicle Conf.*, pp. 1–8, 2012.

[30] P. A. et al., "Comparative design analysis of permanent magnet rotor topologies for an aircraft starter-generator," in *Proc. IEEE Int. Conf. Intell. Energy Power Syst. (IEPS)*, pp. 273–278, 2014.

[31] Z. X. et al., "A semi-flooded cooling for a high-speed machine: Concept, design and practice of an oil sleeve," in *Proc. 43rd Annu. Conf. IEEE Ind. Electron. Soc. (IECON)*, pp. 8557–8562, 2017.

[32] R. Camilleri, D. A. Howey, and M. D. McCulloch, "Predicting the temperature and flow distribution in a direct oil-cooled electrical machine with segmented stator," *IEEE Trans. Ind. Electron.*, vol. 63, no. 1, pp. 82–91, 2016.

[33] X. Fan, D. Li, R. Qu, C. Wang, and H. Fang, "Water cold plates for efficient cooling: Verified on a permanent-magnet machine with concentrated winding," *IEEE Transactions on Industrial Electronics*, vol. 67, no. 7, pp. 5325–5336, 2020.

[34] M. Polikarpova, P. M. Lindh, J. A. Tapia, and J. J. Pyrhonen, "Application of potting material for a 100 kw radial flux pmsm," in *Proc. Int. Conf. Electr. Mach. (ICEM)*, pp. 2146–2151, 2014.

[35] M. Polikarpova, P. Lindh, C. Gerada, M. Rilla, V. Naumanen, and J. Pyrhönen, "Thermal effects of stator potting in an axial-flux permanent magnet synchronous generator," *Appl. Thermal Eng.*, vol. 75, pp. 421–429, 2015.

[36] P. Ponomarev, M. Polikarpova, and J. Pyrhonen, "Thermal modeling of directly-oil-cooled permanent magnet synchronous machine," in *Proc. 20th Int. Conf. Electr. Mach.*, pp. 1882–1887, 2012.

[37] L. Ye, F. Tao, L. Qi, and W. Xuhui, "Experimental investigation on heat transfer of directly-oil-cooled permanent magnet motor," in *Proc. 19th Int. Conf. Elect. Mach. Syst. (ICEMS)*, pp. 1–4, 2016.

[38] T. Davin, J. Pellé, S. Harmand, and R. Yu, "Experimental study of oil cooling systems for electric motors," *Applied Thermal Engineering*, vol. 75, p. 1–13, 2015.

[39] V. Madonna, A. Walker, P. Giangrande, G. Serra, C. Gerada, and M. Galea, "Improved thermal management and analysis for stator end windings of electrical machines," *IEEE Trans. Ind. Electron.*, vol. 66, no. 7, p. 5057–5069, 2019.

[40] R. Ponnappan and J. E. Leland, "Rotating heat pipe for high-speed motor/generator cooling," in *SAE Trans.*, vol. 107, p. 167–172, 1998.

[41] L. Li, J. Zhang, C. Zhang, and J. Yu, "Research on electromagnetic and thermal issue of high-efficiency and high-power-density outer-rotor motor," *IEEE Trans. Appl. Supercond.*, vol. 26, no. 4, p. 1–5, 2016.

[42] X. Zhang, C. Zhang, P. Fu, C. Zhang, and L. Li, "A novel cooling technique for the windings of high-torque-density permanent magnet machines," in *Proc. 21st Int. Conf. Electr. Mach. Syst. (ICEMS)*, p. 332–337, 2018.

[43] G. Fang, W. Yuan, Z. Yan, Y. Sun, and Y. Tang, "Thermal management integrated with three-dimensional heat pipes for air-cooled permanent magnet synchronous motor," *Appl. Thermal Eng.*, vol. 152, p. 594–604, 2019.

[44] S. A. Semidey and J. R. Mayor, "Experimentation of an electric machine technology demonstrator incorporating direct winding heat exchangers," *IEEE Trans. Ind. Electron.*, vol. 61, no. 10, p. 5771–5778, 2014.

[45] M. Schiefer and M. Doppelbauer, "Indirect slot cooling for high-power density machines with concentrated winding," in *Proc. IEEE Int. Electr. Mach. Drives Conf. (IEMDC)*, p. 1820–1825, 2015.

[46] C. Rhebergen, B. Bilgin, A. Emadi, E. Rowan, and J. Lo, "Enhancement of electric motor thermal management through axial cooling methods: A materials approach," in *Proc. IEEE Energy Convers. Congr. Expo. (ECCE)*, p. 5682–5688, 2015.

[47] H.-C. Lahne, D. Gerling, D. Staton, and Y. C. Chong, "Design of a 50000 rpm high-speed high-power six-phase pmsm for use in aircraft applications," in *Proc. 11th Int. Conf. Ecol. Vehicles Renew. Energies (EVER)*, p. 1–11, 2016.

[48] S. Ayat, C. Serghine, T. Klonowski, S. Yon, A. Mutabazi, and S. McDaniel, "The use of phase change material for the cooling of electric machine windings formed with hollow conductors," in *Proc. IEEE Int. Electr. Mach. Drives Conf. (IEMDC)*, p. 1195–1201, 2019.

[49] W. R. Canders, J. Ho, and M. Henke, "Cooling technologies for high power density electrical machines for aviation applications," *Energies*, vol. 12, no. 23, 2019.

[50] W. Sixel, M. Liu, G. Nellis, and B. Sarlioglu, "Cooling of windings in electric machines via 3-d printed heat exchanger," *IEEE Transactions on Industry Applications*, vol. 56, no. 5, p. 4718–4726, 2020.

[51] A. S. Fawzal, R. M. Cirstea, K. N. Gyftakis, T. J. Woolmer, M. Dickison, and M. Blundell, "Fan performance analysis for rotor cooling of axial flux permanent magnet machines," *IEEE Trans. Ind. Appl.*, vol. 53, no. 4, p. 3295–3304, 2017.

[52] M. Tosetti, P. Maggiore, A. Cavagnino, and S. Vaschetto, "Conjugate heat transfer analysis of integrated brushless generators for more electric engines," *IEEE Trans. Ind. Appl.*, vol. 50, no. 4, p. 2467–2475, 2014.

[53] X. Yi, R. Sanchez, K. Haran, J. Veres, A. T. Perry, and P. J. Ansell, "Self-pumped air-cooling design for a high-speed high-specific-power motor," in *Proc. IEEE Transp. Electrific. Conf. Expo (ITEC)*, p. 274–279, 2018.

[54] H. Li, "Cooling of a permanent magnet electric motor with a centrifugal impeller," *Int. J. Heat Mass Transf.*, vol. 53, no. 4, p. 797–810, 2010.

[55] W. G. et al., "A liquid-cooled rotor for high density electric machines," in *Proc. 47th AIAA/ASME/SAE/ASEE Joint Propuls. Conf. Exhib.*, p. 5560, 2011.

[56] K.-H. Lee, H.-R. Cha, and Y.-B. Kim, "Development of an interior permanent magnet motor through rotor cooling for electric vehicles," *Appl. Thermal Eng.*, vol. 95, p. 348–356, 2016.

[57] Y. Gai, M. Kimiabeigi, Y. C. Chong, J. D. Widmer, X. Deng, M. Popescu, J. Goss, D. A. Staton, and A. Steven, "Cooling of automotive traction motors: Schemes, examples, and computation methods," *IEEE Transactions on Industrial Electronics*, vol. 66, no. 3, p. 1681–1692, 2019.

[58] G. Previati, G. Mastinu, and M. Gobbi, "Thermal management of electrified vehicles—a review," *Energies*, vol. 15, no. 4, 2022.

[59] D. C. Deisenroth and M. Ohadi, "Thermal management of high-power density electric motors for electrification of aviation and beyond," *Energies*, vol. 12, no. 3594, 2019.

[60] D. Staton, E. Chong, S. Pickering, and A. Boglietti, *Cooling of Rotating Electrical Machines: Fundamentals, modelling, testing and design.* 2022.

[61] J. F. Gieras, R.-J. Wang, and M. J. Kamper, *Axial Flux Permanent Magnet Brushless Machines.* Springer Dordrecht, 2nd ed., 2008.

[62] YASA, *YASA 750R E-Motor.*

[63] Koenigsegg, *The Quark e-Motor.*

[64] *Dynamics of Electrical Machines and Drives, Course Lecture Notes.*

[65] F. P. Incropera, D. P. DeWitt, T. L. Bergman, and A. S. Lavine, *Fundamentals of Heat and Mass Transfer.* John Wiley & Sons, 6th ed., 2006.

[66] J. Pyrhönen, T. Jokinen, and V. Hrabovcová, *Design of Rotating Electrical Machines.* John Wiley & Sons, 2nd ed., 2014.

[67] *Matlab online documentation.*

[68] *DOWTHERM™ SR-1 Fluid Technical Data Sheet.*